7-10-2017

Polymer Nanocomposites and Biomaterials: From Chemical Cross-linking to 3D Printing

Huseini Patanwala
University of Connecticut - Storrs, huseini.patanwala@gmail.com

Polymer Nanocomposites and Biomaterials:

From Chemical Cross-linking to 3D Printing

Huseini Shabbir Patanwala, PhD

University of Connecticut, [2017]

Abstract:

Part 1:

Aerogel is an open-celled, microporous, solid foam composed of a network of interconnected structures formed by replacing the solvent in wet gel with air. Integrating the intrinsic mechanical and electrical properties of carbon nanotubes (CNTs) with those of an aerogel provides a new class of material with unique multifunctional properties which may find applications not limited to fuel cells, super capacitors and batteries. I attempt at improving the mechanical integrity by first functionalizing the CNTs with carboxylic (-COOH) groups and subsequently cross-linking the CNTs using diisocyanate to form polyurea-CNT (PUA-CNT) composite aerogels. Mechanical properties of the final PUA-CNT aerogels are presented.

Part 2:

3D printing is an additive manufacturing technique capable of creating highly complex and customized structures that are otherwise difficult or impossible to produce using conventional methods such as injection molding. Fused Deposition Modeling (FDM) based on micro-extrusion

of thermoplastics is one of the most commonly used methods for 3D printing. The second part of this thesis reports incorporation of carbon nanotubes (CNTs) into PLA with a goal to improve the mechanical properties of the 3D-printed composites. The orientation distribution of CNTs within the printed extrudates has been characterized using X-ray Diffraction (XRD) and scanning electron microscopy (SEM). The effects of process conditions on CNT orientation and the subsequent mechanical properties of fabricated test coupons have been explored.

Part 3:

Breast cancer is caused by the development of malignant cells in the breast forming a lump or mass called tumor. The malignant cells originate in the lining of the milk glands or ducts of the breast (ductal epithelium) and grow into the surrounding breast tissue. As per the American Cancer Society, in 2015, 1 out of 7 women diagnosed with breast cancer died due to complications arising from the disease. I lay down the foundations for precise and reproducible FDM based 3D bioprinting to help understand the interactions of breast cancer cells with its microenvironment which upon further mathematical modeling may lead to better strategies to treat the disease. Rheology is used as a tool to identify printing parameters of Matrigel®; an extracellular matrix.

Polymer Nanocomposites and Biomaterials:

From Chemical Cross-linking to 3D Printing

Huseini Shabbir Patanwala

B. Tech., Institute of Chemical Technology, Mumbai, India [2008]

A Dissertation

Submitted in Partial Fulfillment of the

Requirements for the Degree of

Doctor of Philosophy

at the

University of Connecticut

[2017]

APPROVAL PAGE

Doctor of Philosophy Dissertation

Polymer Nanocomposites and Biomaterials: From Chemical Cross-linking to 3D Printing

Presented by

Huseini Shabbir Patanwala, B. Tech.

Major Advisor

_____

Anson W. K. Ma

Associate Advisor

_____

Suzy V. Torti

Associate Advisor

_____

Mu-Ping Nieh

Associate Advisor

_____

Montgomery Shaw

Associate Advisor

_____

Richard Parnas

University of Connecticut
[2017]

Acknowledgments

I express my deepest gratitude towards my major advisor, Dr. Anson Ma for his guidance and unwavering support throughout these years. His passion for science and research has been inspiring. I thank Dr. Montgomery Shaw, Dr. Mu-Ping Nieh, and Dr. Richard Parnas for their valuable advice on research and the efforts they put in for teaching various courses. I have learned a lot and gained an enormous value and understanding about rheology, nanostructural characterization and polymer composites by virtue of discussions with these stalwarts. A special thanks to Dr. Suzy Torti for introducing me to the realm of biology and helping me realize the need and importance of working at the intersection of two multidisciplinary fields of materials science and biology.

I acknowledge and appreciate the amazing camaraderie I developed with my colleagues Dr. Brice Bognet, Dr. Yang Guo, Dr. Sahil Vora, Erik Carboni and Nicole Farra. I also acknowledge Dr. Laura Pinatti for training and advising me on thermal characterizations, Dr. Mark Dudley for his assistance with chromatography and mechanical testing, Dr. Lichun Zhang for familiarizing me with electron microscopy techniques, Dr. Gary Lavigne for his advice on spectroscopy techniques and finally Dr. Jack Gromek and Dr. Daniela Morales for their help and guidance with X-ray diffraction.

I thank the Polymer Program, the Graduate School and the International Student & Scholar Services at UConn for providing me with the intellectual foresight of advisors, scholars and fellows from around the world. I thank Mrs. YoungHee Chudy, Mrs. Nancy Kellerann, Mrs. Shari Masinda, Mrs. Maria Mejias, Mrs. Rhonda Ward, Mrs. Kimberly Post and Mrs. Deb Perko for being a support system and guiding and helping me with all the administrative requirements. I also thank General Electric for acknowledging the novelty and significance of my work through GE Graduate Fellowship for Innovation.

A very special thanks to my wife, Dr. Inseyah Bagasrawala, for being a pillar of moral support and motivation in my life. I am also grateful to my parents & my sister and their enormous respect for the quest of knowledge that has made me achieve what I have so far. A special mention of my in-laws for their well wishes. I cannot end without thanking my friends Dr. Dhaval Kulkarni, Vivek Iyer, Joseline Raja, Rishabh Kejriwal, Avnish Kumar, Gabrielle Mutel, Dr. Jennifer Bento, Dr. YNhi Doan, Rui Ma and Joon-Sung Kim for being there and supporting my endeavors and of course for having fun.

I dedicate my thesis to science.

TABLE OF CONTENTS

LIST OF FIGURES

LIST OF TABLES

ABBREVIATIONS

CNT	Carbon Nanotubes
o-CNT	Oxidized carbon nanotubes
PUA	Polyurea
PLA	Polylactic acid
FDM	Fused Deposition Modeling
SLS	Selective Laser Sintering
SLA	Stereolithography
CAD	Computer-aided design
RF	Resorcinol formaldehyde
MF	Melamine formaldehyde
SDBS	Dodecylbenzene sulfonate
PVA	Polyvinyl alcohol
CA	Carbon aerogel
XRD	X-ray diffraction
SEM	Scanning electron microscopy
FTIR	Fourier Transform Infrared Spectroscopy
HDI	Hexamethylene diisocyanate
TGA	Thermogravimetric analysis
DSC	Differential scanning calorimetry
ABS	Acrylonitrile butadiene styrene copolymer
CVD	Chemical vapor deposition

GPC	Gel Permeation Chromatography
FWHM	Full width at half maximum
RoM	Rules of mixture
HDP	Hanging drop microplate
DOD	Drop on demand
CIJ	Continuous inkjet
ECM	Extracellular matrix
DMEM	Dulbeccos minimal essential media
FBS	Fetal bovine serum
GFP	Green fluorescent protein
RFP	Red fluorescent protein
NEAA	Non-essential amino acid
LVE	Linear viscoelastic region

NOMENCLATURE

L_p	Persistence length
T_g	Glass transition temperature
T_m	Melting temperature
T_d	Degradation temperature
ΔH_m	Enthalpy of melting
ΔH_c	Enthalpy of crystallization
ΔH_f°	Enthalpy of fusion
ρ_{CNT}	Density of CNT
ρ_{PLA}	Density of PLA
λ	Aspect ratio (length to diameter ratio)
η_s	Viscosity of the suspending medium
n	Power law coefficient
$\dot{\gamma}_w$	Wall shear rate
$\dot{\gamma}$	Shear rate
D_r	Rotary diffusivity
Pe	Peclet number
k_b	Boltzman constant
T	Temperature
r	radius
l	Length
d	Diameter
d_{nozzle}	Print nozzle diameter

Hz	Hertz
G’	Elastic moduli
G’’	Viscous moduli
η^*	Complex viscosity
η	Apparent viscosity
η_s	Suspending medium viscosity
Q	Volumetric flow rate
Q_r	Reduced volumetric flow rate
Q_{actual}	Actual volumetric flow rate
Q_{ideal}	Ideal volumetric flow rate
h	Gap
v	Linear translation speed of the printhead
E_c	Composite modulus
E_m	Matrix modulus
E_f	Fiber modulus
V_f	Filler/Fiber volume fraction
$E_{//}$	Longitudinal modulus of the composite
$\eta_{//}$	Longitudinal efficiency factor
η_L	Length correction factor
η_o	Krenchel orientation correction factor
α_n	Angle which a group of fibers make with the loading direction
a_{fn}	Proportion of a particular group of fibers lying in a given place

Chapter 1 - Introduction

1.1 Thesis Structure:

This dissertation is divided into three major chapters, each chapter dedicated to a different research project. Research in chapter 2 investigates a facile method of synthesizing polyurea – carbon nanotube (PUA-CNT) aerogels. This involved oxidizing pristine CNTs using a highly concentrated acid mixture under sonication and mild temperature conditions. Unlike, many other reports where oxidized CNTs are cross-linked using multi-step functionalization, we employed a one-pot synthesis of polyurea using moisture in the air to form PUA-CNT aerogels.

Chapter 3 focuses on studying and understanding the structure and properties of 3D printed carbon nanotube – polylactic acid (CNT-PLA) composites. The purpose of this research was to understand the challenges and opportunities of short fiber-reinforced composites fabricated using 3D printing and to specifically evaluate the potential for load-bearing components. Our results show that composites with oriented carbon nanotubes can be 3D printed.

Chapter 4 is a proof-of-concept study on 3D printing viable cells with a very common extracellular matrix called Matrigel®. Primary aim of this research is to lay the foundation in order to combine precise and reproducible 3D bioprinting with predictive mathematical modeling to understand the role of the local environment in the growth of breast tumors.

1.2 Carbon Nanotubes (CNTs)

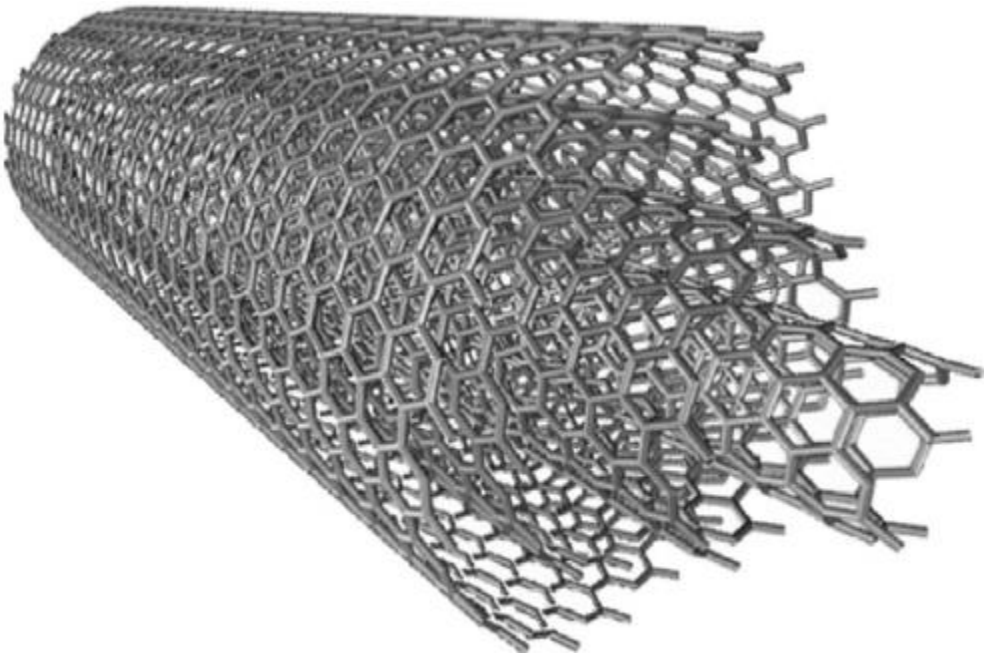

Figure 1.1: Schematic representation of a multi-walled CNT. Reproduced with permission from [1].

Carbon nanotubes (CNTs) are hollow cylindrical macromolecules composed of sp^2 hybridized carbon atoms and are equivalent to a graphitic (graphene) sheet rolled into a seamless tube, capped or uncapped at the ends (**Figure 1.1**) [2]. Iijima *et al*. synthesized needle-like tubes of carbon[1] by the electric-arc technique in 1991 [3]. Since then, CNTs have become the focus of nanoscience and nanotechnology owing to their structures and their wide range of potential applications [2].

The exact diameter and length (distribution) of CNTs vary depending on the synthesis method, but the aspect ratio[2] is always greater than 1 given their shape. This gives them characteristics similar to single molecules or quasi-one dimensional crystals with translational periodicity along the tube

[1] Later termed as carbon nanotubes
[2] Aspect ratio is defined as the ratio of the length-to-diameter of the CNT

axis [4]. CNTs offer fascinating properties like low density (1.8 g/cm^3), high elastic moduli (about 1 TPa), and high thermal (3000W/mK) and electrical conductivities (10^6 S/m) [5]–[8]. These superior properties make CNTs attractive for lightweight and multifunctional applications and technologies.

Despite their great potential, pristine CNTs tend to aggregate as they are processed or incorporated into macroscopic articles such as fibers, films, and composites. The lack of precise control on CNT nano/microstructure has, in many cases, led to only moderate improvements in material properties.

1.3 3D Printing

3D printing has been around since 1980's. In 1986, Charles Hull, in his method named "stereolithography" described a 3D printing technique based on curing thin layers of a cross-linkable material using ultraviolet light. He later went on to co-found 3D Systems Corporation – one of the largest and most prolific 3D printing organizations operating today. Later Carl Deckard, was issued a patent in 1989 for Selective Laser Sintering (SLS) process where a powdered material is fused or sintered using a laser. This technology was then licensed to DTM Inc, which was later acquired by 3D Systems. Also, in 1989 Scott Crump, a co-founder of Stratasys Inc. filed a patent for Fused Deposition Modeling (FDM) where a filament is extruded through a hot end and laid on the build plate layer-by-layer to form the object.

3D printing is a layered manufacturing technique that prints a three dimensional object created from a virtual model in any computer-aided design modeling software. A 3D printer can manufacture net-shaped components without the need to produce molds or dies and therefore can

help reduce overall product development time and increase manufacturing flexibility. This is one of the major reasons for the widespread acceptability of 3D printing technologies in various industries.

There are a number of steps involved in order to print a part. First, a part is modeled using three-dimensional computer-aided design (CAD) software such as AutoCAD®. Three-dimensional models are saved in the STL file format which is commonly used by majority of the 3D printers. Each printer comes with a model slicing software which determines a variety of process parameters like material in-fill density, in-fill pattern, nozzle temperature, linear translation speed of the printhead, etc. The STL file is first imported into the slicing software, then positioned and oriented, and the part size is adjusted if needed. The STL file is then sliced into a number of layers. Each sliced layer has a cross sectional area of finite thickness. Finally the build file is generated and transferred to the 3D printer as a g-code. The printer reads this g-code and automatically builds the part under minimal supervision. The part is built layer by layer, where each layer is a cross sectional slice of desired thickness as fixed while slicing the part. Once a given layer is printed, the build platform lowers by the distance equal to the slice layer thickness. With the lowered build platform, the next layer is built on top of the previous layer. This process continues until the build is complete.

There are various types of 3D printing technologies and they may be classified by the methods used in their solid freeform fabrication technique [9]. Some common technologies are Stereolithography (SLA), Fused-Deposition Modelling (FDM), and Selective Laser Sintering (SLS) [10]. Each of these technologies use different tool heads, operate at different temperatures, and use different deposition techniques and materials.

Fused Deposition Modeling

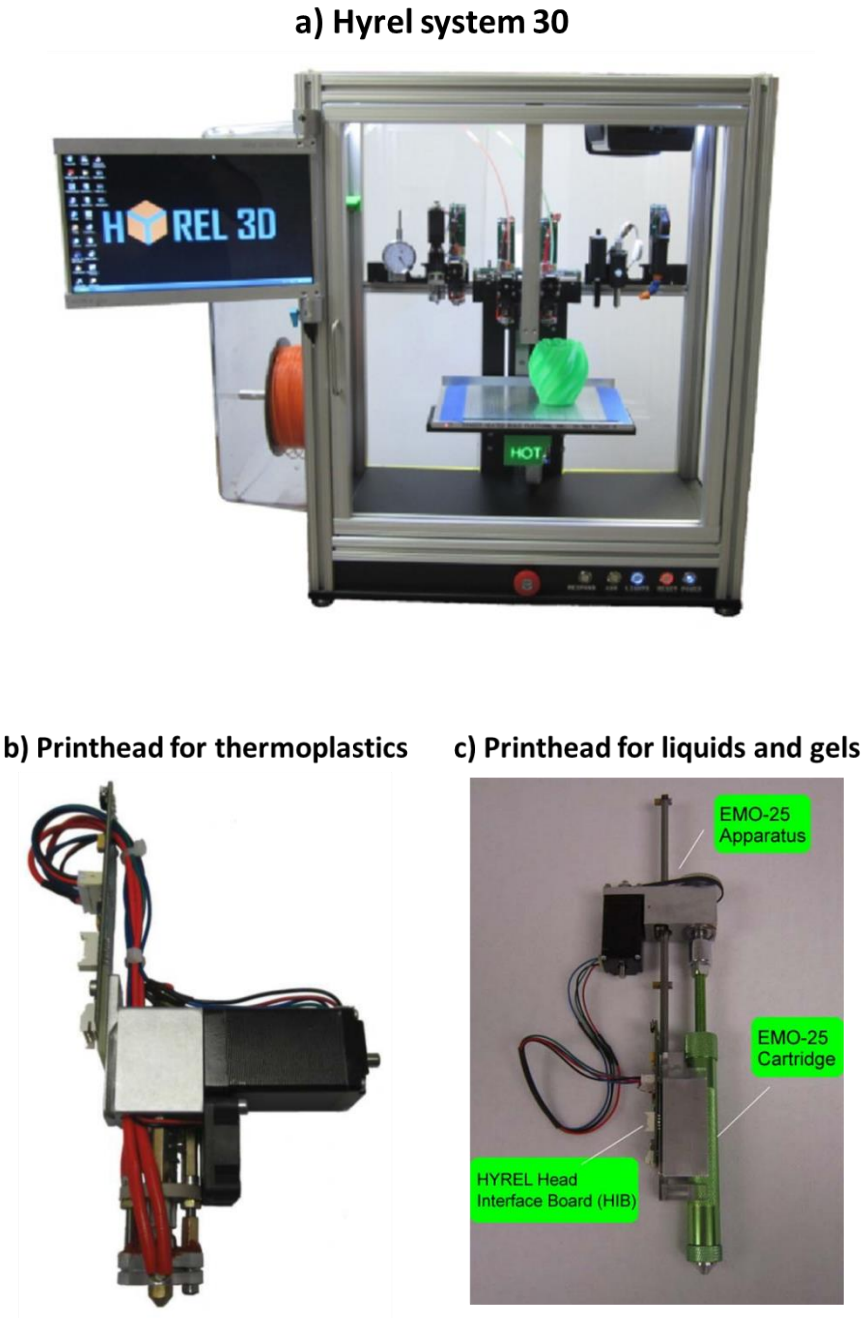

Figure 1.2: (a) Hyrel system 30, a FDM type 3D printer (b) printhead based on pinch roller mechanism used for 3D printing thermoplastics (c) printhead with a piston mechanism used for 3D printing with cross-linkable liquids and gels. Source: www. hyrel3d.com.

3D printing technologies have drastically evolved in the last decade. Professional grade 3D printers are capable of producing high quality parts mainly since they have been optimized for use with a limited number of materials and do not allow the user to change process parameters. Conversely, Fused Deposition Modeling (FDM) has emerged as a favorite due to widespread availability of low-cost open-architecture machines that permit extensive experimentation with any number of materials. The FDM 3D printing process operates by feeding thermoplastic filament through a heated nozzle while the nozzle extrudes the desired pattern one layer on top of another.

A FDM type 3D printer from Hyrel has been utilized for my research. A unique feature of this printer is that it allows the user to swap between two different printheads (a) a heated printhead with a fixed nozzle diameter of 0.5 mm for printing thermoplastics and (b) a non-heated syringe type printhead for printing liquids and gels. The 3D printer and the two printheads are shown in **Figure 1.2**. The syringe type printhead design was modified to allow temperature control required for printing Matrigel® as described in chapter 4. A combination of printheads can be used at a time and the maximum number of printheads allowed for a given print is four. This opens up the possibilities of multi-nozzle printing which we have utilized for 3D printing cell-laden Matrigel® constructs.

1.4 References

[1] M. Zannotti, R. Giovannetti, C. A. D'Amato, and E. Rommozzi, "Spectroscopic studies of porphyrin functionalized multiwalled carbon nanotubes and their interaction with TiO2 nanoparticles surface," *Spectrochim Acta Part A Mol Biomol Spectrosc*, vol. 153, pp. 22–29, 2016.

[2] M. Endo, T. Hayashi, Y. A. Kim, M. Terrones, and M. S. Dresselhaus, "Applications of Carbon Naotubes in the Twenty-First Century," *Philos Trans R Soc A Math Phys Eng Sci*, vol. 362, no. 1823, pp. 2223–2238, 2004.

[3] S. Iijima, "Helical microtubules of graphitic carbon," *Nature*, vol. 354, pp. 56–58, 1991.

[4] S. Basu-Dutt, M. L. Minus, R. Jain, D. Nepal, and S. Kumar, "Chemistry of Carbon Nanotubes for Everyone," *J Chem Educ*, vol. 89, no. 2, pp. 221–229, Jan. 2012.

[5] E. Bekyarova, M. E. Itkis, N. Cabrera, B. Zhao, A. Yu, J. Gao, and R. C. Haddon, "Electronic properties of single-walled carbon nanotube networks.," *J Am Chem Soc*, vol. 127, no. 16, pp. 5990–5, Apr. 2005.

[6] H. J. Qi, K. B. K. Teo, K. K. S. Lau, M. C. Boyce, W. I. Milne, J. Robertson, and K. K. Gleason, "Determination of mechanical properties of carbon nanotubes and vertically aligned carbon nanotube forests using nanoindentation," *J Mech Phys Solids*, vol. 51, no. 11–12, pp. 2213–2237, Nov. 2003.

[7] P. Kim, L. Shi, A. Majumdar, and P. McEuen, "Thermal Transport Measurements of Individual Multiwalled Nanotubes," *Phys Rev Lett*, vol. 87, no. 21, pp. 215502-1-215502–4, Oct. 2001.

[8] A. Thess, R. Lee, P. Nikolaev, H. Dai, P. Petit, C. Xu, Y. H. Lee, S. G. Kim, A. G. Rinzler, D. T. Colbert, G. E. Scuseria, D. Tománek, J. E. Fischer, R. E. Smalley, J. Robert, and D. Tomanek, "Crystalline Ropes of Metallic Carbon Nanotubes," *Science (80-)*, vol. 273, no. 5274, pp. 483–487, 1996.

[9] Chua Chee Kai, "Three-dimensional rapid prototyping technologies and key development areas," *Comput Control Eng J*, vol. 5, no. 4, p. 200, 1994.

[10] D. Pham and R. . Gault, "A comparison of rapid prototyping technologies," *Int J Mach Tools Manuf*, vol. 38, no. 10–11, pp. 1257–1287, 1998.

Chapter 2 – Cross-linked Carbon Nanotube Aerogels

2.1 INTRODUCTION

Aerogel is an open-celled, microporous, solid foam that is composed of a network of interconnected structures and that exhibits porosity (non-solid volume) of no less than 50%. The term aerogel was first introduced by Kistler in 1931 to designate gels in which the liquid was replaced with a gas, without collapsing the gel solid network [1].

A variety of aerogels, such as inorganic SiO_2, TiO_2, Al_2O_3, etc., and organic resorcinol/formaldehyde (RF), melamine/formaldehyde (MF), etc., can be generally prepared from molecular precursors by sol–gel processing and by subsequent supercritical drying or freeze drying to replace the solvents in the wet gels with air [2, 3]. Aerogels offer unique characteristics such as extremely low densities ($0.004 – 0.5$ g/cm^3) and high surface areas ($100 – 1600$ m^2/g) [4]. Based on these properties, silica aerogels have applications in thermal and acoustic insulation, nuclear waste storage, catalysis, whereas organic aerogels have been applied in electronic devices, hydrogen and energy storage [5, 6].

2.2 BACKGROUND

2.2.1 Common aerogels and their synthesis

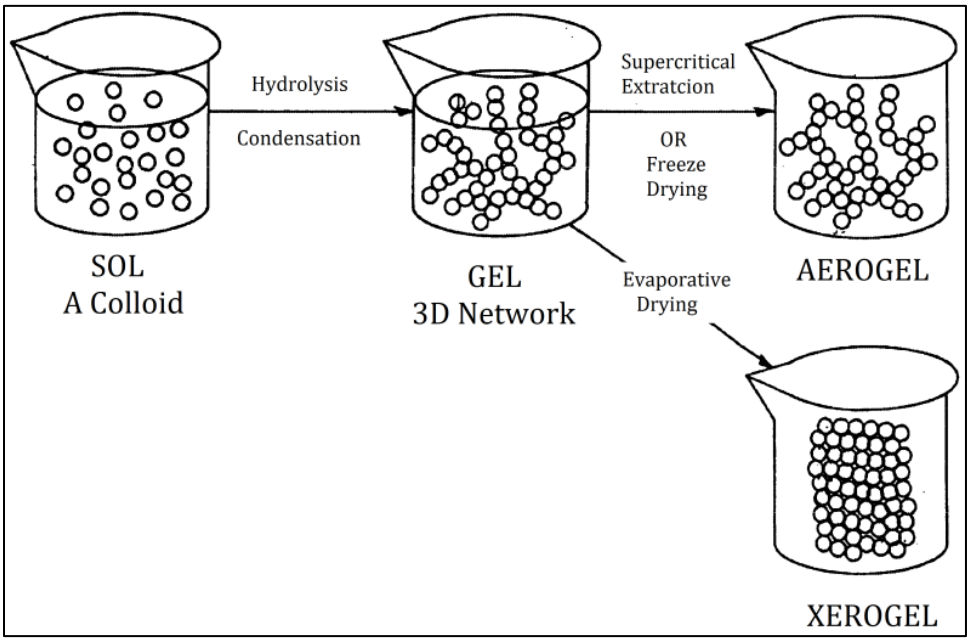

Figure 2.1: General strategy for making aerogels. Reprinted from US Patent # US6666935 B1

A variety of aerogels have been studied, prepared and used successfully. Most widely available aerogels include the ones made from silica, metal oxides and organics. Carbon aerogels can be prepared from organic aerogels via pyrolysis [7]. The formation of aerogels, in general, involves two major steps, the formation of a wet gel, and the drying of the wet gel to form an aerogel **(Figure 2.1)** [8]. The starting material is a colloidal solution of the precursor referred to as 'sol' which then undergoes a) hydrolysis and condensation for silica and metal oxide aerogels [9] and b) addition and condensation for organic aerogels [10] to form the 3D network structure – "gel". Typically, evaporative drying of the gel leads to extensive shrinkage of the network structure. This shrinkage is caused by the surface tension of the solvent which exerts a pull on the solid structure

as the liquid evaporates. The material thus obtained is termed as 'xerogel' [11]. Shrinkage of the network structure can be extensively minimized if the gel is dried by using either the supercritical extraction method or by freeze drying [12].

2.2.2 Carbon nanotube aerogels

Despite their great potential, pristine CNTs tend to aggregate as they are processed or incorporated into macroscopic articles such as fibers, films, and composites. The lack of precise control on CNT nano/microstructure has, in many cases, led to only moderate improvements in material properties. One way to overcome this challenge is to investigate and research on preparing functional bulk materials where individual CNTs form the structure. By combining properties of individual CNTs with those of aerogels, a new class of material becomes accessible with unique multifunctional material properties, which may find applications in fuel cells, super capacitors, batteries, advanced catalyst supports, energy absorption materials, multifunctional composites, chemical and biological sensors, etc. [13].

The reported methods for making CNT aerogels are different from those for preparing conventional aerogels. Bryning and coworkers created CNT aerogel by using an aqueous-gel precursor made by dispersing the CNTs in sodium dodecylbenzene sulfonate (SDBS) [14]. However, they were restricted by the loading density of CNTs due to their aggregation tendency above 13 mg/ml with SDBS : CNT weight ratio of 5:1. They showed that unreinforced aerogels were fragile; however, reinforcement with poly vinyl alcohol (PVA) improved their strength and stability and were able to support at least 8000 times their own weight. On the downside, PVA reinforcement led to a drop in electrical conductivity of the aerogels. The electrical conductivities

dropped from 1 S/cm for unreinforced aerogels to 10^{-5} S/cm for aerogels reinforced by 1 wt% PVA.

To improve on the electrical conductivity, Worsley and coworkers prepared a Carbon Aerogel (CA) composite from an aqueous dispersion of surfactant-stabilized double-walled carbon nanotubes (DWNTs) in an aqueous medium [15]. This approach allowed distribution of CNTs in the CA matrix which was prepared through the sol-gel polymerization of resorcinol and formaldehyde. Subsequent supercritical drying and pyrolysis in an inert atmosphere resulted in CA-CNT composite aerogels. With 8 wt% DWNTs, there was a two-fold increase in the electrical conductivity. The electrical conductivity for DWNT-CA composite increased with increasing DWNT loading, but again was limited by the fact that it became increasingly difficult to keep the CNTs dispersed (above 8 wt%) while cross-linking the sol.

Nabeta and Sano prepared sponge-like bulk materials from CNTs [16]. They prepared them by freeze-drying acidified CNTs dispersed in gelatin solution. In their samples, porous structures were derived from the self-networking nature of gelatin and appeared after freeze-drying. Leroy *et al*. also employed the freeze-drying technique to produce solid foams from CNTs, wherein the porous structure was obtained by bubbling during the freezing step [17]. Abarrategi *et al*. developed CNTs derived scaffolds by freeze-drying chitosan containing dispersed CNTs and showed the applicability of the prepared bulk sample to tissue engineering [18]. These reports have demonstrated that porous bulk foams can be produced from CNTs with the aid of an agent which helps to disperse the CNTs in a starting solution, stabilize the dispersion, and keeps bulk structure from collapsing after freeze-drying. It is a great challenge to keep the CNTs dispersed during the entire process of gelation owing to their intrinsic aggregation tendency. However, if

individual CNTs are kept dispersed while gelation there are high chances of developing bulk samples which would display characteristics close to the original CNTs in the resulting bulk matrix.

Interestingly, to our knowledge, no one has reported a CNT aerogel made of a chemically cross-linked CNT network. Although networks of CNTs have been observed transiently in furnaces while spinning CNT fibers, such an approach does not permit experimental control over the resulting network [19]. Fabricating aerogels with CNTs offers potential for improvement over current carbon aerogel technologies in device applications such as sensors, actuators, electrodes, and thermoelectrics [20].

2.3 PROJECT DESCRIPTION

2.3.1 Objective

There have been a few reports [14, 15, 21] showing successful processing of CNTs into aerogels. Also, much work has been done using either pristine or functionalized CNTs forming physically cross-linked network structures that help reduce the shrinkage and prevent the collapse of the network during solvent evaporation to form the aerogel. In this project, we propose to functionalize carbon nanotubes (CNTs) and then cross-link the functional groups on CNTs to form the network structure using well established isocyanate chemistry. The solvent in the cross-linked CNT network will then be removed by freeze-drying to form the aerogel.

2.3.2 Motivation

CNTs are nanoscale fibers with a persistence length (L_p) on the orders of tens of micrometers [22], orders of magnitude larger than that of rigid rod polymers (L_p of PBT ~ 450 A^o) [23]. Chemically cross-linked polymers have been well documented and understood [24–26], but our current understanding of cross-linking nanoscale fibers is rather limited. We hypothesize the chemical cross-linking of CNTs would be different from that of typical polymers based on stiffness and steric hindrance considerations. Besides, the morphology of porous materials is an important factor because the nanostructures, pore properties and microstructure have a significant effect on their applications [27].

2.3.3 Impact

Chemical cross-linking, in general, has been used to improve the mechanical strength of neat CNT films, fibers, and to enhance the interfacial stress transfer between CNTs and the polymer matrix. This research will enable a better understanding of CNT cross-linking, which is relevant for improving the properties of CNT films, fibers and composites in general.

This research resulted in the creation of lightweight, cross-linked, multifunctional CNT-based materials which have a huge demand in application fields like spacecrafts, aircrafts, automobiles, etc. [28] where weight reduction is crucial for reducing energy consumption. Furthermore, properties like high surface area and high electrical conductivity can be exploited for applications like catalyst support, supercapacitors, etc.

2.4 APPROACH

2.4.1 Functionalization

CNTs are considered as attractive candidates for diverse applications owing to their extraordinary properties. Pristine CNTs are only soluble in superacids like oleum, trifluromethanesulfonic acid and chlorosulfonic aicd, however, insoluble in all organic solvents and aqueous solutions thereby limiting their processing and use [29–31]. One possible solution is to introduce functional groups on the tips and sidewalls of the nanotubes which allow improving their dispersibility in a variety of aqueous and organic solvents [29]. Functionalization also tends to minimize the aggregation of CNTs if dispersed in an appropriate solvent. Also, in the absence of aggregation/bundling, nanotube surface area to volume ratio will be very large which will be useful for aerogel production [32]. However, care must be taken to avoid excessive functionalization of the CNTs as that may impair their intrinsic properties by disturbing the sp^2 hybrid structure and even perhaps shortening their length.

In-house functionalization of the CNTs will be advantageous as it will provide a fair basis for comparison between pristine CNTs and the modified ones. And since acid functionalized CNTs are easily dispersible in aqueous medium, they form the central theme of functionalization for this project. Also, we have chosen the aqueous system as water is the preferred solvent which can be freeze dried at fairly easily achievable temperature and vacuum conditions (273.16 K and 0.612 kPa) but this will require an additional step of solvent exchange before freeze-drying the network. Fourier transform infrared spectroscopy (FTIR) is carried out to verify the presence (or absence) of functional groups on the CNTs.

2.4.2 Oxidation

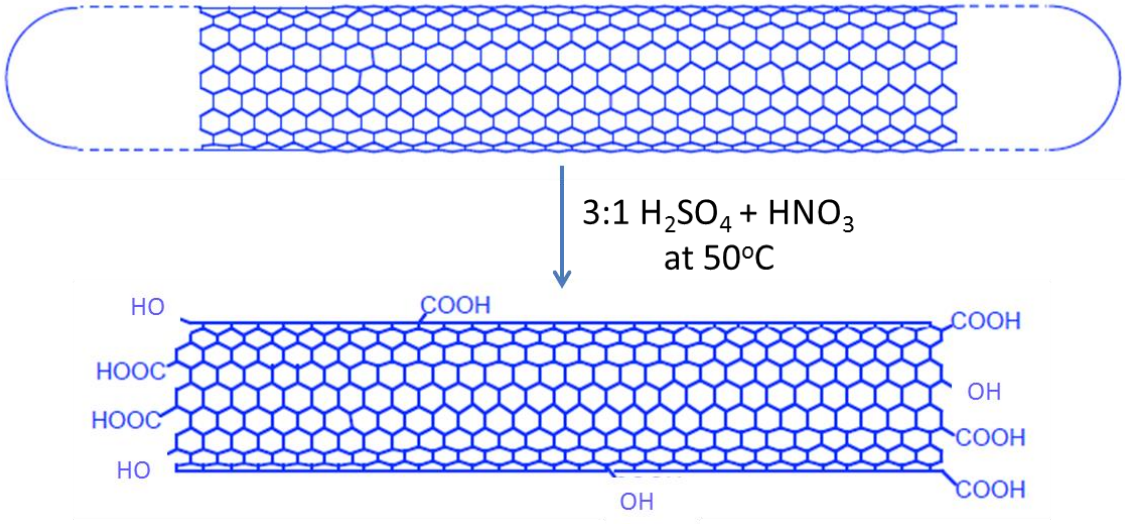

Figure 2.2: Oxidation of pristine CNTs using 3:1 mixture of sulfuric and nitric acid under sonication at 50 °C.

An acid treatment method, as illustrated in **Figure 2.2** and described by Liu *et al*., was used for oxidizing CNTs. CNTs were suspended in a 3:1 v/v mixture of concentrated sulfuric acid & nitric acid and sonicated in a water bath at 50 °C for 3 h [33, 34]. The resultant suspension was then diluted with deionized water and filtered over a 10-µm pore polytetrafluoroethylene (PTFE) membrane. The CNT cake obtained was further washed with deionized water until the water passing through the filter had a pH between 6-7. Oxidized CNTs (o-CNTs) thus obtained were finally freeze-dried at -25 °C for 3 days before use.

2.4.3 CNT Network formation

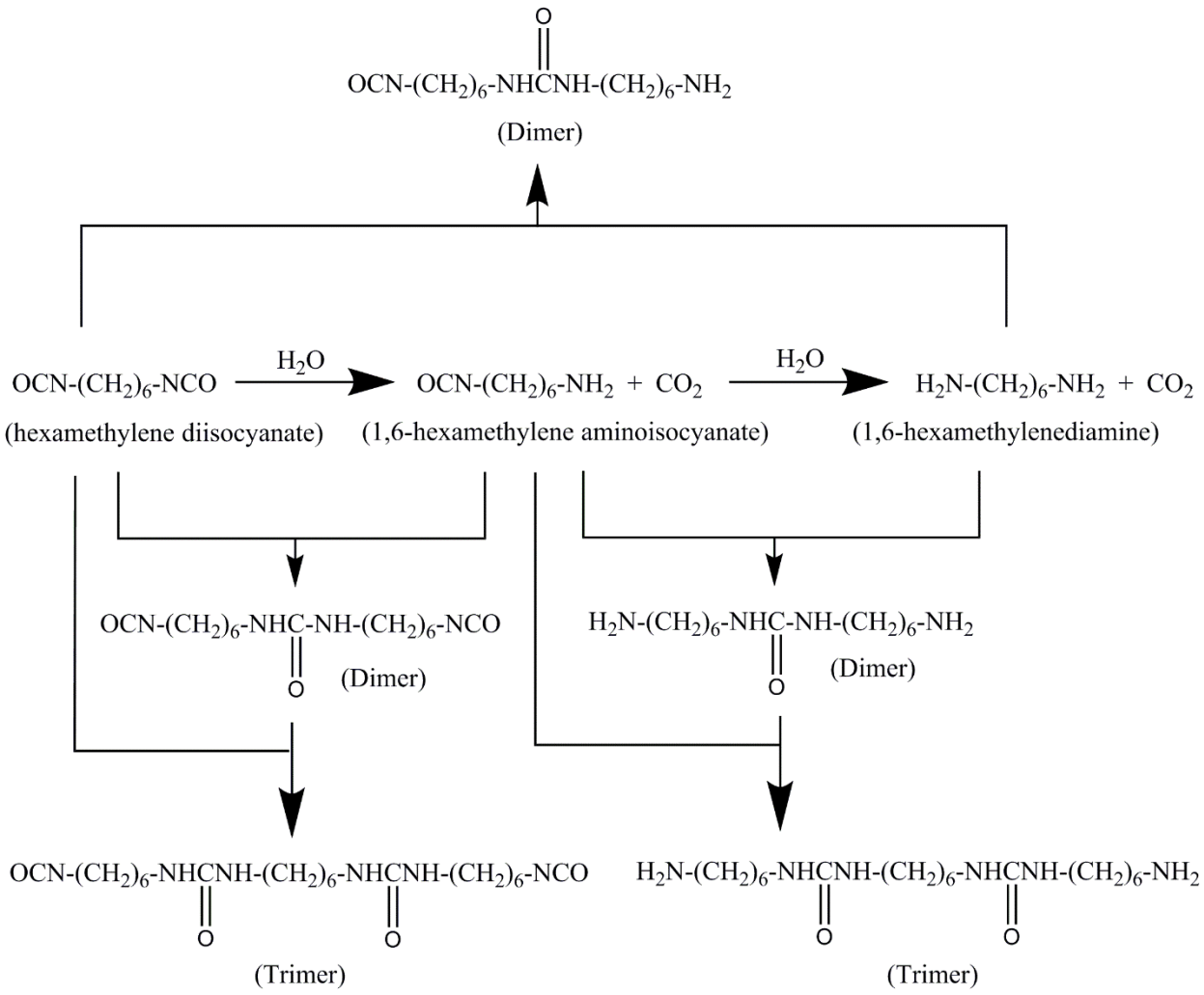

Figure 2.3: Reaction scheme representing hydrolysis of isocyanate functionalities to corresponding amines. The remainder of the reaction scheme represents the potential reactions of hexamethyene diisocyanate (HDI) and the hydrolysis products of HDI. Extended repetition of these reactions results in the formation of high molecular weight polyurea.

The reaction between isocyanate moieties and water is well documented by Kennedy *et al.* [35]. Isocyanates readily react with moisture in the air to form a primary amine. The primary amine thus formed can further react with unreacted isocyanate to form a urea. The reaction scheme for a di-functional isocyanate is shown in **Figure 2.3.** This simple reaction of isocyanate with water can be easily reproduced in lab.

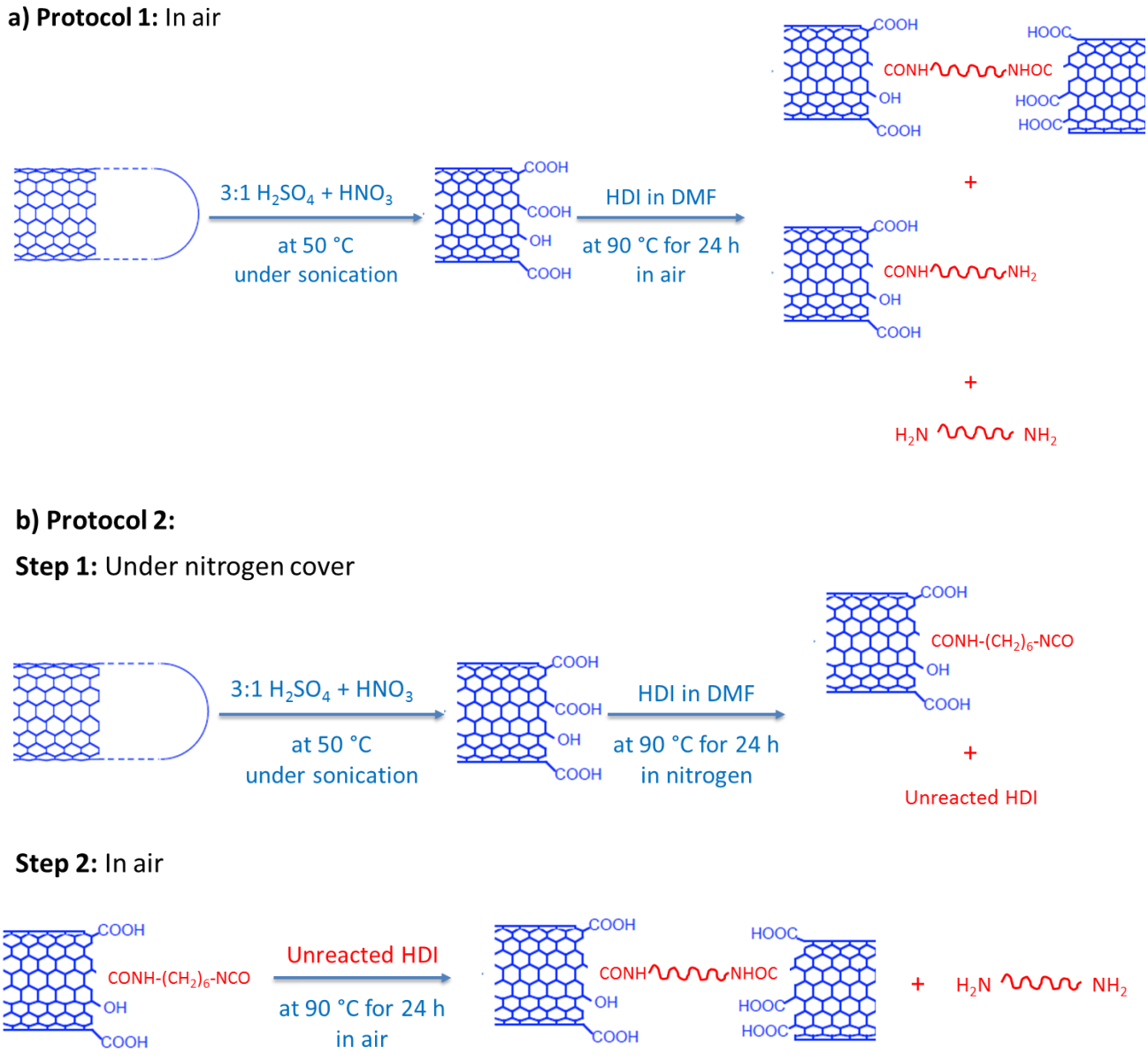

Figure 2.4: (a) Reaction scheme for protocol in air (b) reaction scheme for protocol under nitrogen cover followed by exposure to air.

Oxidized carbon nanotubes (o-CNTs) were reacted with hexamethylene disocyanate (HDI) [36] following two different protocols. First, o-CNTs were dispersed in DMF by sonication for 5 min. HDI was then added to the above dispersion followed by sonication for 1 min. The above mixture was left to stand at 90 ^{0}C in an oil bath. In one experiment, the mixture was kept under nitrogen cover to obtain CNTs with isocyanate functionality (NCO-CNTs). After 24 h, nitrogen cover was removed and the mixture was allowed to stand at 90 $^{\circ}$C for additional 24 h thereby allowing the unreacted isocyanate functionalities to react with moisture in the air forming the polyurea-CNT network structure.

In another experiment, the o-CNT and HDI reaction mixture was kept at 90 $^{\circ}$C for 24 h with no nitrogen cover, thereby shortening the process while providing less time for o-CNTs to react with HDI to form NCO-CNTs.

The gels obtained were washed with THF followed by acetone to remove DMF and any unreacted HDI from the network. Leftover solvents in the network structure were exchanged with water by immersing the samples in excess water without agitation. Water was periodically swapped every 12-24 h and this was continued for 5 days. After solvent exchange, the samples were washed with copious amount of acetone followed by water and freeze-dried for 3 days. **Figure 2.4** explains the two reaction protocols followed.

Since the functionality of HDI is two, HDI by itself cannot cross-link the system. Instead, o-CNTs with multiple reaction sites, links growing chains of polyurea and in the process cross-links the

system. Carrying out the initial reaction in presence of nitrogen allows HDI to react with o-CNTs and therefore, provides with a grafting site which is covalently attached to the CNT surface, from which polymerization can be initiated. Presence of covalent bonding between the polymer matrix and o-CNTs (fillers) allows better stress transfer.

Table 2.1 summaries the samples prepared from different starting concentration of HDI. Weight percentage for HDI in the mixture was calculated using HDI density of 1.047 g/cm^3.

Table 2.1: Sample identification.

Sample	**o-CNT**	**HDI**	**DMF**	**Sample name**
	(mg)	**(µl)**	**(ml)**	
1	160	200	4	56.7% HDI + o-CNT
2	160	400	4	72.4% HDI + o-CNT
3	-	400	4	100% HDI (polymerized, negative control)
4	160	-	4	Control o-CNT
5	-	Liquid	-	HDI Liquid (non-polymerized)

2.5 RESULTS & DISCUSSIONS

2.5.1 Fourier Transform Infrared Spectroscopy

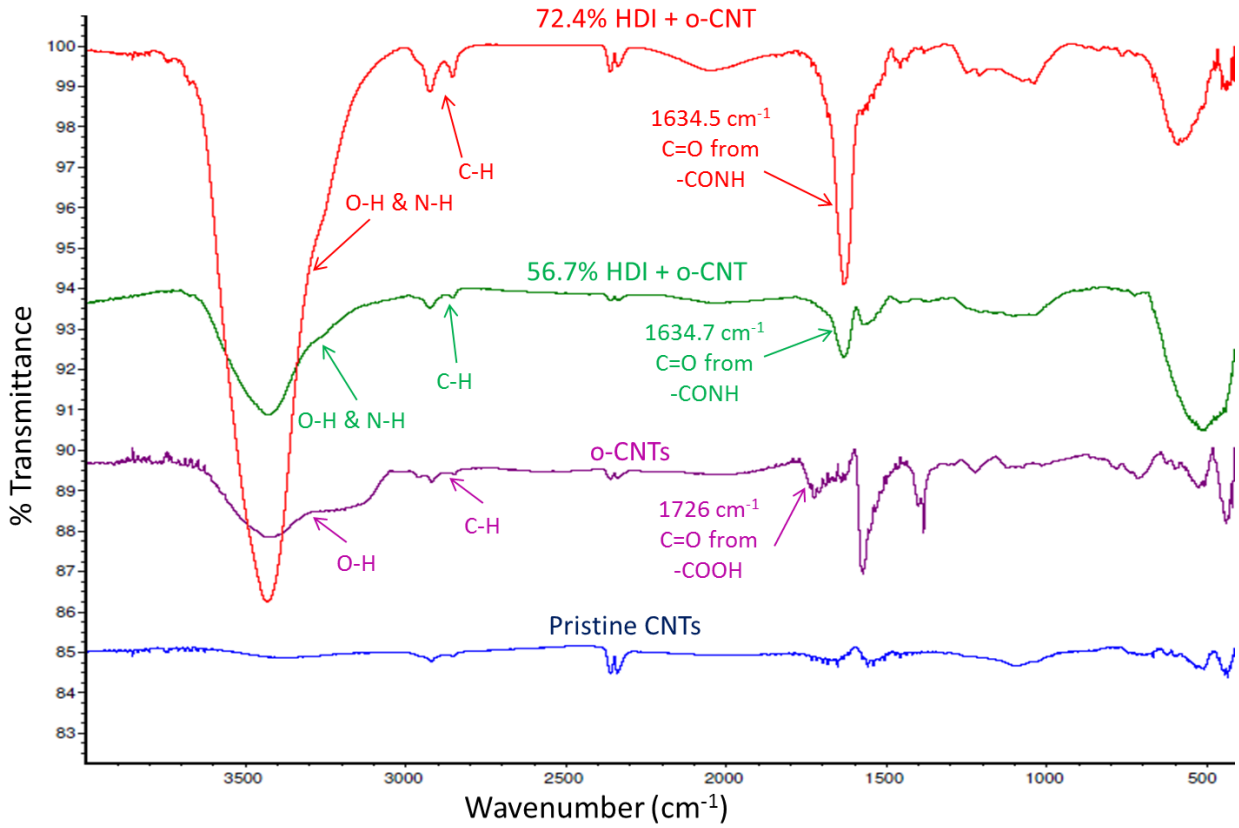

Figure 2.5: FTIR spectra for pristine, oxidized and PUA-CNT networks.

Fourier Transform Infrared Spectroscopy is an informative tool for studying the functional groups attached to CNTs. All samples were studied using Magna-IR 560 Spectrometer, Nicolet by running 1024 scans for each spectrum. **Figure 2.5** shows the FTIR spectra of pristine CNTs, o-CNT and polyurea (PUA)-CNT aerogels. A weak and broad band at ~3400 cm^{-1} is attributed to the presence -OH groups on the surface of the as-received CNTs and is hypothesized to originate from the adsorbed or ambient moisture tightly bond onto the nanotube surface [37]. For o-CNTs, the

appearance of the peak at 1726 cm^{-1} is assigned to the stretching mode of acid carbonyl suggesting successful oxidation of the nanotubes [37, 38]. Reaction of o-CNTs with HDI forms amide linkages (-CONH) and the downshift of the carbonyl peak from 1726 cm^{-1} to 1634 cm^{-1} is attributed to this phenomenon [36, 39].

2.5.2 Raman Spectroscopy

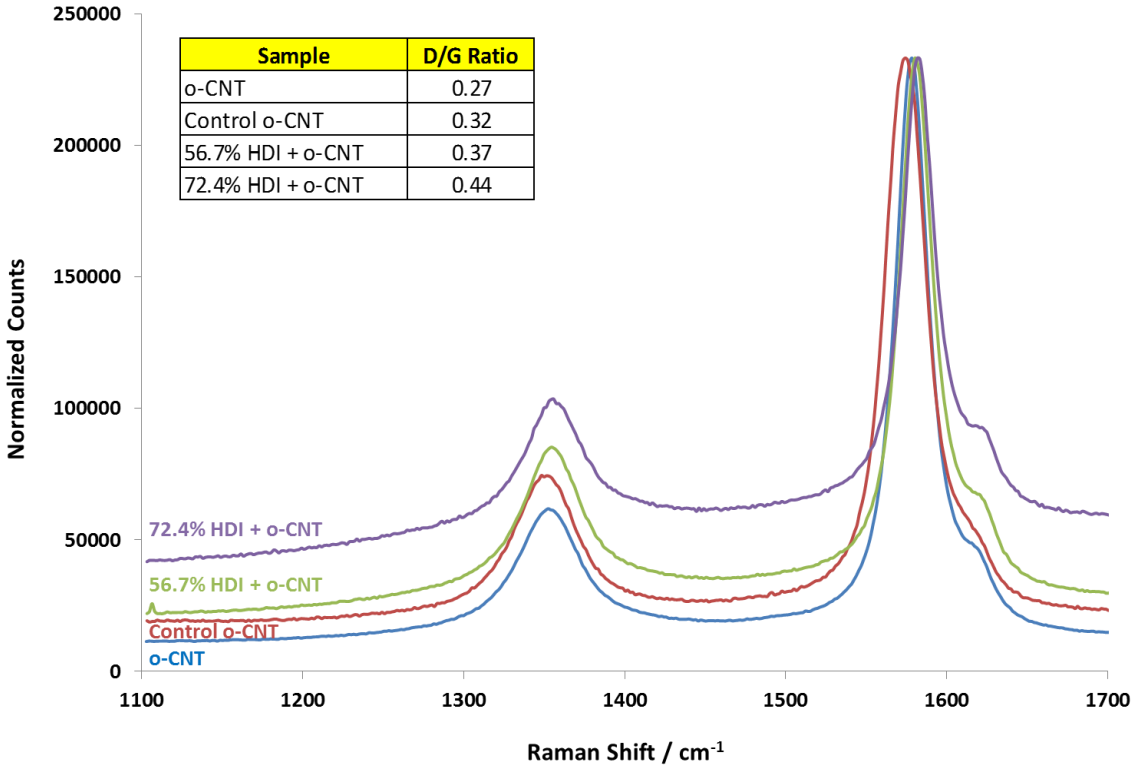

Figure 2.6: Raman spectra for PUA-CNT networks and their components.

Raman spectroscopy (Renishaw System 2000; 514 nm) was carried out on pristine and functionalized CNTs. Raman spectrum obtained from these samples are shown in **Figure 2.6**. The ratio of the D-band to G-band for pristine CNTs is 0.27, indicating the as-received CNTs are rather defect-free [40, 41]. After oxidation and subsequent reactions with HDI, this ratio increased from

0.27 to 0.44 as more of the sp2 hybridized carbon get converted to sp3 hybridized carbon. This indicates successful functionalization of CNTs and polymerization of HDI into PUA.

2.5.3 Thermal Properties:

Thermal properties of the prepared aerogels were characterized using thermogravimetric analysis (TGA) and differential scanning calorimetry (DSC). These techniques in combination provide an extensive information on the thermal behavior of the aerogels and their components.

Thermogravimetric analysis (TGA):

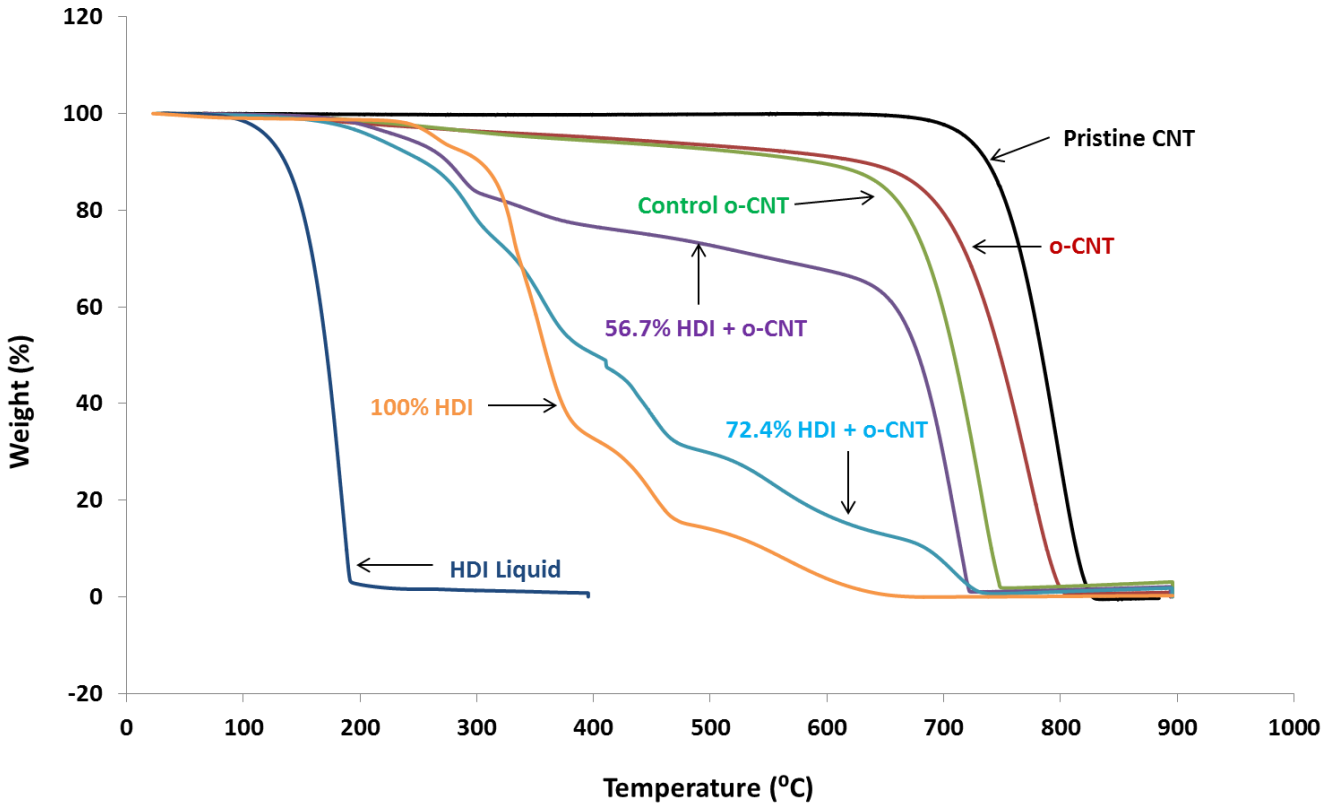

Figure 2.7: Weight loss profile for aerogels and their components in air.

TA Instruments TGA Q-500 was used for thermogravimetric analysis of the samples. Samples were cut into a small piece weighing about 10 mg for TGA**.** All the samples were analyzed using air and an arbitrarily chosen temperature ramp rate of 10 °C/min. Weight loss profile as a function of temperature provides a good indication of thermal stability of a given sample. Thermal degradation temperature is taken as the maximum of the first derivative of weight loss with respect to temperature from TGA results. Thermal degradation temperatures for different samples are tabulated in **Table 2.2**.

Table 2.2: Thermal degradation temperatures.

Sample	**Degradation Temperature (°C)**	
	PUA	**CNT**
Pristine CNT	-	796.4
o-CNT	-	773.6
Control o-CNT	-	733.8
56.7% HDI + o-CNT	285.64	712.4
72.4% HDI + o-CNT	292.7	708.5
100% HDI	265.8	-
HDI Liquid	184.97	-

Figure 2.7 shows that pristine CNTs are thermally stable up to a temperature of 796.4 °C and typically starts to degrade via oxidation under ambient air environment at such high temperature [42]. o-CNTs which have more defect sites on the wall and on the tube ends degrade much before

pristine CNTs. The results show a difference in the degradation temperature between o-CNTs (773.6 °C) and control o-CNTs (733.8 °C) which may be coming from creating more defects while sonicating the o-CNTs in DMF for sample preparation. This observation is in agreement with data obtained from Raman spectroscopy indicating a higher D/G ratio; i.e., more defects on control o-CNT sample.

The first derivative of weight loss with respect to temperature for 56.7% HDI + o-CNT gives two maxima. Weight loss observed at 285.6 °C is due to degradation of polyurea in the aerogel sample. About 17% weight loss was detected at 300 °C, and about 25% of the aerogel decomposed at 400 °C. The residue was stable until 600 °C, after which the CNTs in the system start to degrade. For 72.4% HDI + o-CNT sample, multiple peaks for the derivative of weight loss with respect to temperature are observed, similar to those observed for 100% HDI sample. This is an indication of presence of polyureas with different thermal stability. Primary cause for such an observation is speculated to arise from the complex nature of HDI polymerization observed in presence of moisture which could result in polyureas with different molecular weights. A 50% weight loss was observed at 400 °C and about 83% of 72.4% HDI + o-CNT sample degrades by 600 °C. The final weight loss at 708.5 °C is attributed to o-CNTs.

The polyurea formed using 100% HDI shows an initial degradation at 265.8 °C followed by a major weight loss at 331 °C and about 96.3% material is lost by 600 °C. Boiling point for HDI is 255 °C, however, since the sample pan is open to air while running the TGA experiments, weight loss at 185 °C is attributed to HDI evaporation during experiment.

Differential Scanning Calorimetry:

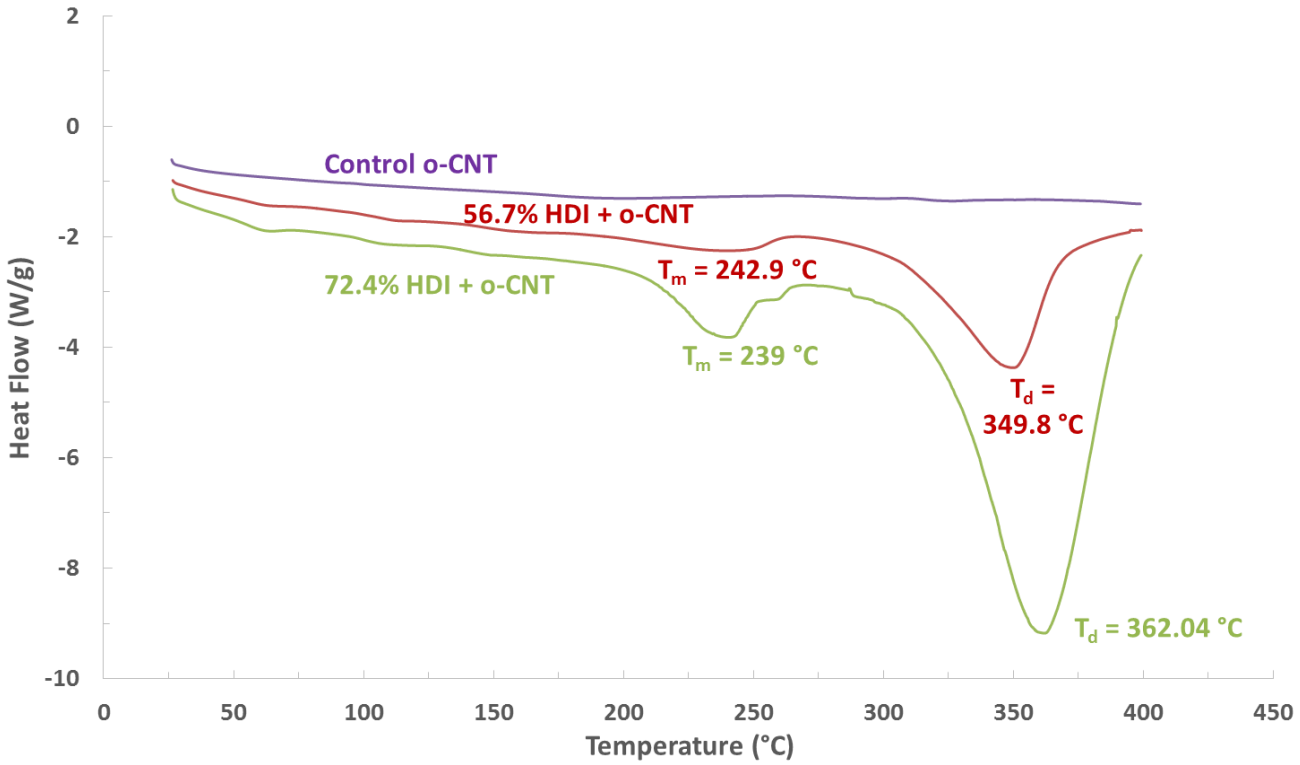

Figure 2.8: Thermal transitions from DSC.

Thermal transitions of the samples were analyzed using TA Instruments DSC Q-100. The sample was equilibrated at the initial temperature for 5 minutes before increasing to a final temperature of 400 °C at a ramp rate of 10 °C/min.

DSC test shown in **Figure 2.8** indicates fluctuations in the heat flow observed above 230 °C, there was no obvious glass transition temperature (T_g) within the scanned temperature range from 25 °C to 400 °C. This is a characteristic of polyurea attributed to the presence of strong hydrogen bonding in the polymer. Similar results have been observed in a number of studies [43–46]. The strong hydrogen bonding "freezes" most of the polymer segments and thereby imparts partial crystallinity

to the polymer. The free movement of polymer chains and segments is severely restricted until the melting temperature is reached.

For polyureas synthesized from hexamethylene diisocyanate and hexamethylene diamine, Suresh et al. observed an endothermic DSC peak at about 280 °C, a transition attributed to the melting of the polymer [47]. Given the similarity of the polymer concerned, the likely endothermic fluctuations observed at about 240 °C are due to melting of polyurea in the aerogel samples. Soon after the melting endothermic heat fluctuation, the polymer starts to degrade significantly. This observation is supported by the weight loss profile obtained from TGA as shown in **Figure 2.7**. No thermal transitions are observed for control o-CNT in the temperature range considered for DSC. Thermal transitions are tabulated in **Table 2.3**.

Table 2.3: Thermal transitions observed using DSC.

Sample	Melting Temperature (T_m)	Degradation Temperature (T_d)
	(°C)	(°C)
Control o-CNT	-	-
56.7% HDI + o-CNT	242.9	349.8
72.4% HDI + o-CNT	239	362.04

2.5.4 Electron Microscopy

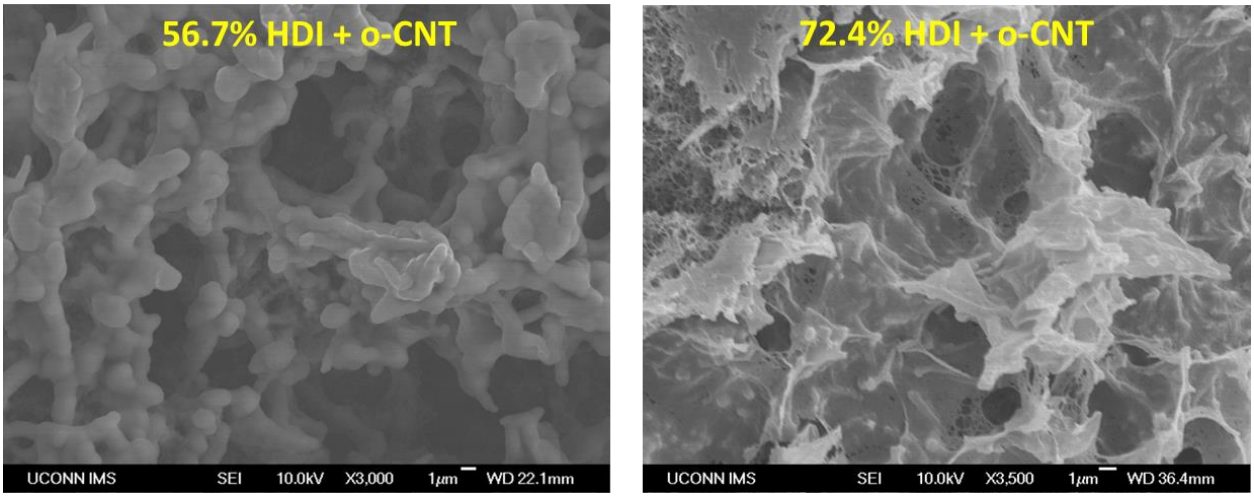

Figure 2.9: SEM micrographs for PUA-CNT network structures.

Scanning electron microscopy (SEM; JEOL 6335 Field Emission SEM) was carried out after sputtering a thin layer (3 - 5 nm) of gold and palladium onto the test sample to prevent charging. The electron beam was generated at 10 kV for all the images. The SEM micrographs aided in observing the microstructure of the PUA-CNT network structures.

The morphology observed for the two samples is completely different as seen in **Figure 2.9**. In the case of 56.7% HDI + o-CNT, polyurea appears to have coated individual CNTs whereas for 72.4% HDI + o-CNT sample, individual CNTs are connected through thin sheet-like polyurea thereby connecting them.

2.5.5 Dynamic Mechanical Analysis

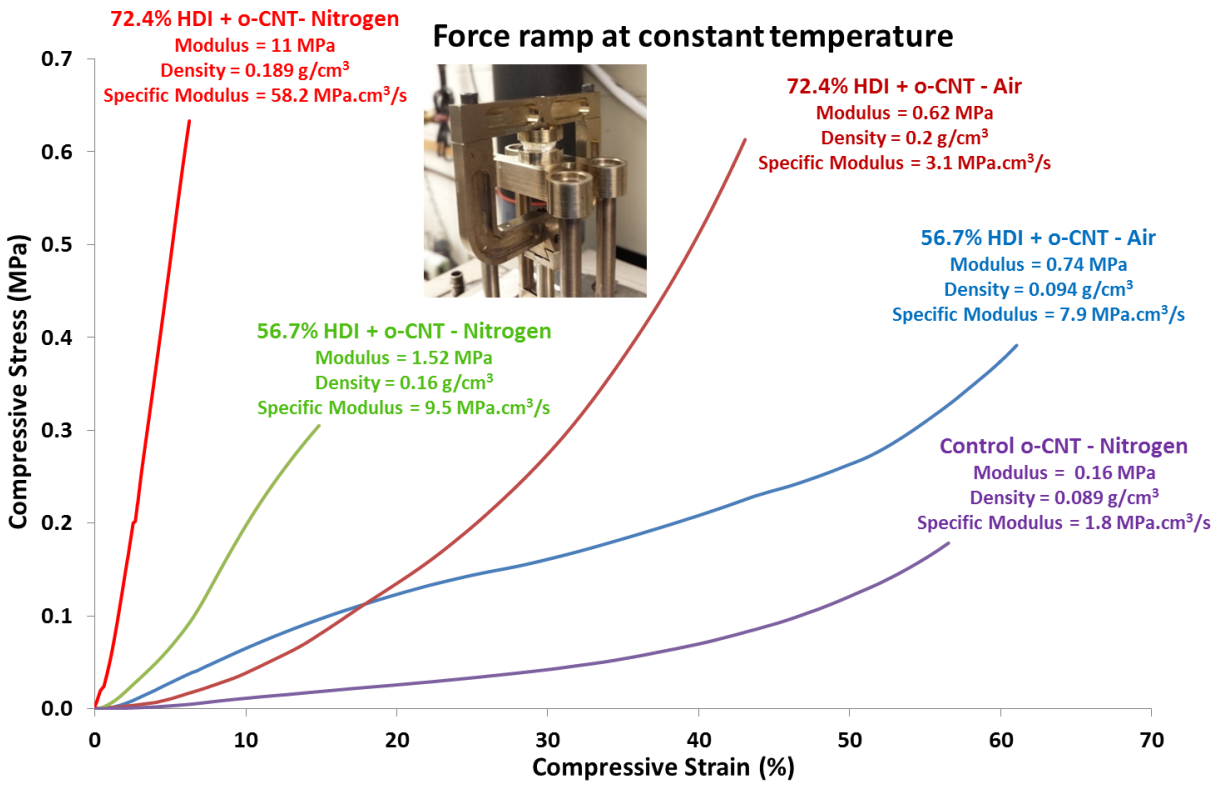

Figure 2.10: Compressive stress vs strain data for aerogel samples.

DMA experiments were carried out under compression for aerogel samples. The samples were first loaded on to the stage and equilibrated at 30 °C followed by keeping it at isothermal conditions for an additional 5 mins. A force ramp of 1 N/min at constant temperature was chosen to obtain the stress-strain curves. Maximum allowed force on the sample was 18 N.

Stress-strain data can further be analyzed to calculate the compression modulus of the aerogels considering the slope in the low strain region of the curve. For all cases, compression modulus was calculated from the slope of the curve between 0% and 2% compression strain. Stiffness of the gels is a direct indication of stress transfer between the matrix and CNTs. In general, higher

stiffness values would indicate better stress transfer between the filler and the matrix material. Indirectly, stiffness can indicate successful cross-linking of CNTs. However, compression tests alone do not provide enough evidence of success cross-linking. Solvent dispersion test is chosen to provide further evidence to confirm cross-linking of CNTs by PUA.

From **Figure 2.10**, it can be seen that the control sample has the lowest specific moduli compared to the rest of the samples. Aerogels prepared directly in air have a lower compression moduli compared to those prepared in nitrogen environment. This confirms that the additional step of reacting HDI with o-CNTs in presence of nitrogen environment (or absence of moisture) helps reinforce the aerogel through covalent bonds between CNTs and polyurea matrix. Density of the network structures was measured using weight by volume method.

2.5.6 Dispersion Tests

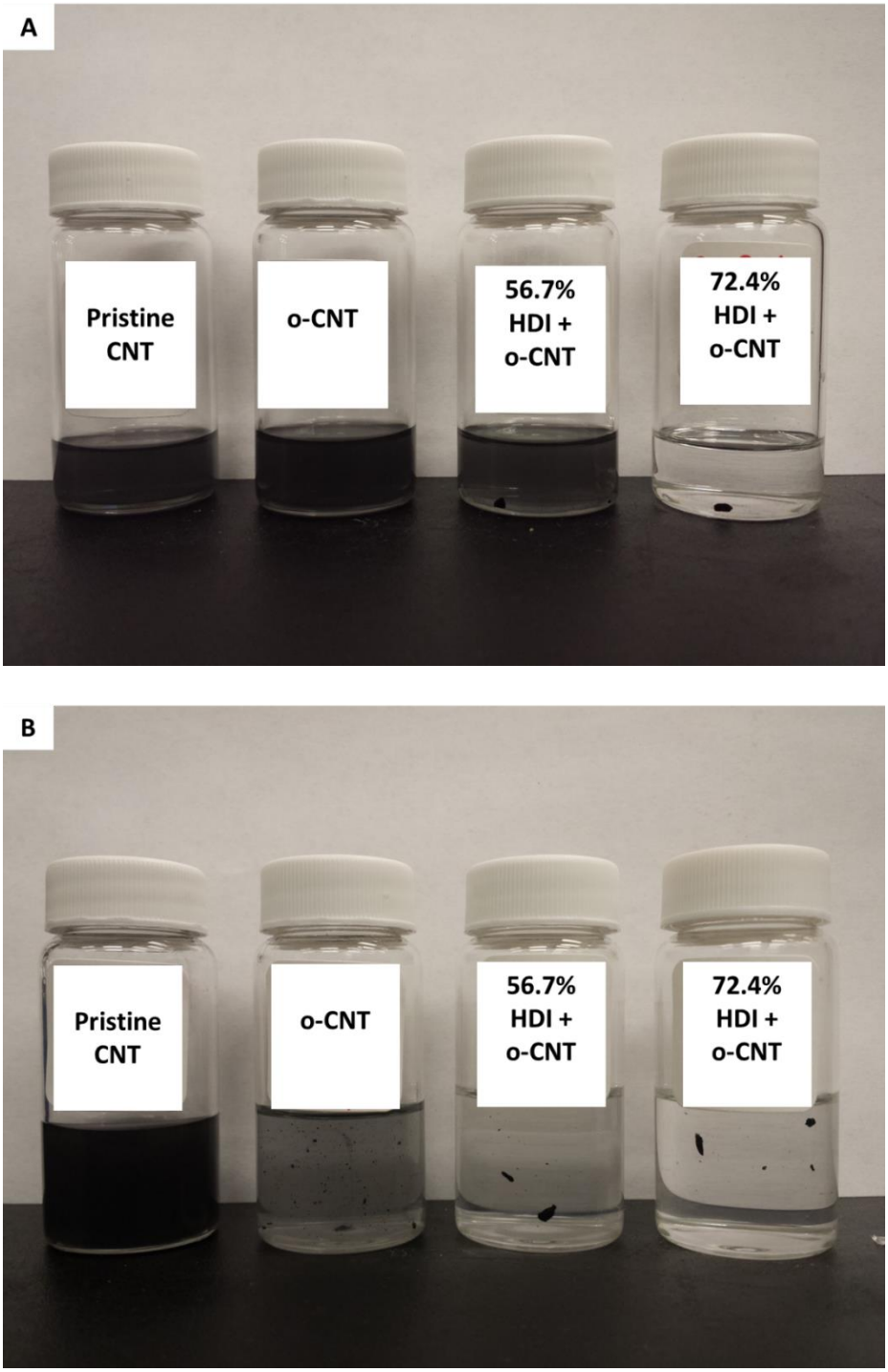

Figure 2.11: (A) dispersed samples in chloroform after 1 min of sonication (B) dispersed samples in PDMS matrix after 10 min of speed mixing.

Dispersion tests were carried out in chloroform (under sonication) and PDMS (under speed mixing using FlackTek Inc., SpeedMixer Dac150.1 FVZ-K). The results are as shown in **Figure 2.11**. Chloroform being a good solvent for PUA can help understand whether the PUA-CNT network is cross-linked or not. It can be seen from the images that the pristine and o-CVD readily disperses in chloroform after 1 min sonication unlike the cross-linked samples. 72.4% HDI + o-CNT remains completely undispersed unlike 56.7% HDI + o-CNT where dispersion is observed but only to a very little extent as the cross linked pellet can still be seen in the photomicrograph. For PDMS, pristine CVD readily disperses upon speed mixing for 10 min. Dispersion quality decreases significantly for o-CNT, 56.7% HDI + o-CNT and 72.4% HDI + o-CNT.

2.6 CONCLUSIONS

Despite their great potential, CNT aerogels suffer from a lack of control on CNT nano/microstructure which in many cases have led to moderate improvements in mechanical properties of the aerogels. A method for preparing CNT aerogels using a relatively simple isocyanate chemistry was explored which relies on the reaction on isocyanate moieties with moisture. Successful functionalization of CNTs was confirmed using Fourier transform infrared spectroscopy and Raman spectroscopy. FTIR helped in establishing and confirming the presence of functional groups on the sides and walls of CNTs. Raman spectroscopy supported the claim of successful functionalization which can be affirmed by following the increasing amount of defects (primarily, presence of sp3 hybridized carbon) on CNTs. Thermal properties were characterized indicating that the aerogels were thermally stable up to a temperature of around 250 °C above which PUA in the system starts to melt and degrade eventually. Scanning electron microscopy helped differentiate between the microstructure of aerogels formed with two different concentrations of HDI. Mechanical properties were characterized using dynamic mechanical analysis which indicated improvement in mechanical robustness of the system with increasing HDI loading and protocol involving nitrogen environment which helps graft PUA on CNT surface thereby improving stress-transfer and ultimately cross-linking the system. Successful cross-linking of the network structure was confirmed by dispersion test in chloroform, a good solvent for PUA. A limitation of the selected protocol comes from potential non-reproducibility arising from day-to-day variations in moisture levels in ambient air.

2.7 REFERENCES

[1] S. S. Kistler, "Coherent Expanded-Aerogels," *J Phys Chem*, vol. 36, no. 1, pp. 52–64, 1931.

[2] A. Soleimani Dorcheh and M. H. Abbasi, "Silica aerogel; synthesis, properties and characterization," *J Mater Process Technol*, vol. 199, no. 1, pp. 10–26, 2008.

[3] K. Kanamori, M. Aizawa, K. Nakanishi, and T. Hanada, "New Transparent Methylsilsesquioxane Aerogels and Xerogels with Improved Mechanical Properties," *Adv Mater*, vol. 19, no. 12, pp. 1589–1593, 2007.

[4] N. Hüsing and U. Schubert, "Aerogels—Airy Materials: Chemistry, Structure, and Properties," *Angew Chemie Int Ed*, vol. 37, no. 1–2, pp. 22–45, 1998.

[5] A. C. Pierre and G. M. Pajonk, "Chemistry of aerogels and their applications.," *Chem Rev*, vol. 102, no. 11, pp. 4243–65, Nov. 2002.

[6] J. Biener, M. Stadermann, M. Suss, M. A. Worsley, M. M. Biener, K. A. Rose, and T. F. Baumann, "Advanced carbon aerogels for energy applications," *Energy Environ Sci*, vol. 4, no. 3, p. 656, 2011.

[7] R. W. Pekala, C. T. Alviso, F. M. Kong, and S. S. Hulsey, "Aerogels derived from multifunctional organic monomers," *J Non Cryst Solids*, vol. 145, pp. 90–98, 1992.

[8] R. L. Simpson, R. S. Lee, T. M. Tillotson, L. W. Hrubesh, R. W. Swansiger, and G. A. Fox, "Sol-gel manufactured energetic materials." Google Patents, 2005.

[9] J. L. Gurav, I.-K. Jung, H.-H. Park, E. S. Kang, and D. Y. Nadargi, "Silica Aerogel: Synthesis and Applications," *Journal of Nanomaterials*, vol. 2010. pp. 1–11, 2010.

[10] S. A. Al-Muhtaseb and J. A. Ritter, “Preparation and Properties of Resorcinol–Formaldehyde Organic and Carbon Gels,” *Adv Mater*, vol. 15, no. 2, pp. 101–114, 2003.

[11] S. Hæreid, E. Nilsen, and M.-A. Einarsrud, “Subcritical drying of silica gels,” *J Porous Mater*, vol. 2, no. 4, pp. 315–324, Dec. 1996.

[12] L. Durães, M. Ochoa, N. Rocha, R. Patrício, N. Duarte, V. Redondo, and A. Portugal, “Effect of the Drying Conditions on the Microstructure of Silica Based Xerogels and Aerogels,” *J Nanosci Nanotechnol*, vol. 12, pp. 1–7, 2011.

[13] X. Gui, J. Wei, K. Wang, A. Cao, H. Zhu, Y. Jia, Q. Shu, and D. Wu, “Carbon nanotube sponges.,” *Adv Mater*, vol. 22, no. 5, pp. 617–21, Feb. 2010.

[14] M. B. Bryning, D. E. Milkie, M. F. Islam, L. a. Hough, J. M. Kikkawa, and a. G. Yodh, “Carbon Nanotube Aerogels,” *Adv Mater*, vol. 19, no. 5, pp. 661–664, Mar. 2007.

[15] M. a Worsley, J. H. Satcher, and T. F. Baumann, “Synthesis and characterization of monolithic carbon aerogel nanocomposites containing double-walled carbon nanotubes.,” *Langmuir*, vol. 24, no. 17, pp. 9763–6, Sep. 2008.

[16] M. Nabeta and M. Sano, “Nanotube foam prepared by gelatin gel as a template.,” *Langmuir Acs J Surfaces Colloids*, vol. 21, no. 5, pp. 1706–1708, 2005.

[17] C. M. Leroy, F. Carn, R. Backov, M. Trinquecoste, and P. Delhaes, “Multiwalled-carbon-nanotube-based carbon foams,” *Carbon N Y*, vol. 45, no. 11, pp. 2317–2320, Oct. 2007.

[18] A. Abarrategi, M. C. Gutiérrez, C. Moreno-Vicente, M. J. Hortigüela, V. Ramos, J. L. López-Lacomba, M. L. Ferrer, and F. del Monte, “Multiwall carbon nanotube scaffolds for tissue engineering purposes.,” *Biomaterials*, vol. 29, no. 1, pp. 94–102, Jan. 2008.

[19] Y.-L. Li, I. A. Kinloch, and A. H. Windle, “Direct Spinning of Carbon Nanotube Fibers

from Chemical Vapor Deposition Synthesis," *Science (80-)*, vol. 304, no. 5668, pp. 276–278, 2004.

[20] T. Bordjiba, M. Mohamedi, and L. H. Dao, "New Class of Carbon-Nanotube Aerogel Electrodes for Electrochemical Power Sources," *Adv Mater*, vol. 20, no. 4, pp. 815–819, Feb. 2008.

[21] M. a. Worsley, P. J. Pauzauskie, S. O. Kucheyev, J. M. Zaug, A. V. Hamza, J. H. Satcher, and T. F. Baumann, "Properties of single-walled carbon nanotube-based aerogels as a function of nanotube loading," *Acta Mater*, vol. 57, no. 17, pp. 5131–5136, Oct. 2009.

[22] N. Fakhri, D. A. Tsyboulski, L. Cognet, R. B. Weisman, and M. Pasquali, "Diameter-dependent bending dynamics of single-walled carbon nanotubes in liquids," *Proc Natl Acad Sci U S A*, vol. 106, no. 34, pp. 14219–14223, Aug. 2009.

[23] R. Zhang and W. L. Mattice, "Evaluation of the persistence length of the rigid-rod polymers poly(benzobisoxazole) and poly(benzobisthiazole) using molecular-dynamics simulations," *Macromolecules*, vol. 25, no. 19, pp. 4937–4941, 1992.

[24] M. T. Shaw, *Introduction to Polymer Rheology*, John Wiley & Sons, Inc., 2011, pp. 239–259.

[25] H. H. Winter and F. Chambon, "Analysis of Linear Viscoelasticity of a Crosslinking Polymer at the Gel Point," *J Rheol (N Y N Y)*, vol. 30, no. 2, p. 367, 1986.

[26] F. Chambon and H. H. Winter, "Linear Viscoelasticity at the Gel Point of a Crosslinking PDMS with Imbalanced Stoichiometry," *J Rheol (N Y N Y)*, vol. 31, no. 8, pp. 683–697, Nov. 1987.

[27] S.-M. Kwon, H.-S. Kim, and H.-J. Jin, "Multiwalled carbon nanotube cryogels with

aligned and non-aligned porous structures," *Polymer (Guildf)*, vol. 50, no. 13, pp. 2786–2792, Jun. 2009.

[28] X. Zhang, J. Liu, B. Xu, Y. Su, and Y. Luo, "Ultralight conducting polymer/carbon nanotube composite aerogels," *Carbon N Y*, vol. 49, no. 6, pp. 1884–1893, May 2011.

[29] D. Tasis, N. Tagmatarchis, A. Bianco, and M. Prato, "Chemistry of carbon nanotubes.," *Chem Rev*, vol. 106, no. 3, pp. 1105–36, Mar. 2006.

[30] L. M. Ericson, H. Fan, H. Peng, V. A. Davis, W. Zhou, J. Sulpizio, Y. Wang, R. Booker, J. Vavro, C. Guthy, A. N. G. Parra-Vasquez, M. J. Kim, S. Ramesh, R. K. Saini, C. Kittrell, G. Lavin, H. Schmidt, W. W. Adams, W. E. Billups, M. Pasquali, W.-F. Hwang, R. H. Hauge, J. E. Fischer, and R. E. Smalley, "Macroscopic, Neat, Single-Walled Carbon Nanotube Fibers10.1126/science.1101398," *Science (80-)*, vol. 305, no. 5689, pp. 1447–1450, 2004.

[31] S. Ramesh, L. M. Ericson, V. A. Davis, R. K. Saini, C. Kittrell, M. Pasquali, W. E. Billups, W. W. Adams, R. H. Hauge, and R. E. Smalley, "Dissolution of pristine single walled carbon nanotubes in superacids by direct protonation," *J Phys Chem B*, vol. 108, no. 26, pp. 8794–8798, 2004.

[32] M. B. Bryning, D. E. Milkie, M. F. Islam, L. A. Hough, J. M. Kikkawa, and A. G. Yodh, "Carbon Nanotube Aerogels," *Adv Mater*, vol. 19, no. 5, pp. 661–664, 2007.

[33] J. Liu, "Fullerene Pipes," *Science (80-)*, vol. 280, no. 5367, pp. 1253–1256, May 1998.

[34] W. Song and A. H. Windle, "Isotropic - Nematic Phase Transition of Dispersions of Multiwall Carbon Nanotubes," pp. 6181–6188, 2005.

[35] A. Kennedy and W. Brown, "Isocyanates and Lung Disease: Experimental Approaches to

Molecular Mechanisms," *Occup Med (Philadelphia, PA)*, vol. 7, no. 2, pp. 301–329, 1992.

[36] N. Leventis, C. Chidambareswarapattar, D. P. Mohite, Z. J. Larimore, H. Lu, and C. Sotiriou-Leventis, "Multifunctional porous aramids (aerogels) by efficient reaction of carboxylic acids and isocyanates," *J Mater Chem*, vol. 21, no. 32, p. 11981, 2011.

[37] T. Ramanathan, F. T. Fisher, R. S. Ruoff, and L. C. Brinson, "Amino-Functionalized Carbon Nanotubes for Binding to Polymers and Biological Systems," *Chem Mater*, vol. 17, no. 6, pp. 1290–1295, Mar. 2005.

[38] H. Peng, L. B. Alemany, J. L. Margrave, and V. N. Khabashesku, "Sidewall Carboxylic Acid Functionalization of Single-Walled Carbon Nanotubes," no. 10, pp. 15174–15182, 2003.

[39] Y. Wang, Z. Iqbal, and S. V. Malhotra, "Functionalization of carbon nanotubes with amines and enzymes," *Chem Phys Lett*, vol. 402, no. 1–3, pp. 96–101, Jan. 2005.

[40] S. Osswald, M. Havel, and Y. Gogotsi, "Monitoring oxidation of multiwalled carbon nanotubes by Raman spectroscopy," *J Raman Spectrosc*, vol. 38, no. 6, pp. 728–736, Jun. 2007.

[41] S. R. Vora, B. Bognet, H. S. Patanwala, F. Chinesta, and A. W. K. Ma, "Surface pressure and microstructure of carbon nanotubes at an air-water interface," *Langmuir*, vol. 31, no. 16, pp. 4663–4672, 2015.

[42] E. T. Thostenson, C. Li, and T.-W. Chou, "Nanocomposites in context," *Compos Sci Technol*, vol. 65, no. 3, pp. 491–516, 2005.

[43] Y. Yang, X. Jiang, X. Zhu, and X. Z. Kong, "A facile pathway to polyurea nanofiber fabrication and polymer morphology control in copolymerization of oxydianiline and

toluene diisocyanate in acetone," *RSC Adv*, vol. 5, no. 10, pp. 7426–7432, 2015.

[44] S. S. Dhumal and A. K. Suresh, "Understanding interfacial polycondensation: Experiments on polyurea system and comparison with theory," *Polymer (Guildf)*, vol. 51, no. 5, pp. 1176–1190, 2010.

[45] L. Ning, W. De-Ning, and Y. Sheng-Kang, "Crystallinity and hydrogen bonding of hard segments in segmented poly(urethane urea) copolymers," *Polymer (Guildf)*, vol. 37, no. 16, pp. 3577–3583, 1996.

[46] X. Z. Kong, W. Jiang, X. Jiang, and X. Zhu, "Preparation of core–shell and hollow polyurea microspheres via precipitation polymerization using polyamine as crosslinker monomer," *Polym. Chem.*, vol. 4, no. 24, pp. 5776–5784, 2013.

[47] S. J. Wagh, S. S. Dhumal, and A. K. Suresh, "An experimental study of polyurea membrane formation by interfacial polycondensation," *J Memb Sci*, vol. 328, no. 1–2, pp. 246–256, 2009.

Chapter 3 – Structure and Properties of 3D Printed Carbon Nanotube-Polylactic acid Composites

Note: This chapter is published in Polymer Composites as "The Microstructure and Mechanical Properties of 3D Printed Carbon Nanotube-Polylactic acid Composites" [1].

3.1 INTRODUCTION

3D printing is an additive manufacturing technique, wherein three-dimensional objects are created layer-by-layer or drop-by-drop with minimal material waste. 3D printing is capable of creating complex, highly customized and net-shaped structures that are otherwise difficult or impossible to produce using conventional methods such as injection molding [2, 3]. Fused Deposition Modeling (FDM) is one of the most common methods used for 3D printing. It is based on micro-extrusion of thermoplastic polymers in a raster pattern through a nozzle. For better processibility, most FDM methods use thermoplastics, such as polylactic acid (PLA) and acrylonitrile butadiene styrene (ABS), with low glass transition temperatures (< 100°C). FDM parts are great for rapid prototyping purposes but lack the physical properties for practical applications. There are two general approaches to improve the properties of FDM parts, namely, by choosing other polymers with higher temperature stability and better properties (e.g., polyaryletherketone (PAEK) [4] and liquid crystalline polymers [5] and by incorporating fillers in the neat polymers [6, 7]. 3D printing high temperature, high performance polymers involves tackling challenges such as minimizing temperature gradient, and minimizing shrinkage, and increasing inter-road bonding. Also, identifying appropriate polymer grades and developing new formulations for 3D printing constitute an active area of research.

This chapter focuses on exploring carbon nanotubes (CNTs) as short fiber fillers to improve the thermal and mechanical properties of PLA-based FDM parts. PLA is widely utilized in FDM because of its thermal properties and ease of use during printing. PLA biodegrades into lactic acid and further into carbon dioxide and water through hydrolysis making it a useful material for creating biodegradable scaffolds in biomedical applications [8]. PLA has a low glass transition temperature (T_g) of about 55 – 65°C which also coincides with the heat deflection temperature (HDT) of most PLA resins. Improving HDT of PLA requires achieving maximum crystalline content of about 38%,[9] which is neither achievable nor desirable as this would have negative impacts due to shrinkage and warpage in FDM processes. Further improvement in HDT can be achieved with addition of fillers. However, care must be taken while choosing a filler material as they can act as nucleating agents or seed points, significantly increasing the crystallinity of PLA matrix when melt processed, thereby making the system unviable for FDM processes.

3.2 BACKGROUND

CNT is chosen as the reinforcement material because of their excellent intrinsic mechanical, thermal and electrical properties[10-12]. Further, CNT is available in powder form, allowing for direct blending into PLA and extrusion into filaments to be fed to the FDM printer. This process is different from continuous fiber composites printing which requires a specialized printer and carefully chosen polymers (e.g., **MarkForged)** [13,14]. A number of studies exist on including fillers in neat polymers for 3D printing. Tekinalp *et al.* investigated on 3D printed carbon fiber – acrylonitrile-butadiene-styrene (ABS) composites and compared the mechanical properties to those produced against conventional compression molding technique [15]. Samples prepared by

these two methods exhibited comparable tensile strength and modulus attributed to changes in fiber orientation, dispersion and void formation. Carbon fiber loading of as high as 40 wt% was compounded with neat ABS but could not be successfully 3D printed. Extrudate or printed filaments are referred to as "roads", and porosity between the roads is a typical feature of FDM parts. In addition to inter-road porosity, Tekinalp *et al.* observed additional void between the fillers and the polymer matrix in the printed composites at high filler loadings. Nozzle clogging is another major challenge that needs to be overcome while printing with high fiber loading. This challenge can be partially addressed by using a large diameter (>500 μm) nozzle, but the lateral resolution of the print will be compromised as a result. Shofner *et al.* 3D printed vapor grown carbon fiber–ABS composites and increased the average tensile strength and Young's modulus by 39% and 60%, respectively [16]. Compton *et al.* incorporated nano-clay platelets in a thermally curable epoxy and observed high anisotropy upon printing which helps improve the Young's modulus in the load bearing direction [17].

3.3 OBJECTIVE

Compared to more conventional processing methods like injection molding, **s**tructure-processing-properties relations in 3D printing are not well established. Many studies attempted to optimize the mechanical parts by varying process parameters, such as, deposition speed, nozzle temperature, the gap between the print nozzle and build plate, infill pattern, infill density, and part slicing layer thickness [18,19]. This study is limited to exploring the effects of volumetric flow rate and CNT concentration on the structure and subsequent properties of FDM parts. Mechanical properties are benchmarked against existing literature data on PLA-CNT composites and explained in terms of preferential alignment of CNTs induced during 3D printing.

3.4 EXPERIMENTAL METHODS

3.4.1 Materials:

CNTs in this study are multi-walled carbon nanotubes produced using chemical vapor deposition (CVD) technique. CNTs were purchased from Sigma Aldrich (Cat# 659258, Lot# MKBG9911V) and used without any further purification**.** These CNTs have an average diameter of ca. 128 nm (approximately 40 layers thick) and average length on the order of 2.8 μm. Polylactic acid filaments were purchased from 3D maker world (Cat# 4043D).

3.4.2 Molecular weight characterization:

Molecular weights of neat PLA and PLA composites were characterized using gel permeation chromatography (GPC) **(**Waters GPC-1 equipped with 1515 HPLC Pump & Waters 717Plus Autoinjector & Varian Model 380-LC Evaporative Light Scattering Detector) with tetrahydrofuran (THF) from Sigma-Aldrich (Lot# SHBG6390V, ≥99% purity) as the solvent. Approximately 50 mg of sample was dissolved in 20 ml of THF and stored at room temperature for 24 h. To remove CNTs and any impurities, the solutions were then filtered through a 0.45-μm syringe filter before injecting them through the GPC column in order. The bulk density of the neat PLA and CNT-PLA composites was calculated by measuring the weight and volume of the samples.

3.4.3 Optical and Electron Microscopy:

Optical microscopy was carried out using Olympus BX50 installed with a PAXCam CCD camera for capturing images. A single PLA or CNT-PLA pellet was sandwiched between two glass slides and hot pressed at 160 °C for 30 s. The hot-pressed films with glass slides were then cooled and

observed under the microscope. Scanning electron microscopy (SEM; JEOL 6335 Field Emission SEM) was performed after sputtering a thin layer (3 - 5 nm) of gold and palladium onto the fractured tensile test coupons to prevent charging. An accelerating voltage of 10 kV was used for capturing all the images.

3.4.4 X-Ray Diffraction:

For 1D diffraction pattern, CNT-PLA composites were hot pressed into a disc. The peak at 26° with a d-spacing of 3.38 Å corresponds to the interlayer spacing of multi-walled CNT (**Figure 3.10**). For 2D diffraction pattern on FDM samples, only one layer was printed to ensure there is sufficient transmitted X-ray signal. The printed sample was mounted on the holder and care was taken to properly align the sample using the built-in CCD camera, such that the incident beam would either hit the raster center or raster intersection as illustrated in **Figure 3.9a**. Diffraction pattern of the transmitted X-ray was collected onto the detector placed at 65 cm from the sample. The faint ring where 2theta is approximately 26° forms the diffraction pattern of the CNTs aligned along the filament axis. The full width at half maximum (FWHM) of the azimuthal ring integral quantifies the average alignment of CNTs along the road axis and in the load bearing direction. CNT alignment at raster center and raster intersection is then compared to help understand the mechanical properties of 3D printed samples.

3.4.5 Thermogravimetric analysis (TGA):

TA Instruments TGA Q-500 was used for thermogravimetric analysis of the samples after 3D printing. Samples were cut into a small piece weighing about 12 mg for TGA. All the samples were analyzed using air and an arbitrarily chosen temperature ramp rate of 10 °C/min. Thermal

degradation temperature is taken as the maximum of the first derivative of weight loss with respect to temperature.

3.4.6 Differential Scanning Calorimetry:

Thermal transitions of the samples before and after 3D printing were analyzed using TA Instruments DSC Q-100. The sample temperature was equilibrated at 0 °C for 5 minutes before increasing to a final temperature of 220 °C at a ramp rate of 20 °C/min. After reaching 220 °C, the sample was held at this temperature for 5 minutes before ramping down to 0 °C at a ramp rate of 20 °C/min. The cycle was then repeated one more time to collect data for a total of two heating and cooling cycles. % crystallinity of the samples were calculated using the equation

$$\%Crystallinity = \frac{\Delta H_f^{obs}}{\Delta H_f^{\circ}} = \frac{\Delta H_m - \Delta H_c}{\Delta H_f^{\circ}} \quad (1),$$

where $\Delta H_m, \Delta H_c$ and ΔH_f° (93.1 J/g) [20] are enthalpy of melting, enthalpy of crystallization and enthalpy of fusion for 100% crystalline PLA respectively.

3.4.7 3D printer feed filament preparation:

FDM printer in this study uses 1.75 mm (dia.) thermoplastic filaments as the feedstock material. Hydrolysis of PLA accelerates in humid conditions above the glass transition temperature of PLA [21]. To prepare the feed filaments, PLA and CNTs were vacuum dried at room temperature for at least 48 hr to minimize hydrolysis of PLA during processing. Different amounts of CNTs were compounded with PLA using a Haake Minilab Twin Screw Extruder (counter rotating screw, 100 rpm, 160 °C, 5 mins) until the torque reading became constant before extrusion through a circular

die. Spin-draw ratio was varied, for samples with different CNT loadings, to keep the diameter of the extruded filament constant. The extruded samples were fed to a filament chopper, pelletized, and dried at room temperature for 48 hr. These pellets were then extruded again through a 1.75-mm diameter circular die using the twin screw extruder in continuous mode and wound on an in-house built pick-up roll while maintaining a consistent filament diameter of 1.75 mm ± 0.1 mm. The second extrusion was necessary to produce continuous filaments as the compounding mode is limited to extruding 4 g of materials at a time. As the thermal history affects the molecular weight and properties, the control PLA sample was prepared following the same extrusion procedure with no CNTs added.

3.4.8 3D printing mechanical test coupons:

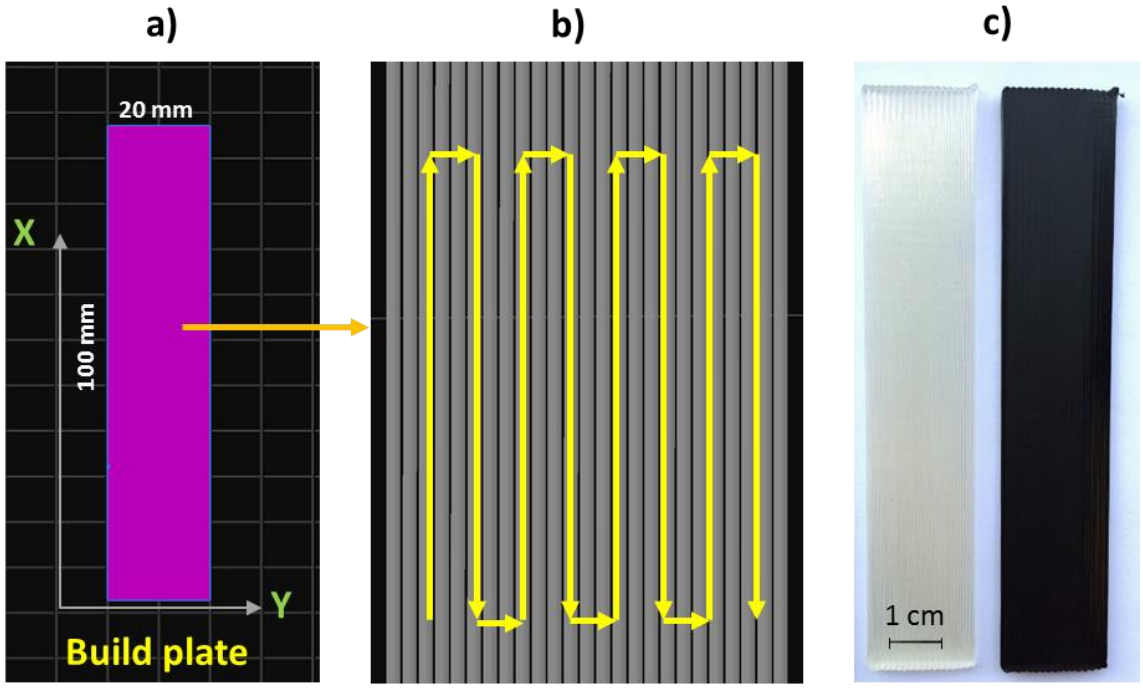

Figure 3.1: (a) Computer-aided design (CAD) rendering of a test coupon, (b) Chosen toolpath for printing a test coupon, where the extruded filaments, or "roads", align along the load bearing

direction in subsequent mechanical testing. (c) Actual 3D printed 0% CNT-PLA (left) and 5% CNT-PLA (right) test coupons.

Hyrel System 30 3D printer was used in this study. The printer has a build volume of 250 mm x 200 mm x 200 mm (X x Y x Z) and a positional accuracy of 50 µm x 50 µm x 20 µm (X x Y x Z). Rectangular test coupons with dimensions of 100 mm x 20 mm x 1.8 mm (L x W x T) were 3D printed with a layer thickness of 300 µm and 6 layers. A nozzle diameter of 500 µm was used and the set temperatures of the nozzle and build plate were 210 °C and 50 °C, respectively. Test coupons, as shown in **Figure 3.1** were printed from a CAD file which was first converted to a **s**tereolithography **(**.stl) file and further into a g-code using Slic3r®. In this study, the toolpath was chosen such that the extruded filaments, or "roads", aligned along the load bearing direction of the test coupons in subsequent mechanical testing (**Figure 3.1b**).

Among many controllable factors, there are some factors that are more difficult to control with Hyrel System 30. Since the printer does not have an enclosed build chamber, part surrounding temperature or envelop temperature is one such factor and is mainly dictated by the room temperature. Another factor is nozzle diameter since it is fixed and cannot be swapped. The standard nozzle diameter is 0.5 mm for Hyrel System 30. Lastly, the part printing location on the build platform was kept constant throughout experimentation. Samples were printed at the center of the build platform.

3.4.9 Mechanical testing:

Mechanical test data were collected using Instron 5869. To protect the coupon from being damaged by the clamps, aluminum plates were glued onto the two ends of the coupon using Loctite E-20HP,

a high strength epoxy (McMaster, Cat# 6430A19). Stress-strain data recorded were used to calculate the Young's modulus and tensile strength of the neat PLA and CNT-PLA composites. A constant displacement rate of 1 mm/min was arbitrarily chosen and a minimum of three samples were measured per experimental condition.

3.4.10 Rheology and sample preparation:

Discs with 25-mm diameter and 1-mm thickness were prepared by compression molding pellets of control and compounded samples at 160 °C for 1 min. The cavity of the mold is connected to an overflow channel for capturing any excess material. The mold was sandwiched between steel plates with Kapton® lining to allow easier sample removal. The mold was cooled down to room temperature before the samples were removed. Rheological experiments were carried out on a strain-controlled rheometer (ARES, TA Instruments) using a 25-mm (dia.) parallel plate fixture. The sample was heated to 210 °C and squeezed to a gap of 1 mm before excess material was trimmed from the edge. Steady state data were collected at 210 °C from a shear rate of 0.1 s^{-1} to 10 s^{-1}. First data point was measured after a delay of 60 s. For a given shear rate, the apparent viscosity value was averaged over a time period of 60 s.

3.5 RESULTS & DISCUSSION

3.5.1 Molecular weight and CNT dispersion

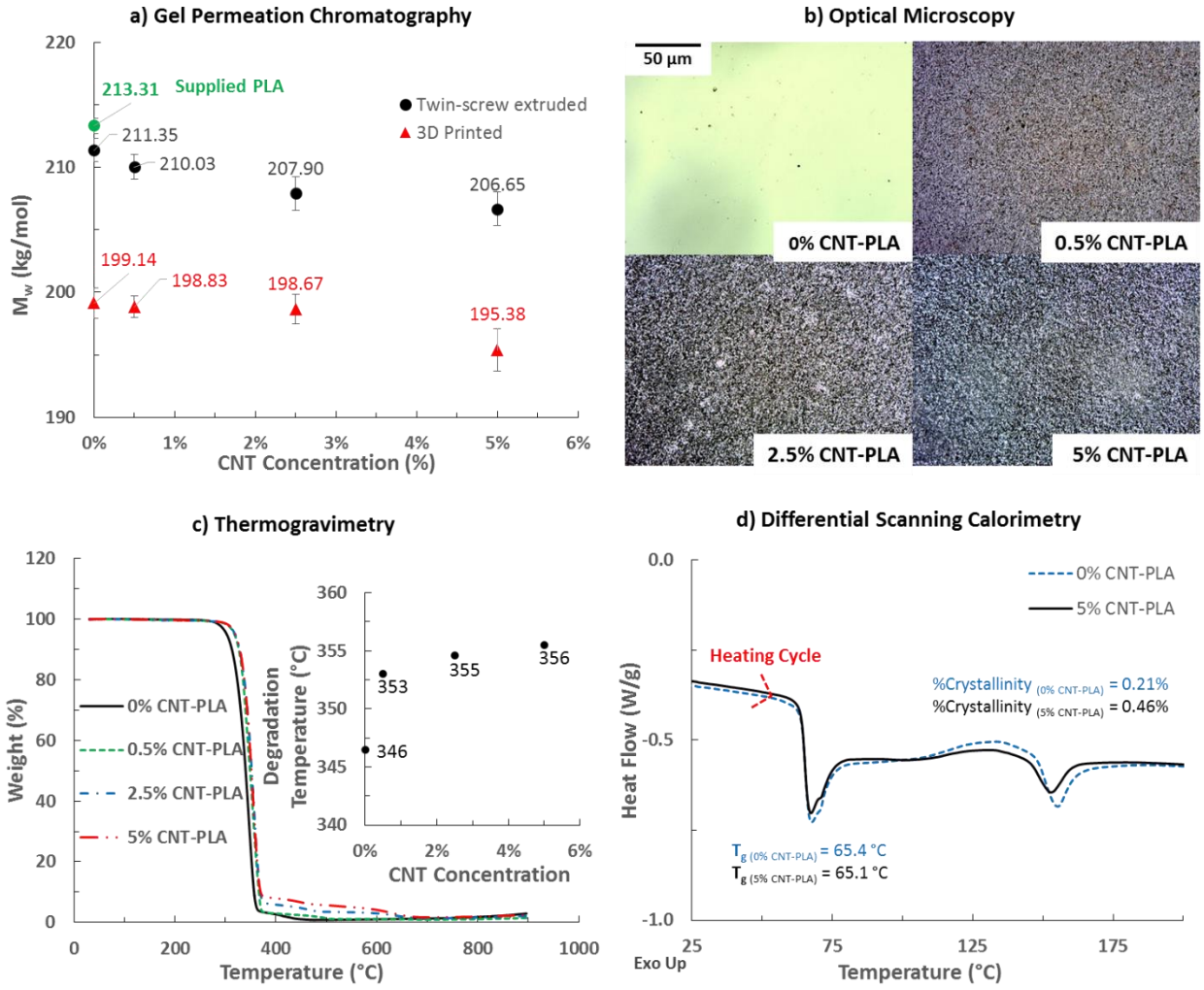

Figure 3.2: (a) Gel permeation chromatography data for twin screw extruded and CNT-PLA composites 3D printed at 210 °C. (b) Optical micrographs of hot pressed composite films showing the difference in optical texture with increasing CNT concentration. Same scale in all micrographs. (c) Thermogravimetric analysis (TGA) data of extruded CNT-PLA composites; inset – degradation temperature for corresponding samples in air. (d) First heating cycle of

differential scanning calorimetry (DSC) data for 0% CNT-PLA and 5% CNT-PLA sample with % crystallinity.

PLA thermally degrades, through oxidation and hydrolysis, during melt processing [8]. Molecular weight and molecular weight distribution have an important impact on the mechanical properties of polymers. In general, the higher the molecular weight, the better the mechanical properties. **Figure 3.2a** shows the weight average molecular weight of as-supplied PLA and PLA after compounding and 3D printing, respectively. Despite the precautions taken to dry PLA and CNT, PLA degradation was still observed. Molecular weight of PLA decreased slightly from 213.31 kg/mol to 211.35 kg/mol in the absence of CNT. The molecular weight distribution characterized as the polydispersity index remains the same at 1.3 before and after compounding PLA. The molecular weight of PLA in samples containing CNTs was lower probably due to the residual moisture present in CNTs, which further contributes to hydrolysis. Further decrease in molecular weight was observed after 3D printing, but the difference between samples with and without CNTs is relatively small (< 2%).

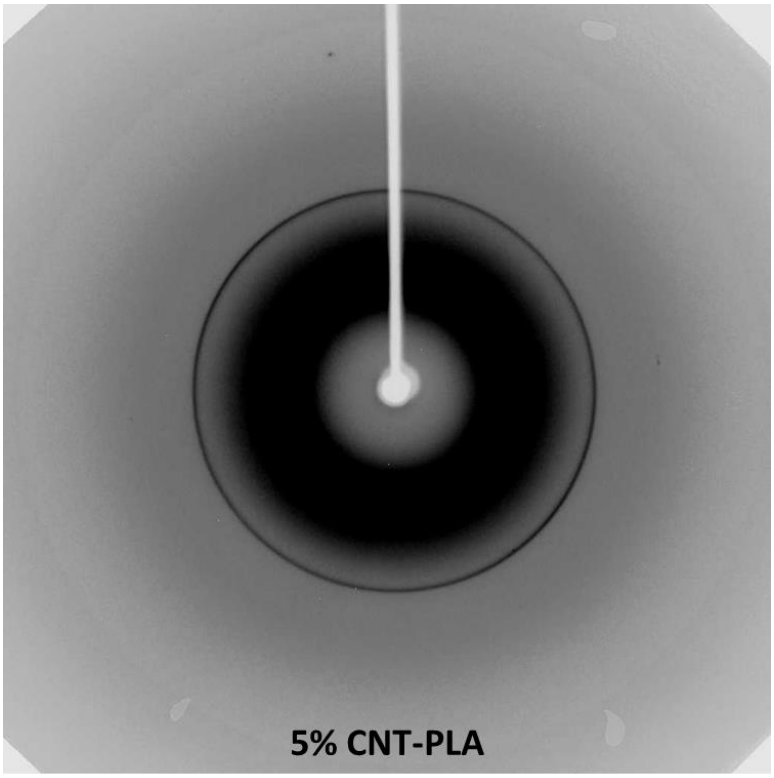

Figure 3.3: XRD diffraction pattern for a hot pressed thin film of 5% CNT-PLA composite indicating no preferential alignment of CNTs. These hot pressed samples were used for optical microscopy.

Figure 3.2b shows optical micrographs of PLA and CNT-PLA composites with different CNT loadings (0.5%, 2.5% and 5%). These samples were prepared by hot pressing a short filament segment into thin films with a thickness of ca. 20 μm. Although optical microscopy cannot resolve individual CNTs, the global optical texture suggested the presence of CNT aggregates that are larger than the optical diffraction limit (~ 1 μm). Further, XRD analysis indicated no preferential alignment of CNTs in these samples (**Figure 3.3**). The overlap between CNT aggregates prevented further aggregate size analysis, but no clogging occurred during the 3D printing, implying these aggregates were smaller than the nozzle diameter (500 μm) under the flow

conditions of 3D printing. However, these CNT aggregates will contribute to local CNT concentration variation and negatively impact the mechanical strength of the printed CNT-PLA composites.

3.5.2 Thermal degradation and thermal transitions

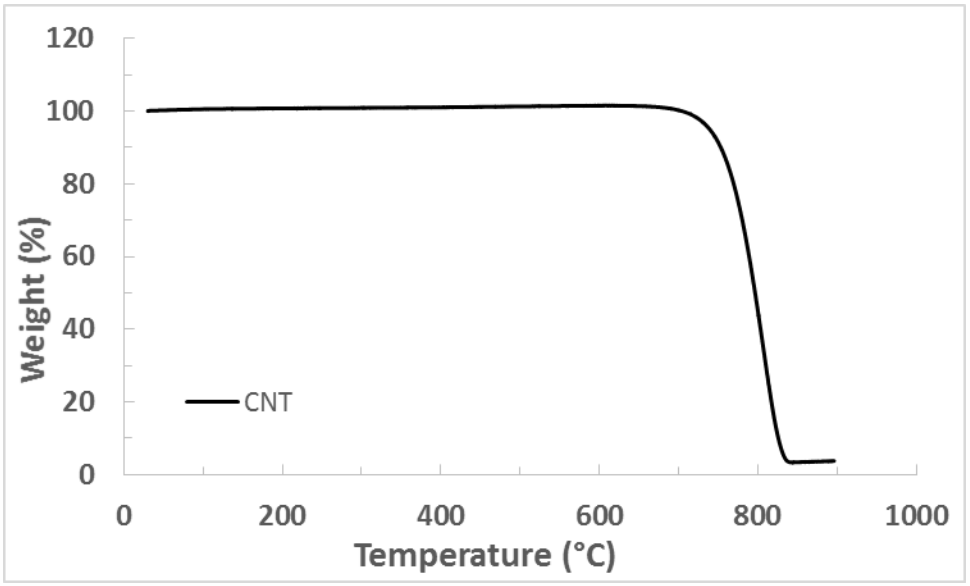

Figure 3.4: TGA weight loss profile for neat CNT in air.

The thermal stability of PLA and CNT-PLA composites was characterized using TGA and the results are shown in **Figure 3.2c.** As a control sample, the "0% CNT-PLA" sample was prepared following the same compounding and extrusion conditions except that no CNT was added. The thermal degradation temperature is reported as the peak in the first derivative of weight loss with respect to temperature. The thermal degradation temperature of neat CNT is 808 °C (**Figure 3.4)**, whereas that of 0% CNT-PLA is 346 °C. The thermal degradation temperature of CNT-PLA composites increased as a function of increasing CNT concentration as shown in **Figure 3.2c**. Similar observations have been previously reported by Wu *et al.* and other research groups [22–25]. CNT has a thermal conductivity close to diamond [26], and the inclusion of CNTs increases

the overall thermal conductivity of the CNT composites, leading to better heat dissipation and consequently an increase in degradation temperature [25].

The thermal transitions of neat PLA and CNT-PLA composites were studied using DSC. **Figure 3.2d** shows the thermal transitions of the 5% CNT-PLA sample with highest CNT loading. No significant difference was observed in the glass transition temperature between neat PLA and CNT-PLA composites, ranging between 65 °C and 66 °C. Full DSC data are included in **Table 3.1**. Further, the degree of crystallinity was calculated using the enthalpy of crystallization and enthalpy of melting (**Equation 1**) and was observed to be < 1.2% in all cases. The inclusion of CNT has negligible effect on the degree of crystallinity of the PLA used in this study. This is probably due to the relatively fast cooling rate involved in 3D printing as the diameter of the printed roads is rather small (<1 mm). Prior studies by Xu *et al.* and Shieh *et al.* suggested that a CNT loading less than 10 wt% did not induce PLA crystallization at a cooling rate of 10 °C/min or higher [27, 28]. The low degree of PLA crystallinity is advantageous for 3D printing because higher crystallinity is associated with higher shrinkage and potential warpage of the printed parts [29].

Table 3.1: Thermal transitions and % crystallinity from Differential Scanning Calorimetry (DSC) data. % Crystallinity was calculated using **Equation 1**. T_g is the glass transition temperature, T_c is the crystallization temperature, and T_m is the melting temperature.

Sample	T_g (°C)	T_c (°C)	T_m (°C)	% Crystallinity
0% CNT-PLA	65.4	133.3	155.2	0.21
0.5% CNT-PLA	66.0	134.7	156.1	1.14
2.5% CNT-PLA	65.5	132.3	153.9	0.17
5% CNT-PLA	65.1	130.7	153.0	0.46

3.5.3 Rheology and Flow Rate Calibration

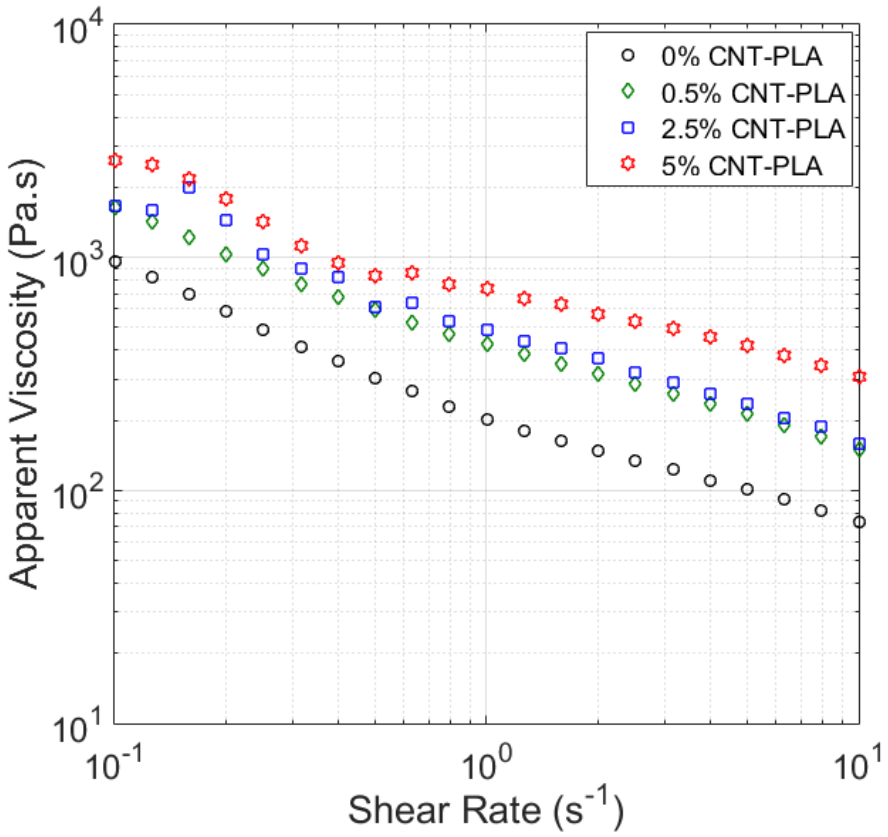

Figure 3.5: Apparent viscosity as a function of shear rate for different weight concentrations of CNT in PLA at 210 °C. A 25-mm parallel plate fixture was used. The reported shear rate corresponds to the maximum shear rate at the edge of the parallel plates.

Figure 3.5 shows the apparent shear viscosity as a function of shear rate for different CNT loadings at 210 °C. Inclusion of CNT in PLA increased the apparent shear viscosity. The degree of viscosity increase depends on CNT orientation and state of aggregation [30]. The CNTs used in this study has an aspect ratio (λ) of 19.5 (length to diameter ratio) and the crossover from dilute to semi-dilute behavior estimated to be at a concentration of 9.4 % (w/w) ($=24r_{CNT}/r_{PLA}l^2$), assuming a

CNT density (ρ_{CNT}) of 1.8 g/cm^3 and PLA density (ρ_{PLA}) of 1.2 g/cm^3 [31]. Despite the relatively high loading, 5% (w/w) CNT in PLA, if individually dispersed, remains within the dilute regime, where there is no CNT-CNT interactions and the viscosity enhancement effect is caused by hydrodynamic interactions [32]. However, this simple analysis does not account for the presence of CNT aggregates.

A power-law fluid model ($\eta_s = K\dot{\gamma}^{n-1}$) was fitted to the steady shear viscosity data of the "0% CNT-PLA" sample, giving K = 230.05 Pa.s$^{0.49}$ and n = 0.49. Shear rate is a function of the radial position within the liquefier. It is zero at the center and highest at the wall. If no slip at the wall is assumed, the wall shear rate for a power law fluid ($\dot{\gamma}_w$) can be calculated using the equation below [33]:

$$\dot{\gamma}_w = \left(3 + \frac{1}{n}\right)\frac{Q}{\pi r^3} \quad (2),$$

where Q is the volumetric flow rate, r is the radius of the liquefier and n is the power law coefficient. The wall shear rate in the liquefier is estimated to be 0.74 s^{-1} for Q = 3.7 mm^3/s, r = 2 mm, and n = 0.49.

During the 3D printing process, the hydrodynamic forces may break up the aggregates and align the CNT along the extrusion direction. Peclet number (*Pe*) compares the hydrodynamic forces versus the thermal motions which lead to randomization of CNT orientation. It is defined as:

$$Pe = \frac{\dot{\gamma}}{D_r} \quad \textbf{(3),}$$

where $\dot{\gamma}$ is the shear rate and D_r is the rotary diffusivity of CNT and is further calculated using the following equation [31]:

$$D_r = \frac{3k_B T\left(\ln\left(l/d\right) - 0.8\right)}{\pi \eta_s l^3} \quad \textbf{(4),}$$

where k_B is the Boltzman constant, T is the temperature, η_s is the viscosity of the suspending medium, and l and d are the length and diameter of the CNTs used, respectively.

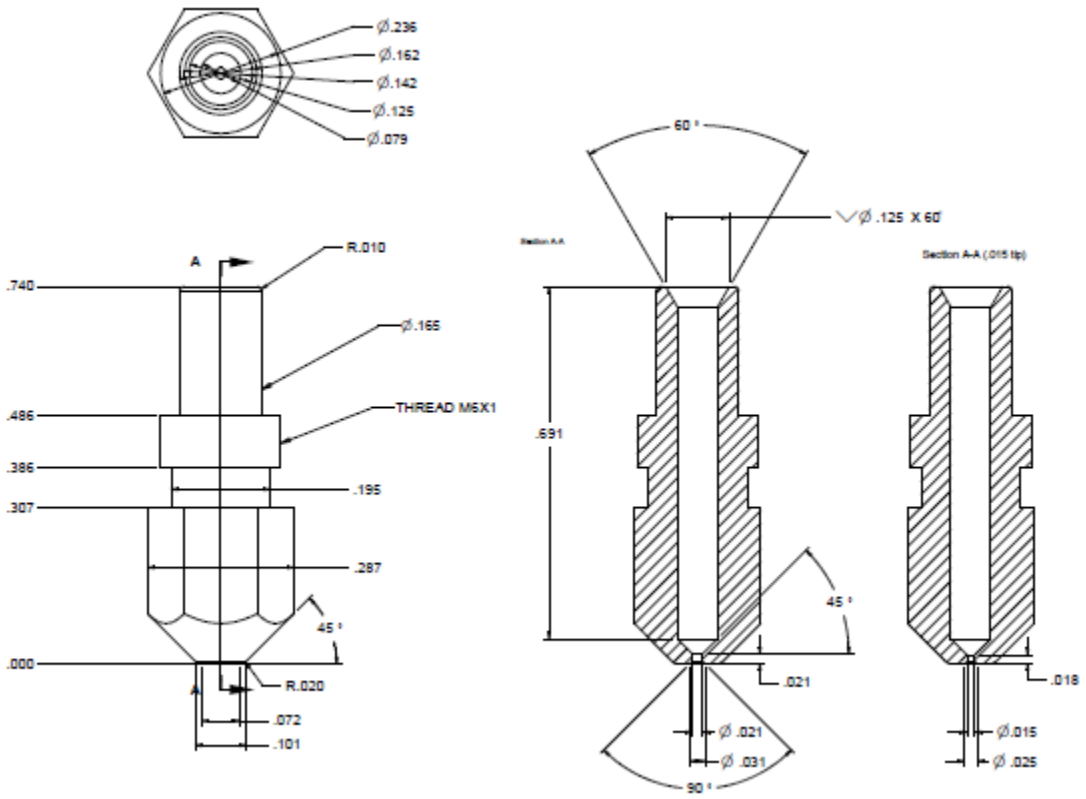

Figure 3.6: Print nozzle geometry installed on Hyrel System 30. Units are in inches.

The viscosity of the suspending medium (η_s) at a shear rate of 0.74 s^{-1} is calculated to be 268 Pa s using the power law model. Based on Equation 4, D_r is calculated to be 3.34 × 10^{-6} s^{-1}, giving a Peclet number on the order of 2.21 × 10^5 at the wall. Pe >> 1 suggests hydrodynamic forces dominate random thermal motions, aligning CNTs in the flow direction. This was later confirmed experimentally in **Section 3.5.5**. However, this relatively simple order-of-magnitude analysis does not account for the aggregates that are initially present, wall slippage, or flow-induced CNT aggregation, which will reduce the degree of CNT alignment. Further, in the actual print nozzle geometry (**Figure 3.6**), the nozzle is tapered. The converging flow further leads to extensional deformation, which aligns the CNTs more effectively than simple shear flows because of the absence of a rotation component [34, 36].

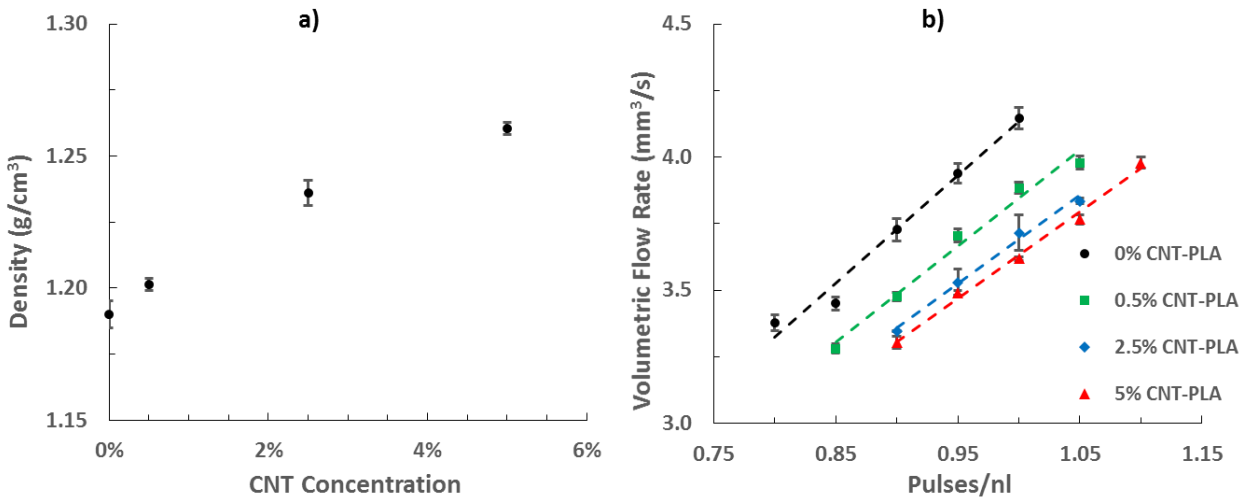

Figure 3.7: (a) Measured density of PLA and CNT-PLA samples based on a minimum of ten samples for each data point. (b) Volumetric flow rate (mm^3/s) as a function of "pulses/nl".

In a FDM printer, the solid feed filament is driven into the liquefier using a pair of pinch rollers. Further, the extrusion flow rate is controlled by a set parameter called "pulses/nl", which is related

to the rotation speed of the pinch rollers. The relation between extrusion flow rate and this parameter is not readily available. As a result, flow rate calibration was carried out. For a given pulses/nl value, the actual mass flow rate was calculated by weighing the printed samples and measuring the time required to print one layer multiplied by the total number of layers printed. Multiplication is performed to exclude the idle time in between printing different layers. The calculated mass flow rate was then divided by the measured density (**figure 3.7a**) to give the volumetric flow rate. For a given pulses/nl value, the volumetric flow rate decreases with increasing CNT loading, as shown in **figure 3.7b**. This trend may be explained by the increase in viscosity due to CNT inclusion. First, inclusion of CNT increases the viscosity, which in turn decreases the volumetric flow rate for a fixed pressure drop and geometry. Second, if the viscosity is too high, the friction may not be able to hold the filament in place, leading to a slip at the roller-filament interface and a reduction in actual filament displacement and volumetric flow rate [37].

3.5.4 Mechanical Properties

Effect of extrusion flow rate

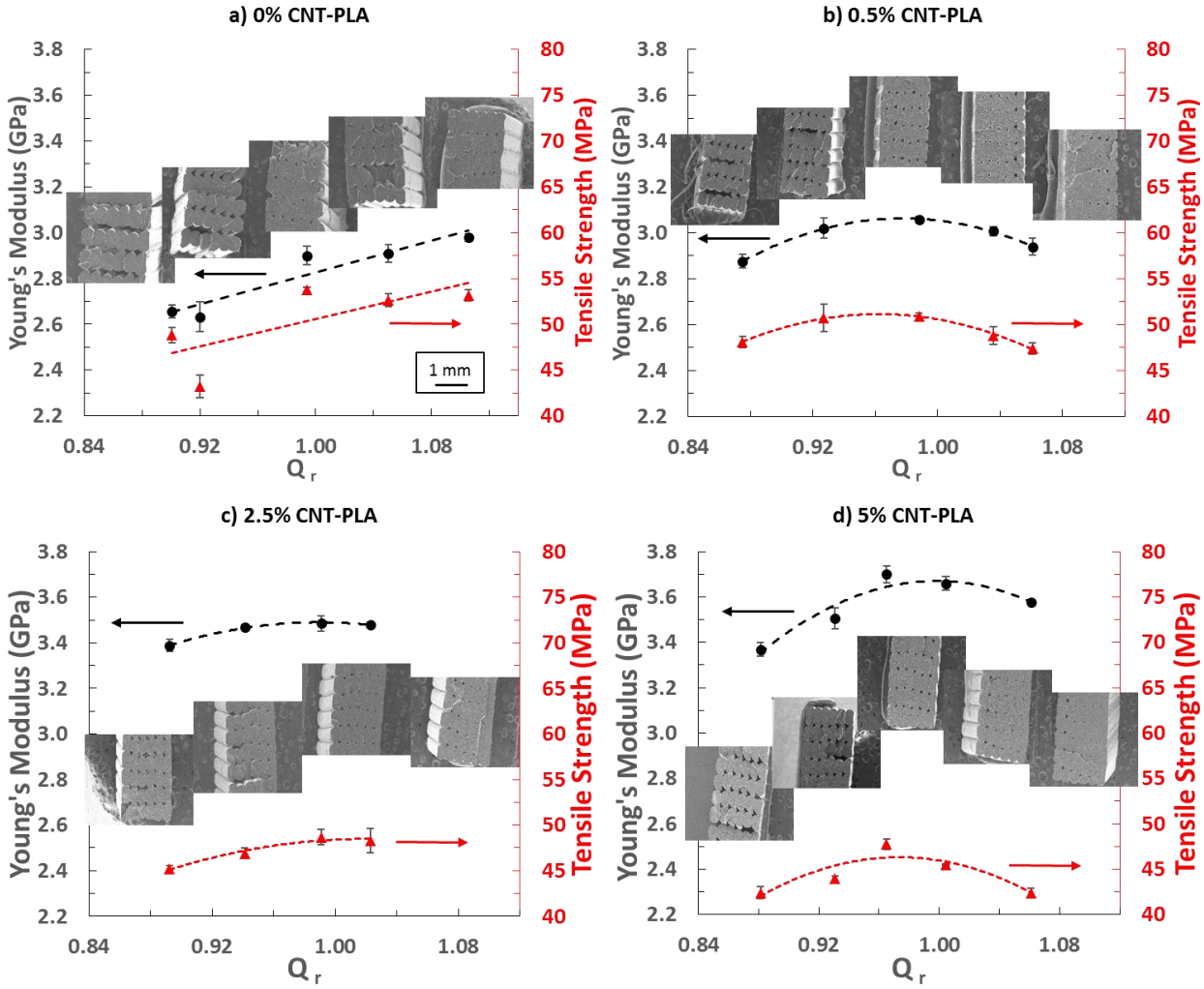

Figure 3.8: Young's modulus, tensile strength, and scanning electron micrographs of the fractured surface as a function of dimensionless volumetric flow rate (Q_r) for (a) 0% CNT-PLA, (b) 0.5% CNT-PLA, and (c) 2.5% CNT-PLA, and (d) 5% CNT-PLA, respectively. Amount of void fraction decreases as a function of increasing Q_r. Same scale as shown in (d) applies to all SEM images.

The width of the extrudate depends on the interplay between extrusion flow rate, translation speed of the print nozzle, and the gap between nozzle and the build plate [19]. For a given gap size and translation speed, a higher volumetric flow rate will lead to wider extrudate. Likewise, a smaller gap or a slower translation speed will also result in extrudate overfilling the gap. In this study, we define a dimensionless volumetric flow rate (Q_r) taking into considerations the nozzle translation speed, and cross-sectional area of the extrudate for a fixed gap and nozzle diameter simultaneously:

$$Q_r = \frac{Q_{actual}}{Q_{ideal}} = \frac{Q_{actual}}{d_{nozzle} h v} \quad \textbf{(5),}$$

where Q_{actual} is the actual volumetric flow rate calculated from calibration curves (**Figure 3.7)**, Q_{ideal} is the ideal volumetric flow rate required to completely fill the gap between the nozzle and the build plate at a given translation speed of the print head, d_{nozzle} is the print nozzle diameter (0.5 mm), h is the gap between the nozzle and the build plate (0.3 mm), and v is the translation speed of the print head (25 mm/s). $Q_r > 1$ indicates "over-flow" and $Q_r < 1$ indicates "under-flow".

Figure 3.8 shows Young's modulus, tensile strength and corresponding electron micrographs of the fractured surface as a function of Q_r for different CNT loadings. In FDM printing, laminate-like mesostructures are formed as printed filaments are partially bonded together via sintering. Like laminates [38], the overall mechanical properties of FDM parts depend on the bonding between different layers (ply), the void density, and the strength of individual extrudate. The latter further depends on matrix material, filler concentration, dispersion, filler orientation, and the stress transfer between the matrix and filler. The bond formation between printed filaments and the resulting bond strength are strongly influenced by these process parameters as well as heat transfer. As a filament is freshly printed, the temperature is initially above the glass transition temperature,

but decreases due to heat loss to the surrounding via conduction, convection, and radiation. As an adjacent filament is laid down, the temperature of previously printed filament increases again and a "neck" is formed between two filaments. The bond quality depends on the amount of residue heat available to enable the molecular diffusion and randomization of polymer chains at the road-road interface. Neck growth slows down almost instantaneously as the filaments rapidly cool down after extrusion. The mesostructures of the printed CNT-PLA strongly depend on dimensionless volumetric flow rate, Q_r. For a fixed extrudate-to-extrudate distance, $Q_r > 1$ leads to a wider neck, whereas $Q_r < 1$ results in a narrower neck or lack of bonding between the roads as illustrated in **Figure 3.12**.

As shown in **Figure 3.8**, in the absence of CNT, the Young's modulus and tensile strength of PLA samples increase as a function of increasing Q_r. This is attributed to the reduction in void fraction and better bonding between individual PLA roads. In the case of CNT-PLA samples, the highest Young's modulus and tensile strength were observed at Q_r close to 1. Like the neat PLA case, increasing the volumetric flow rate for under-filled samples ($Q_r < 1$) reduces the void fraction between roads and increases the stress transfer between individual roads under tension. Theoretically, as the volumetric flow rate is increased, the shear rate within the liquefier should also increase, leading to a higher degree of CNT alignment and consequently higher modulus. However, the opposite trend was observed. We hypothesize that this is related to CNT alignment and overfilling ($Q_r > 1$) randomizes CNT orientation. To examine this hypothesis, XRD analysis was carried out to evaluate the CNT alignment both within and in between the printed roads.

3.5.5 CNT orientation

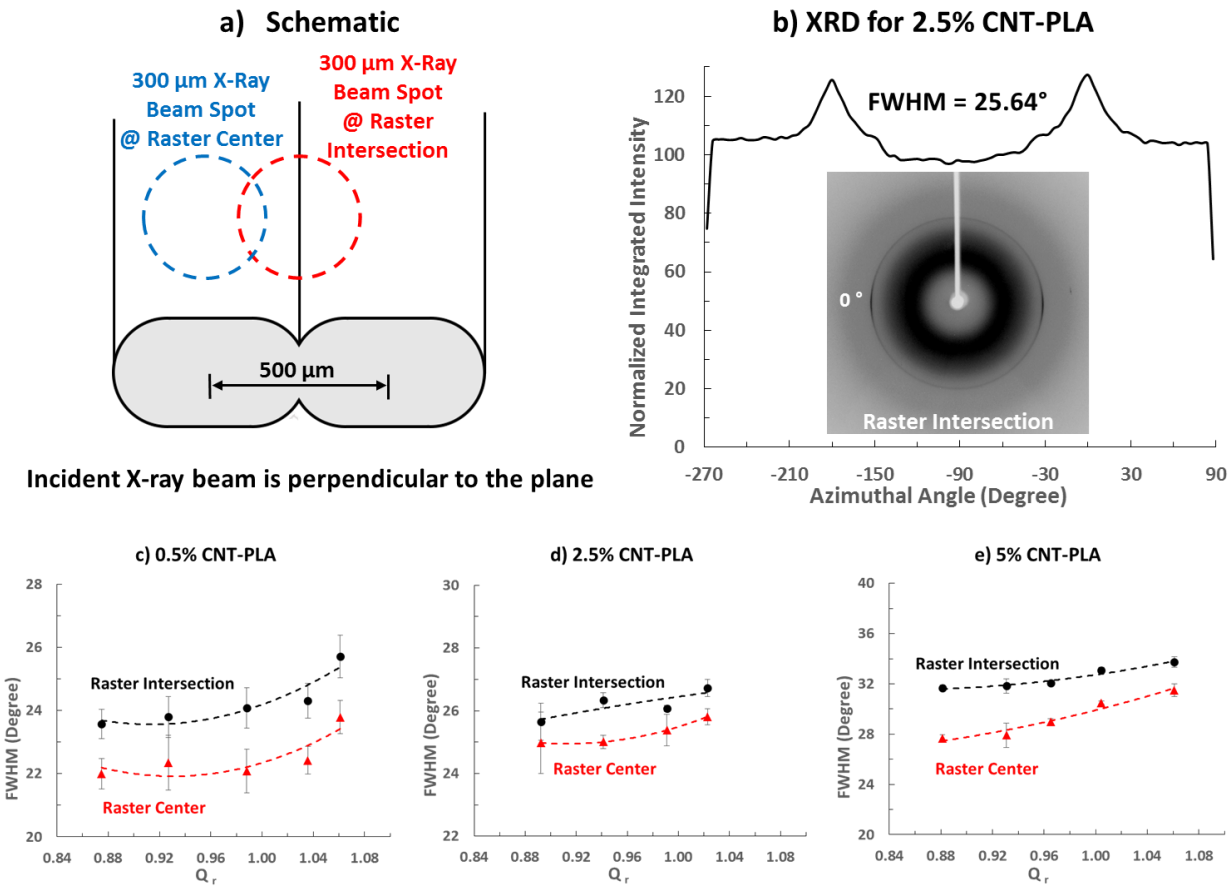

Figure 3.9: (a) Schematic diagram shows the two different locations of X-Ray beam spot for collecting XRD data. (b) XRD pattern for 2.5% CNT-PLA measured at the raster intersection. Full width at half maximum (FWHM) of: (c) 0.5% CNT-PLA, (d) 2.5% CNT-PLA, and (e) 5% CNT-PLA as a function of Q_r. The error bar represents the standard deviation of at least three samples.

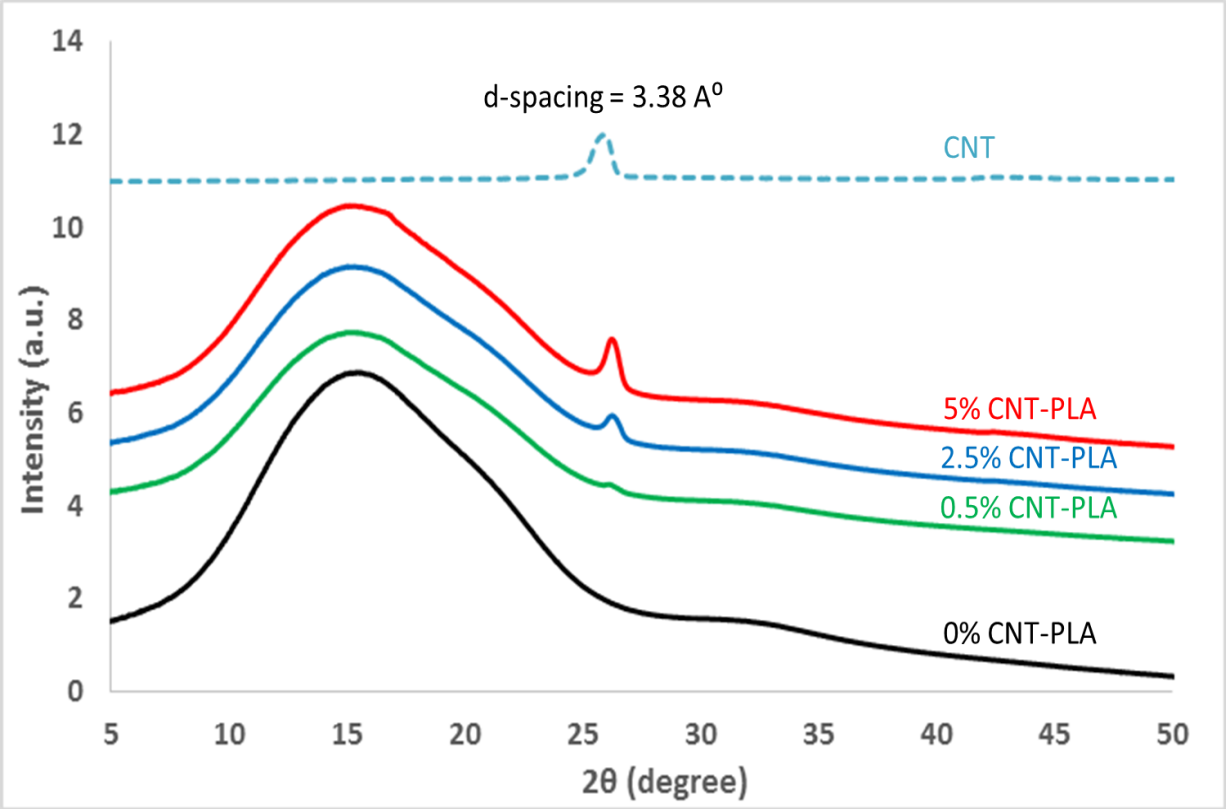

Figure 3.10: 1D X-ray diffraction pattern for PLA and CNT-PLA composites.

XRD was carried out to quantify the degree of CNT alignment both within a printed road and at the intersection between the roads as illustrated in **Figure 3.9(a)**. 1D diffraction pattern (**Figure 3.10**) suggests the 2θ peak at 26° corresponds to a d-spacing of 3.38 Å [39], originating from the interlayer spacing between the walls of multi-walled carbon nanotubes. The faint ring in the 2D diffraction pattern (**Figure 3.9(b)**), where 2θ is approximately 26°, is used to quantify the CNT alignment by calculating the full width at half maximum (FWHM) of the azimuthal ring integral. In the case of 2.5% CNT-PLA, the average FWHM from two peaks at 0° and 180° is 25.64°, indicating that the CNTs are, on average, aligned at 25.64° from the load bearing direction which is the same as the road axis. Similar data were collected from one-layer thick CNT-PLA composites for different CNT loadings and Q_r. A minimum of three samples were measured for

each case, and the average FWHM values are shown in **Figure 3.9**. Scanning electron microscopy (SEM) images for CNT-PLA composites were also collected, confirming the preferential alignment of CNTs along the road axis (**Figure 3.11**). However, the SEM data were not used for quantifying the CNT orientation because the vibratome step during sample preparation may have modified the aggregation state and/or alignment of CNTs [40].

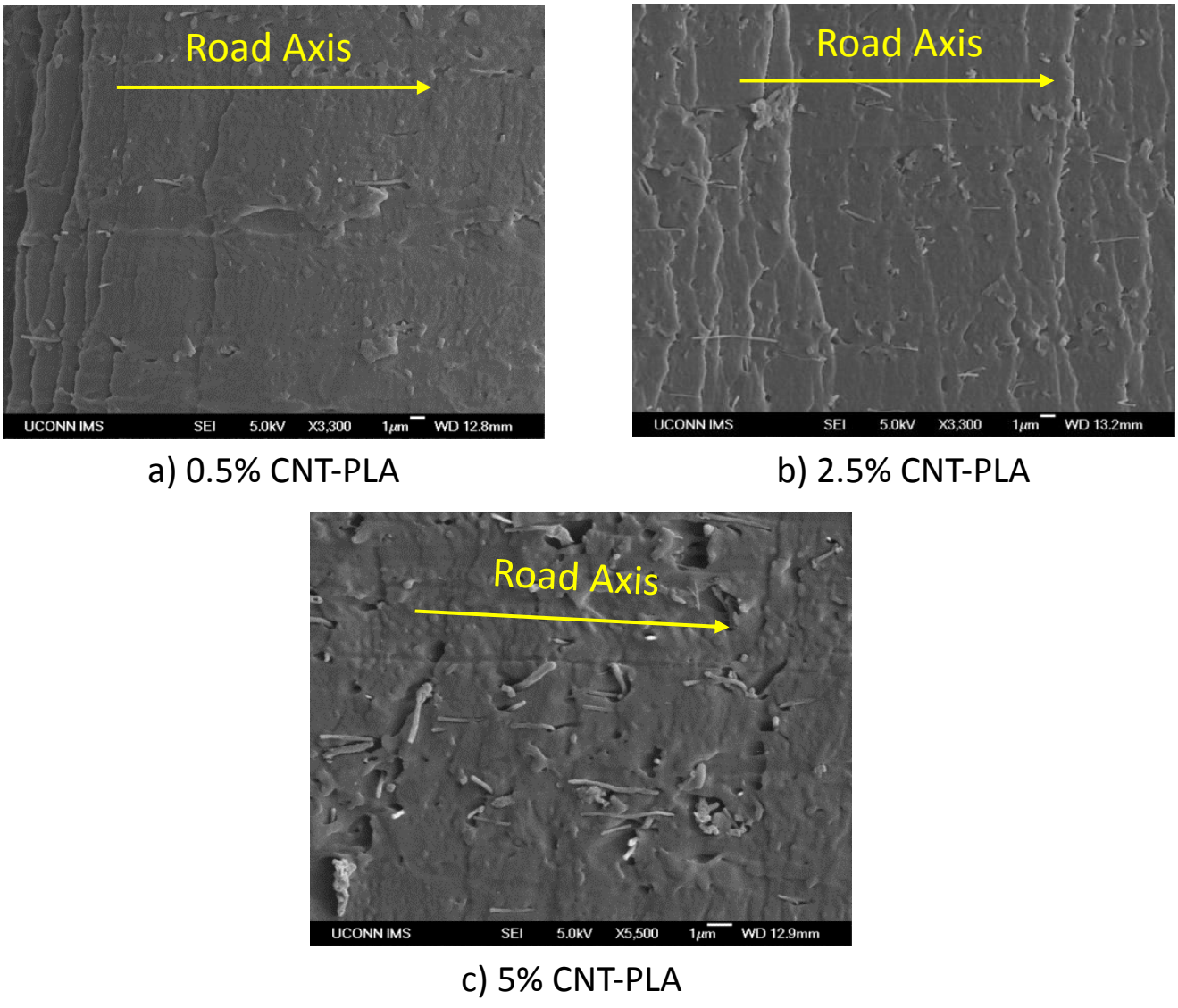

Figure 3.11: SEM images of (a) 0.5% CNT-PLA, (b) 2.5% CNT-PLA and (c) 5% CNT-PLA composites showing preferential CNT alignment along the road axis.

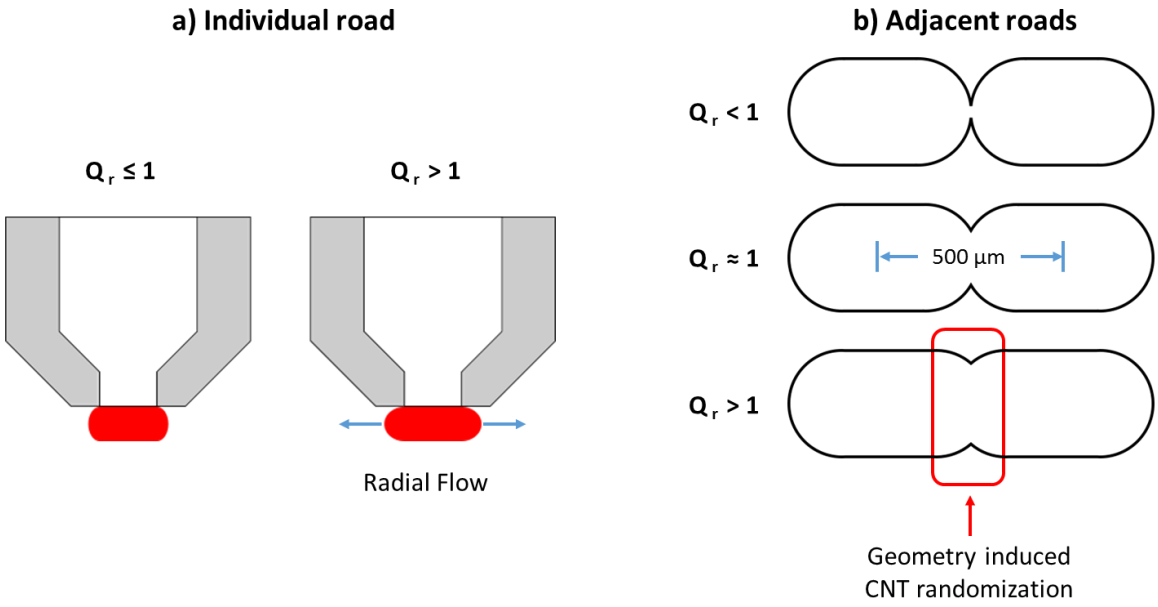

Figure 3.12: Schematic diagrams of hypothesized factors leading to CNT misalignment during 3D printing: (a) radial flow as the material overfills the gap, and (b) geometry-based fusion between adjacent roads.

As shown in **Figure 3.9(c)**, FWHM increases as a function of increasing Q_r for the 0.5% CNT-PLA samples, implying the degree of CNT alignment decreases as a function of increasing Q_r. A similar trend is also observed for the 2.5% and 5% CNT-PLA samples (**Figures 3.9d and 3.9e**). This trend is counter-intuitive because a higher Q_r will lead to a higher wall shear rate and thus higher degree of alignment. However, this experimental observation may be explained by a combination of flow and geometry-induced effects, as illustrated in **Figures 3.12a and 3.12b**. First, if the gap and the relative velocity between the print nozzle and the build plate are fixed, more material flows out of the nozzle with increasing Q_r which results in radial flow in the lateral direction (**Figure 3.12(a)**). This radial flow results in less degree of CNT alignment along the

printing direction. Second, CNT alignment will likely decrease as two adjacent extrudates fuse together (**Figure 3.12(b)**). This geometry-induced misalignment becomes more significant as Q_r increases, especially for $Q_r \geq 1$.

Further, **Figures 3.9c – 3.9e** show that CNTs are less aligned at the intersection compared to that at the center. Although a higher degree of CNT alignment is expected at the intersections due to the higher shear rates close to the wall within the liquefier, this was not observed experimentally. This may be explained by die swelling as well as the combined flow and geometry-induced effects, to which the center of the extrudates is less susceptible. A similar trend has been reported in a FDM simulation study carried out by Heller *et al.* The higher degree of fiber alignment at the core of the extrudate relative to the wall is attributed to a convergence zone of the nozzle — similar to the one used in this experimental study. For a given volumetric flow rate, the flow velocity increases as the cross-sectional area decreases. The increase in flow velocity leads to extensional deformations, which further align the fibers at the core [36].

3.5.6 Effect of CNT concentration and micromechanical models

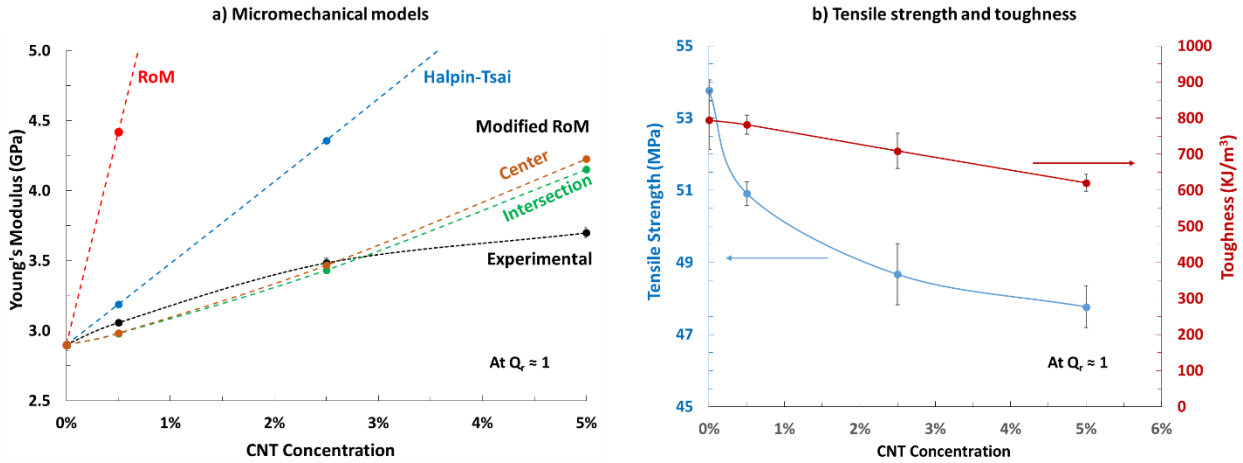

Figure 3.13: (a) Effect of CNT concentration on Young's modulus of FDM parts at $Q_r \approx 1$. Three micro-mechanical models, namely, Rules of Mixtures (RoM), Halpin-Tsai model, and modified RoM, were used. For the modified RoM model fit, the upper and lower bounds were calculated from XRD data measured at the raster center and raster intersection, respectively. The error bars represent standard deviation of at least three measurements. (b) Tensile strength and toughness of CNT-PLA composites at $Q_r \approx 1$. A minimum of three samples were tested for every data point to calculate the standard deviation.

Figure 3.13 shows the Young's modulus of the FDM-printed coupons increases as a function of increasing CNT concentration for $Q_r \approx 1$. Inclusion of CNT with higher modulus is expected to increase the overall modulus. However, the dispersion quality of CNTs and CNT alignment also vary depending on the CNT loading. The higher the CNT loading, the less degree of CNT alignment along the road axis. This may be explained by the higher tendency for CNTs to aggregate at higher concentration [30] . Additionally, CNT aggregates also lead to fluctuations in local CNT concentration, which further results in stress concentration and weaker parts.

Experimental data are further compared against three commonly used micromechanical models, namely rule of mixtures (RoM), Halpin-Tsai, and modified RoM. Experimentally, the modulus does not increase linearly as predicted by the RoM or the Halpin-Tsai model.

First, in the RoM model, the composite modulus is calculated using the following equation:

$$E_c = E_m(1-V_f) + E_f V_f \quad (6),$$

E_c, E_m and E_f are the modulus of the composite, matrix, and filler, respectively, and V_f is the filler volume fraction. The CNT modulus is assumed to be 500 GPa, which is an average value based on a range from 20 GPa to 800 GPa reported for CNTs with a similar diameter [41].

The RoM model assumes: (i) perfect bonding exists between fillers and matrix, (ii) a longitudinal load produces equal strain in fillers and matrix, and (iii) the fillers are continuous and are in parallel. These assumptions are not met for the CNT-PLA system and this may explain the large discrepancy observed.

Second, Halpin-Tsai model for discontinuous fiber composites is considered where the longitudinal modulus ($E_{//}$) of the composite is calculated using the equation below [42].

$$E_{//} = E_m \left[\frac{1 + 2\frac{l}{d}\eta_{//} V_f}{1 - \eta_{//} V_f} \right] \quad (7),$$

where

$$\text{Longitudinal efficiency factor} = \eta_{//} = \left[\frac{\left(\frac{E_f}{E_m}\right) - 1}{\left(\frac{E_f}{E_m}\right) + 2\left(\frac{l}{d}\right)} \right] \quad (8),$$

For continuous fibers, it is assumed that the stress and strain are uniform in the longitudinal direction. However, this assumption is likely to fail in the case of discontinuous fibers. As short stiff fibers are embedded within a more flexible matrix, shear stresses and strains are maximum at

the fiber ends. Short fibers carry load less effectively compared to long fibers and hence have less reinforcement efficiency which the Halpin-Tsai model fails to capture.

Third, a modified RoM, as described by Coleman *et al.*, is used [43]. This model incorporates into the RoM model a length correction factor (η_L) based on the shear lag theory developed by Cox [44] and an orientation correction factor known as the Krenchel orientation correction (η_o). These correction factors accounts for the loss of efficiency when fibers are neither continuous nor unidirectional. Composite modulus using the modified RoM model is given by:

$$E_c = E_m\left(1 - V_f\right) + \eta_L \eta_o E_f V_f \tag{9},$$

where,

$$\eta_L = \left(1 - \frac{\tanh\left(\frac{\beta l}{d}\right)}{\left(\frac{\beta l}{d}\right)}\right) \tag{10},$$

$$\beta = \sqrt{\frac{-3E_m}{2E_f \ln V_f}} \tag{11},$$

and

$$\eta_o = \frac{\sum_n a_{fn} \cos^4 \Phi_n}{\sum_n a_{fn}} \tag{12},$$

β is a measure of stress build up at the fiber ends [44]. Mathematically, the value of the length correction factor (η_L) approaches 1 as the aspect ratio (l/d) increases to infinity. Krenchel orientation factor (η_o) is the fraction of fibers (a_{fn}) aligned at an angle Φ with respect to the load bearing direction (**Equation 13**). This information was extracted from XRD data at the raster center and raster intersection, respectively, and used to calculate the modulus of the composite.

Krenchel orientation factor was calculated from the azimuthal intensity distribution profile according to **Equation 12**. The distribution of intensity (I) with respect to phi (Φ), defined by 2θ = 25.0°–27°, refers to the (002) reflection of CNTs. Since diffracted X-Ray intensity is proportional to the number concentration of oriented CNTs satisfying Bragg's law, the fraction of fibers (a_{fn}) aligned at an angle phi (Φ) is calculated as follows:

$$a_{fn} = \frac{I_n}{\sum_n I_n} \quad (13),$$

a_{fn} value thus obtained is plugged in to **Equation 12** for calculating the Krenchel orientation factor.

All micromechanical models predicts that Young's modulus increases with increasing CNT concentration, as shown in **Figure 3.13(a)**. The modified RoM model, which also considers the CNT orientation, predicts the experimental trend better compared to the RoM and Halpin-Tsai models. The discrepancy between the experimental data and modified RoM predictions at 5% CNT loading is attributed to the poor dispersion and/or poor stress transfer between the CNTs and PLA matrix. Lastly, at low loadings, the initial change in Young's modulus with respect to the change in CNT volume fraction, or dE/dV_f, may be used to compare different experimental results [43,

45]. In this study, an initial slope (dE/dV_f) of 51.6 was calculated. This value is comparable with CNT-PLA composite samples prepared using methods such as compression molding, injection molding, and solid-state drawing, as summarized in **Table 3.2**. However, as shown in **Figure 3.13(b)**, both tensile strength and toughness of the composites decrease with increasing CNT concentration (for $Q_r \approx 1$). The tensile strength and toughness decreased by 11% and 22%, respectively, at 5% CNT loading relative to neat PLA.

Table 3.2: A comparison between dE/dV_f values for composites prepared by different processing methods. The density of CNTs was assumed to be 1.8 g/cm^3 for all calculations.

Processing method	**dE/dV_f**	**Remarks**	**Reference**
3D printing	51.6	Melt compounded	This study
Solid-state drawing	30.0	Drawn (draw ratio = 1)	Mai *et al.* [46]
Injection molding	1.1 – 2.6	Melt compounded	Desa *et al.* [47,48]
Compression molding	83.3 – 158.3	Solution mixed (functionalized CNTs)	Kim *et al.*[49]

3.6 CONCLUSIONS

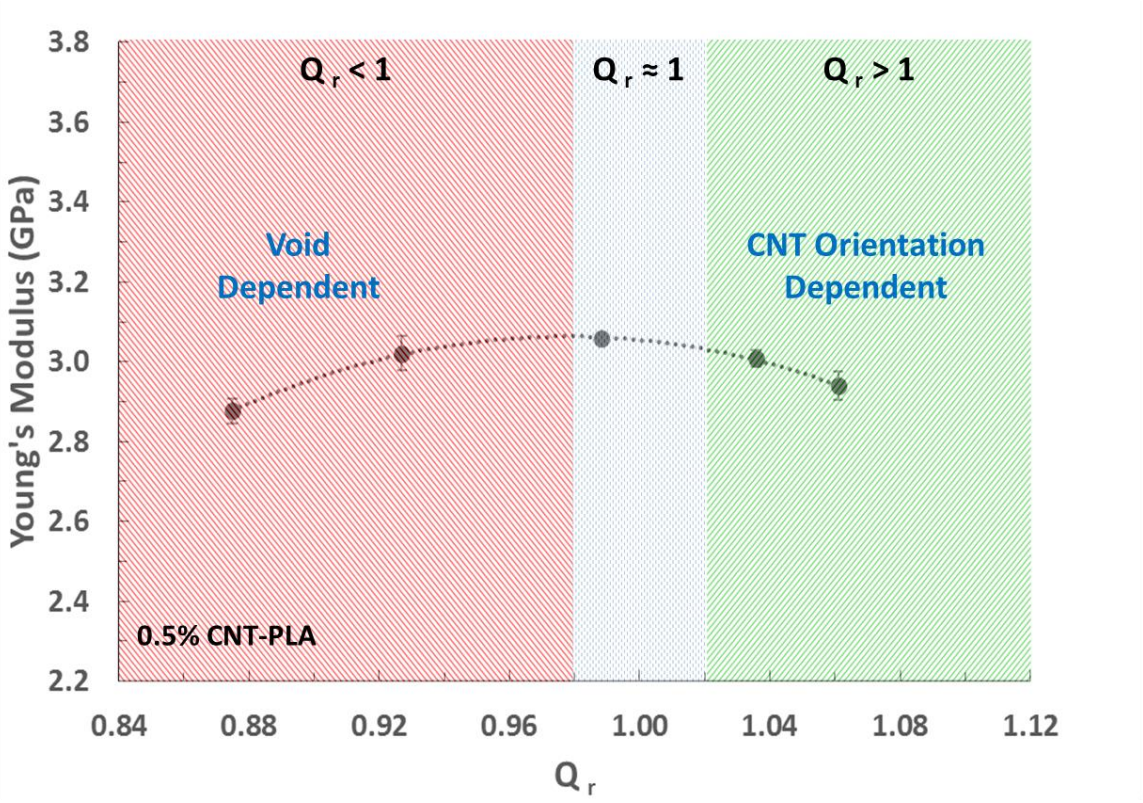

Figure 3.14: Effect of printing flow rate on the Young's modulus of 3D printed CNT-PLA composites using 0.5% CNT-PLA as an example. For $Q_r < 1$, increasing Q_r reduces void fraction and increases modulus, whereas for $Q_r > 1$, increasing Q_r leads to flow- and geometry-induced CNT misalignment as illustrated in **Figure 3.12**.

In summary, this study explored the 3D printing of CNT-PLA composites using an extrusion-based fused deposition modeling (FDM) method. Feedstock filaments for the FDM 3D printer were prepared by compounding PLA at different CNT loadings, namely, 0.5%, 2.5%, and 5% by weight. The weight average molecular weight, thermal degradation temperature, and thermal transitions of the 3D printing feedstock materials were characterized before and after compounding

and also after 3D printing. The effects of volumetric flow rate and CNT concentration on the microstructure and subsequent mechanical properties of 3D printed test coupons were investigated. The actual printing flow rate during 3D printer was calibrated. A dimensionless volumetric flow rate, Q_r, was further defined. Q_r is essentially a "gap-filling" index and is based on the printing flow rate as well as the gap size and the relative velocity between the print nozzle and the build plate. $Q_r < 1$ indicates under-flow, whereas $Q_r > 1$ indicates over-flow. Q_r was found to be a critical parameter in understanding the microstructure and subsequent mechanical properties of FDM parts (as shown in **Figure 3.14**). For $Q_r < 1$, increasing Q_r reduced the void fraction in FDM parts and thus increased the Young's modulus. However, in the case of CNT-PLA composites, the Young's modulus decreased as a function of increasing Q_r, for $Q_r > 1$. XRD data further revealed the higher the Q_r, the lower degree of CNT alignment along the road axis, which is the same as the load bearing direction in mechanical testing. We hypothesized that this is caused by radial flows and fusion between adjacent roads. Additionally, the difference between CNT alignment at the intersections between printed roads and within individual roads suggested the importance of a convergence zone within the printer chamber, consistent with a recent FDM simulation study [36]. Lastly, inclusion of 5% of CNTs (by weight) increased the Young's modulus of the FDM parts by 30%, but the tensile strength and toughness decreased by 11% and 22%, respectively. The effects of CNT concentration and orientation on Young's modulus were studied and compared against three micromechanical models.

3.7 REFERENCES

[1] H. S. Patanwala, D. Hong, S. R. Vora, B. Bognet, and A. W. K. Ma, "The microstructure and mechanical properties of 3D printed carbon nanotube-polylactic acid composites," *Polym Compos*, Jul. 2017.

[2] W. Wu, A. DeConinck, and J. A. Lewis, "Omnidirectional printing of 3D microvascular networks.," *Adv Mater*, vol. 23, no. 24, pp. H178-83, Jun. 2011.

[3] S.-Z. Guo, X. Yang, M. C. Heuzey, and D. Therriault, "3D printing of a multifunctional nanocomposite helical liquid sensor.," *Nanoscale*, vol. 7, no. 15, pp. 6451–6, 2015.

[4] M. Hajihosseini, J. Faradmal, and A. Sadighi-Pashaki, "System and method for 3D printing on permeable materials," USPTO 20160185041, 2015.

[5] J. H. Gray, Robert W, IV; Baird, Donald G Author; Bohn, "Effects of processing conditions on short TLCP fiber reinforced FDM parts," *Rapid Prototyp J*, vol. 4.1, pp. 14–25, 1998.

[6] J. M. Gardner, G. Sauti, J. W. Kim, R. J. Cano, R. A. Wincheski, C. J. Stelter, B. W. Grimsley, D. C. Working, and E. J. Siochi, "3-D printing of multifunctional carbon nanotube yarn reinforced components," *Addit Manuf*, vol. 12, pp. 38–44, 2016.

[7] S. Dul, L. Fambri, and A. Pegoretti, "Fused deposition modelling with ABS-graphene nanocomposites," *Compos Part A Appl Sci Manuf*, vol. 85, pp. 181–191, 2016.

[8] T. Maharana, B. Mohanty, and Y. S. Negi, "Melt-solid polycondensation of lactic acid and its biodegradability," *Prog Polym Sci*, vol. 34, no. 1, pp. 99–124, 2009.

[9] T. Tábi, I. E. Sajó, F. Szabó, A. S. Luyt, and J. G. Kovács, "Crystalline structure of annealed polylactic acid and its relation to processing," *Express Polym Lett*, vol. 4, no. 10, pp. 659–668, 2010.

[10] H. J. Qi, K. B. K. Teo, K. K. S. Lau, M. C. Boyce, W. I. Milne, J. Robertson, and K. K.

Gleason, “Determination of mechanical properties of carbon nanotubes and vertically aligned carbon nanotube forests using nanoindentation,” *J Mech Phys Solids*, vol. 51, no. 11–12, pp. 2213–2237, Nov. 2003.

[11] P. Kim, L. Shi, A. Majumdar, and P. McEuen, “Thermal Transport Measurements of Individual Multiwalled Nanotubes,” *Phys Rev Lett*, vol. 87, no. 21, pp. 215502-1-215502–4, Oct. 2001.

[12] E. Bekyarova, M. E. Itkis, N. Cabrera, B. Zhao, A. Yu, J. Gao, and R. C. Haddon, “Electronic properties of single-walled carbon nanotube networks.,” *J Am Chem Soc*, vol. 127, no. 16, pp. 5990–5, Apr. 2005.

[13] R. Matsuzaki, M. Ueda, M. Namiki, T.-K. Jeong, H. Asahara, K. Horiguchi, T. Nakamura, A. Todoroki, and Y. Hirano, “Three-dimensional printing of continuous-fiber composites by in-nozzle impregnation.,” *Sci Rep*, vol. 6, no. February, p. 23058, 2016.

[14] N. Li, Y. Li, and S. Liu, “Rapid Prototyping of Continuous Carbon Fiber Reinforced Polylactic Acid Composites by 3D Printing,” *J Mater Process Technol*, vol. 238, pp. 218–225, 2016.

[15] H. L. Tekinalp, V. Kunc, G. M. Velez-Garcia, C. E. Duty, L. J. Love, A. K. Naskar, C. A. Blue, and S. Ozcan, “Highly oriented carbon fiber-polymer composites via additive manufacturing,” *Compos Sci Technol*, vol. 105, pp. 144–150, 2014.

[16] M. L. Shofner, K. Lozano, F. J. Rodríguez-Macías, and E. V. Barrera, “Nanofiber-reinforced polymers prepared by fused deposition modeling,” *J Appl Polym Sci*, vol. 89, no. 11, pp. 3081–3090, 2003.

[17] B. G. Compton and J. a. Lewis, “3D-printing of lightweight cellular composites,” *Adv Mater*, pp. 5930–5935, 2014.

[18] O. Rishi, “Feed Rate Effects In Freeform Filament Extrusion,” 2013.

[19] O. S. Carneiro, A. F. Silva, and R. Gomes, “Fused deposition modeling with polypropylene,” *Mater Des*, vol. 83, pp. 768–776, 2015.

[20] C. S. Lovell, J. M. Fitz-Gerald, and C. Park, “Decoupling the effects of crystallinity and orientation on the shear piezoelectricity of polylactic acid,” *J Polym Sci Part B Polym Phys*, vol. 49, no. 21, pp. 1555–1562, Nov. 2011.

[21] T. Villmow, P. Pötschke, S. Pegel, L. Häussler, and B. Kretzschmar, “Influence of twin-screw extrusion conditions on the dispersion of multi-walled carbon nanotubes in a poly(lactic acid) matrix,” *Polymer (Guildf)*, vol. 49, no. 16, pp. 3500–3509, 2008.

[22] B. B. Marosfoi, A. Szabó, G. Marosi, D. Tabuani, G. Camino, and S. Pagliari, “Thermal and spectroscopic characterization of polypropylene-carbon nanotube composites,” *J Therm Anal Calorim*, vol. 86, no. 3, pp. 669–673, 2006.

[23] G. Gorrasi, M. Sarno, A. Di Bartolomeo, D. Sannino, P. Ciambelli, and V. Vittoria, “Incorporation of Carbon Nanotubes into Polyethylene by High Energy Ball Milling: Morphology and Physical Properties,” *J Polym Sci Part B Polym Phys*, vol. 45, no. April, pp. 597–606, 2007.

[24] H.-S. Kim, B. Hyun Park, J.-S. Yoon, and H.-J. Jin, “Thermal and electrical properties of poly(l-lactide)-graft-multiwalled carbon nanotube composites,” *Eur Polym J*, vol. 43, no. 5, pp. 1729–1735, 2007.

[25] D. Wu, L. Wu, M. Zhang, and Y. Zhao, “Viscoelasticity and thermal stability of polylactide composites with various functionalized carbon nanotubes,” *Polym Degrad Stab*, vol. 93, no. 8, pp. 1577–1584, 2008.

[26] A. E. Aliev, M. H. Lima, E. M. Silverman, and R. H. Baughman, “Thermal conductivity

of multi-walled carbon nanotube sheets: radiation losses and quenching of phonon modes.," *Nanotechnology*, vol. 21, no. 3, p. 35709, Jan. 2010.

[27] H.-S. Xu, X. J. Dai, P. R. Lamb, and Z.-M. Li, "Poly(l-lactide) crystallization induced by multiwall carbon nanotubes at very low loading," *J Polym Sci Part B Polym Phys*, vol. 47, no. April, pp. 2341–2352, 2009.

[28] Y. T. Shieh and G. L. Liu, "Effect of MolecularWeight and Temperature on Physical Aging of ThinGlassy Poly(2,6-dimethyl-1,4-phenylene oxide) Films," *J Polym Sci Part B Polym Phys*, vol. 45, pp. 1870–1881, 2007.

[29] S. H. Kochesfahani, "Improving PLA-based Material for FDM 3D-Printers Using Minerals (Principles and Method Development)," in *SPE ANTEC*, 2016, pp. 1958–1614.

[30] A. W. K. Ma, F. Chinesta, A. Ammar, and M. R. Mackley, "Rheological modeling of carbon nanotube aggregate suspensions," *J Rheol (N Y N Y)*, vol. 52, no. 2008, p. 1311, 2008.

[31] R. G. Larson, *The Structure and Rheology of Complex Fluids*. OUP USA, 1999.

[32] J. Mewis and N. J. Wagner, *Colloidal Suspension Rheology*. Cambridge University Press, 2012.

[33] C. W. Macosko, *Rheology : principles, measurements, and applications*. VCH, 1994.

[34] A. W. K. Ma, F. Chinesta, T. Tuladhar, and M. R. Mackley, "Filament stretching of carbon nanotube suspensions," *Rheol Acta*, vol. 47, no. 4, pp. 447–457, May 2008.

[35] G. B. Jeffery, "The Motion of Ellipsoidal Particles Immersed in a Viscous Fluid," *Proc R Soc London A Math Phys Eng Sci*, vol. 102, no. 715, 1922.

[36] B. P. Heller, D. E. Smith, and D. A. Jack, "Effects of extrudate swell and nozzle geometry on fiber orientation in Fused Filament Fabrication nozzle flow," *Addit Manuf*, vol. 12, pp.

252–264, 2015.

[37] D. Espalin, J. Alberto Ramirez, F. Medina, W. M. Johnson, M. Rowell, B. Deason, M. Eubanks, B. N. Turner, R. Strong, and S. A. Gold, "Rapid Prototyping Journal A review of melt extrusion additive manufacturing processes: I. Process design and modeling," *Rapid Prototyp J Rapid Prototyp J Rapid Prototyp J Iss Rapid Prototyp J*, vol. 20, no. 3, pp. 192–204, 2014.

[38] P. K. Mallick, *Fiber-reinforced composites : materials, manufacturing, and design*. CRC Press, 2008.

[39] A. Cao, C. Xu, J. Liang, D. Wu, and B. Wei, "X-ray diffraction characterization on the alignment degree of carbon nanotubes," *Chem Phys Lett*, vol. 344, pp. 13–17, 2001.

[40] P. M. Ajayan, O. Stephan, C. Colliex, and D. Trauth, "Aligned Carbon Nanotube Arrays Formed by Cutting a Polymer Resin-Nanotube Composite," *Science (80-)*, vol. 265, no. 5176, pp. 1212–1214, 1994.

[41] D. Qian, E. C. Dickey, R. Andrews, and T. Rantell, "Load transfer and deformation mechanisms in carbon nanotube-polystyrene composites," *Appl Phys Lett*, vol. 76, no. 20, p. 2868, 2000.

[42] D. F. O'Regan, M. Akay, and B. Meenan, "A comparison of Young's modulus predictions in fibre-reinforced-polyamide injection mouldings," *Compos Sci Technol*, vol. 59, no. 3, pp. 419–427, 1999.

[43] J. N. Coleman, U. Khan, W. J. Blau, and Y. K. Gun'ko, "Small but strong: A review of the mechanical properties of carbon nanotube-polymer composites," *Carbon N Y*, vol. 44, no. 9, pp. 1624–1652, 2006.

[44] H. L. Cox, "The elasticity and strength of paper and other fibrous materials," *Br J Appl*

Phys, vol. 3, no. 3, pp. 72–79, 2002.

[45] J. N. Coleman, U. Khan, and Y. K. Gun'ko, "Mechanical reinforcement of polymers using carbon nanotubes," *Adv Mater*, vol. 18, no. 6, pp. 689–706, 2006.

[46] F. Mai, H. Deng, W. Tu, S. Chankajorn, Q. Fu, E. Bilotti, and T. Peijs, "Oriented Poly(lactic acid)/Carbon Nanotube Composite Tapes with High Electrical Conductivity and Mechanical Properties," *Macromol Mater Eng*, vol. 300, no. 12, pp. 1257–1267, 2015.

[47] M. S. Z. Mat Desa, A. Hassan, A. Arsad, R. Arjmandi, and N. N. B. Mohammad, "Influence of rubber content on mechanical, thermal, and morphological behavior of natural rubber toughened poly(lactic acid)-multiwalled carbon nanotube nanocomposites," *J Appl Polym Sci*, vol. 133, no. 48, pp. 1–9, 2016.

[48] M. S. Z. M. Desa, A. Hassan, A. Arsad, and N. N. B. Mohammad, "Mechanical properties of poly(lactic acid)/multiwalled carbon nanotubes nanocomposites," *Mater Res Innov*, vol. 18, no. October, pp. 14–17, 2014.

[49] H.-S. Kim, Y. S. Chae, B. H. Park, J.-S. Yoon, M. Kang, and H.-J. Jin, "Thermal and electrical conductivity of poly(l-lactide)/multiwalled carbon nanotube nanocomposites," *Curr Appl Phys*, vol. 8, no. 6, pp. 803–806, 2008.

Chapter 4 – 3D Printing Matrigel: A Feasibility study

4.1 INTRODUCTION

Cancer is caused by the cells in the body that change and divide without control forming a lump or mass called tumor [1]. A vast majority of breast cancer initiates in glands for milk production called lobules and ducts that connect the lobules to the nipple. Typically breast cancer can be detected during a screening examination before the symptoms have developed or after noticing a lump.

According to the American Cancer Society, in 2015, approximately 290,000 women were diagnosed with breast cancer out of which 40,000 died due to complications arising from the disease [1]. Most breast cancers are invasive or infiltrating and can break through the walls of the glands or ducts where they originate and grow into the surrounding breast tissue. Understanding the interaction of breast cancer cells with the microenvironment may lead to better strategies to block this interaction and treat the disease.

4.2 OBJECTIVES

Over the last decade, a central focus of drug discovery and disease modeling efforts has been the incorporation of *in-vitro* testing models that better mimic *in-vivo* conditions found within the target patient. Research indicates that traditional 2D cell culture methods does not accurately mimic the anatomy or physiology of a 3D *in-vivo* environment in which cancer cells reside [2]. As a result, the unnatural 2D environment may provide inaccurate data regarding the predicted response of cancer cells to chemotherapeutics making it arguably primitive [3]. Therefore, studying three

dimensional cell cultures is clearly more relevant but requires multidisciplinary approach and expertise.

The overarching aim of this project is to lay the foundation for precise and reproducible 3D bioprinting which can in future be combined with predictive mathematical modeling to understand the role of the local environment in the growth of breast tumors. 3D printing is one of the fastest growing technologies capable of creating three-dimensional objects from computer-aided designs. In this research, 3D printing of cells and an extracellular matrix material have been explored, where multiple nozzles were used to deliver stromal and cancer cells at predetermined locations to create 3D cell cultures.

Rheology was used to optimize the print parameters for the print material, Matrigel® - a gelatinous protein mixture secreted by Engelbreth-Holm-Swarm (EHS) mouse sarcoma. Matrigel® contains extracellular matrix proteins, such as laminin and collagen, growth factors, and enzymes. It closely resembles the complex microenvironment found in many tissues and is often used by cell biologists as a basement membrane matrix for culturing cells [4, 5].

4.3 SIGNIFICANCE & IMPACT

It is well established that cancer is a disease that involves disregulation of dynamic networks, such as intracellular signaling cascades, and needs to be understood across several spatial and temporal scales. This can be studied effectively by constructing a predictive and robust mathematical model which requires experimental data to validate. Experimental data obtained from this project can be coupled with mathematical modeling to quantify the contribution of the local environment to tumor

growth. In long-term this will facilitate the development of new therapies to more effectively inhibit breast cancer growth and metastasis.

4.4 BACKGROUND & APPROACH

Since 2-dimensional cell cultures lack the intercellular effects of a 3-dimensional collection of cells, the use of 3D cell cultures has emerged in recent years as a model system of choice. A wide variety of techniques are currently available to culture cells into 3D structures and can be mainly divided into two categories; (a) non-scaffold-based and (b) scaffold-based techniques.

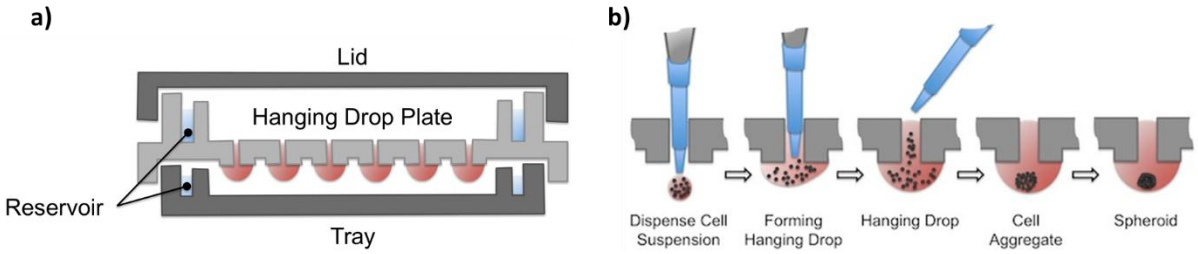

Figure 4.1: (a) Schematic of a hanging drop plate and (**b)** a typical procedure to obtain a spheroid using hanging drop plate. Source: www.cellsystemsbiology.com.

The major non-scaffold based method is the hanging drop microplating (HDP) technique, as shown in **Figure 4.1**, where in the absence of a support structure, cells self-assemble into 3D spheroid structures. Unlike regular plates with a traditional base, HDP's base have an aperture carefully designed to form a discrete droplet of the media sufficient for cellular aggregation but also small enough that surface tension prevents the droplet from being dislodged while handling. Cells suspended in the hanging media aggregate and self-assemble into a 3D spheroid over the course of hours or days depending on the cell type. Co-cultured spheroids can also be created by adding multiple cell types either at the same time or sequentially. However, owing to the small droplet

size (about 1 mm in diameter) media evaporation is often encountered. This is alleviated to a certain extent by constructing a water reservoir around the periphery of the culture plate. Also, since this technique highly relies on the surface tension of the liquid media, extra cellular matrices (usually gels) face difficulty being suspended from the aperture at the bottom of the plate.

Scaffold based techniques usually utilize hard polymeric or soft biological scaffolds for 3D cell culturing. Polymeric scaffolds have shown promise for applications where structural and physical support is required as they have the potential to recreate the natural physical and structural environment of living tissue [6, 7]. Biological scaffolds are advantageous as they do not only provide a matrix for cells to attach and reorganize but also provide the correct microenvironment of soluble growth factors, hormones and other molecules that cell interact with *in-vivo*. Cells can either be added to previously formed scaffolds or mixed with scaffold proteins in liquid state and can then be further fabricated into scaffolds, although the former approach is a cell-diffusion-limited process.

3D printing using biological materials as a building block opens up new exciting opportunities in regenerative medicine and drug screening. It also enables the creation of cell culture models for studying cellular communications and disease progression [8]. Many studies suggested that although cells may be damaged during printing, cell viability is not significantly reduced with special precautions [9–13].

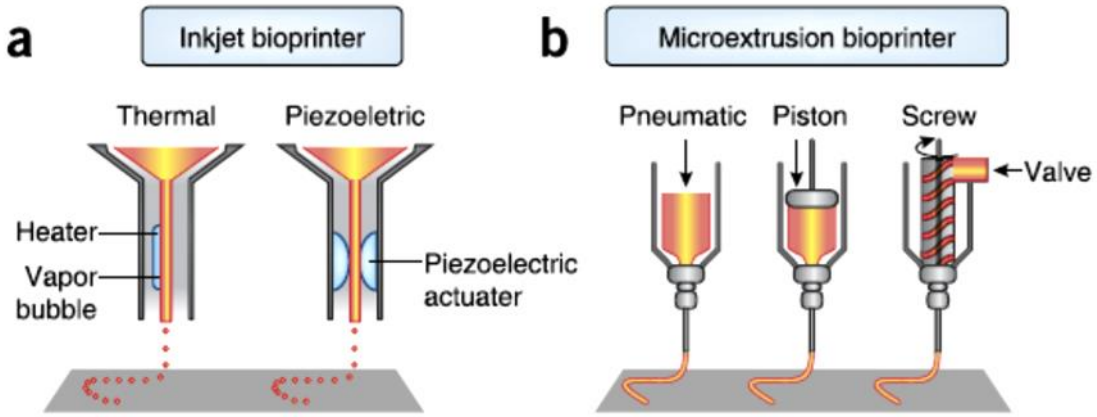

Figure 4.2: Schematic showing components and techniques used for (a) inkjet and (b) microextrusion printing [11]. Reprinted with permission from Nature publishing group.

The two major technologies that are currently used for 3D printing biological materials are inkjet printing and FDM-based microextrusion as shown in **Figure 4.2**. Each technique has certain advantages and disadvantages based on factors such as spatial resolution, cell viability and the rheology of the biological material to be printed. These factors need to be considered and optimized for successful printing.

4.4.1 Inkjet Printing:

Inkjet printing technology was first developed in the 1960s to 1970s (Buehner et al., 1977; Elmqvist, 1951; Sweet, 1965, 1975; Vaught et al., 1984) and has been widely adopted since. Today, inkjet printing has evolved from applications such as product coding and graphic art printing to more advanced applications such as digital fabrication and additive manufacturing. This is due to the ability to deposit a small amount of material in precisely defined position. In the field of biofabrication, inkjet printers are used to build 2D and 3D scaffolds and gels with biological molecules, including living cells. Inkjet printing is a non-contact method, scalable and less

susceptible to contamination making it an attractive method for bioprinting. Furthermore, inkjet printing is compatible with different fluids and not limited to polymer solutions, particle suspensions, and biomolecules provided that the "ink" satisfies certain fluid requirements reviewed by Martin *et al.* [19]. Moreover, with advancement in technologies, it becomes increasingly easier to study the inkjet process simply by using the built-in sound card in any personal computer [20].

Printing Process Overview

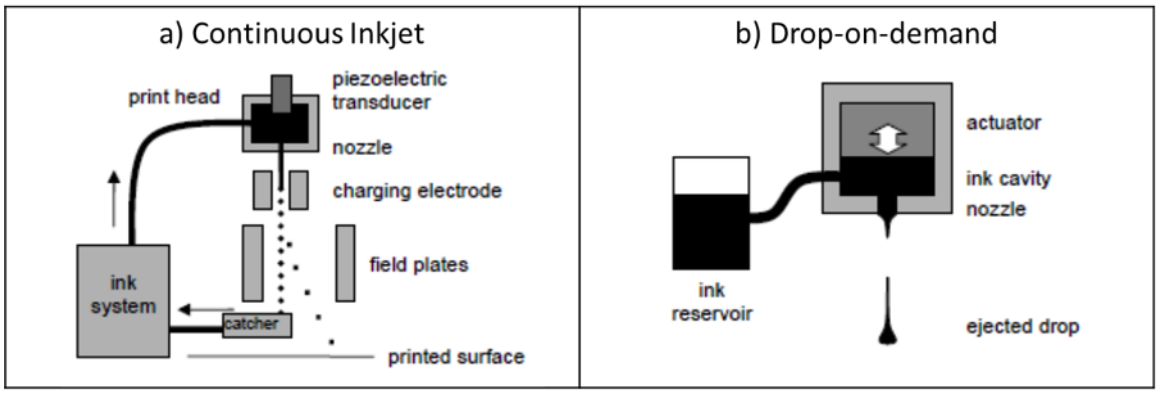

Figure 4.3: Schematic explaining basic setups for (a) continuous inkjet printers and (b) drop-on-demand inkjet printers [19]. Reprinted with permission from IOP Science.

Inkjet printing can be grouped into two major categories: (a) continuous inkjet (CIJ) printing and (b) drop-on-demand (DOD) printing as illustrated in **Figure 4.3**. Both accomplish delivery of controlled streams of ink droplets, which are deposited onto the substrate at predefined locations. CIJ printheads usually force a jet of fluid through the nozzle continuously under pressure. This jet then breaks into a stream of droplets as a result of capillary-driven Rayleigh-Plateau instability. Droplets are charged and deflected using field plates onto the substrate during printing, while the rest are recycled. Due to the

continuous jetting action, the nozzle is less likely clogged due to solvent evaporation especially if a volatile solvent is used. Besides, the resolution of CIJ is generally lower than that of DOD [21]. Also, the deposition of small fragmented drops onto the field plates can modify the electric field and in worst cases can lead to printer failure. Recycling of the ink may also lead to contamination and require re-adjusting the ink concentration to account for solvent evaporation. Owing to these drawbacks, CIJ based inkjet printing is not the technology of choice.

DOD type inkjet printing is more widely used, where the drop is only generated as needed by thermal or piezoelectric actuation. Drop-on-demand technology is in some ways simpler than continuous as it does not require the external drop selection and recovery system; however the techniques needed to make the print head, particularly with multiple fine nozzles, are very demanding. Another drawback of DOD printing is the drying of ink at the nozzle during downtime, which may further lead to particulate deposition at the nozzle and possible clogging. CIJ generally produces a high drop velocity (>10 m s^{-1}) [22] and the typical drop velocity for DOD printing is around 5 to 8 m s^{-1} [21]. This involves high velocity impact during deposition which leads to cell damage.

Two common means to trigger the ejection of a jet a fluid are through thermal or acoustic means [19]. The thermal actuator locally heats the ink solution when a voltage pulse is applied. Localized heating forms a vapor bubble and subsequently the bubble expands rapidly and explodes, which generates a pressure pulse inside the fluid chamber [23, 24]. Consequently, the ink overcomes the surface tension at the nozzle orifice and a droplet is ejected. Thermal inkjet printers are capable of dispensing various biological materials such as proteins and mammalian cells [13, 25–28]. Several

studies have demonstrated that localized heating can range from 200 °C to 300 °C, however, owing to the short duration of the heating (~2 μs) results in an overall temperature rise of only 4–10 °C in the printhead [29]. Thermal inkjet printers can achieve high printing speeds and are easily available at low cost, however, the risk of exposing cells and materials to thermal and mechanical stress, low control on droplet directionality, non-uniform droplet size, frequent clogging of the nozzle and unreliable cell encapsulation pose considerable issues for the use of these printers in 3D bioprinting.

Unlike thermal inkjet printing where droplets are ejected through a nozzle, acoustic printing employs an acoustic field to eject droplets from an open-pool nozzle-less ejection system. The sheer stresses imposed on cells at the nozzle wall are therefore avoided [30]. Typically, an acoustic printer consists of an array of 2D microfluidic channels where the ink is held in place owing to the surface tension at the small channel exit. These arrays can be combined as multiple ejectors in an adjustable format, facilitating simultaneous printing of multiple cell and material types [31]. The droplets are ejected when the force exerted by the acoustic radiation at the focal point exceeds the surface tension at the exit of the channel [30, 32].

Additionally, acoustic inkjet printers are advantageous as they are capable of generating a uniform droplet size and controlling ejection directionality as well as avoiding exposure of ink and the constituent living cells to heat and pressure stressors [33, 34]. However, since acoustic printers typically use 15 – 25 kHz frequencies, there still remains a concern regarding its ability to induce damage to the cell membrane causing potential lysis [13].

One major drawback of inkjet printers is the limitation it sets on material viscosity (ideally <10 mPa s) for successfully jetting the droplets in a controlled manner [35]. For that reason the

biological material has to be in a liquid form and should be capable of forming a solid 3D structure to impart functionality. Several studies have been performed where structural organization after jetting have been achieved by cross-linking the deposited liquid through chemical, pH or light (ultraviolet) means which often slows down the printing process [36, 37]. Imparting cross-linking ability to naturally occurring extracellular matrices (ECM) generally involves chemical modifications that require products or conditions toxic to cells and have potential repercussions on ECMs chemical and material properties [38]. Summary of latest developments in terms of theoretical understanding and experimental techniques related to inkjet printing is reviewed in more detail by Yang *et al.* [39].

4.4.2. FDM-based microextrusion printing:

This is the most common and affordable technique for 3D bioprinting. Printing method is very similar to FDM type 3D printers discussed in greater details in chapter 1. Unlike a regular FDM printer; where the printhead works on a pinch roller mechanism for feeding the feedstock, microextrusion type 3D printers are usually modified and consist of a temperature controlled material dispensing system; typically an autoclavable syringe which holds the biomaterial under controlled conditions. Material is pushed through a narrow orifice via pneumatic means or by rotating the syringe piston or screw as illustrated in **Figure 4.2**. Given their ease of disposal, sterilized metallic needles with narrow gauge size is generally used as the printing nozzle.

Microextrusion yields continuous beads or strands of material rather than liquid droplets like in inkjet printing. Each layer is deposited in two-dimensions and the printed layer serves as a foundation for laying down another layer on top of it. For this purpose it requires to allow sufficient time for the bottom layer to achieve structural integrity before extruding another layer over it.

Similar to inkjet printing, structural integrity could be achieved through means of chemical, pH or light where cross-linking is required [40].

With microextrusion methods a broad array of biocompatible materials can be used for printing and is not limited to liquid materials. Materials with viscosities in the range of 30 mPa.s to 6 X 10^7 mPa.s can be successfully extruded [11]. Materials with shear-thinning properties; a non-Newtonian material property which results in a decrease in viscosity at higher shear rates, are usually preferred. This enables extrusion through a small nozzle (100 µm – 200 µm in diameter), where the material experiences high shear rates, leading to a decrease in viscosity. Upon deposition onto the build plate, the shear rate decreases thereby leading to an increase in viscosity and help maintain the shape of printed structures.

The major advantage of microextrusion type 3D printing is its ability to deposit physiologically relevant cell densities. Marga *et al.* created 3D tissue constructs by extruding solutions of highly concentrated cells [41]. Cell survival rate with microextrusion 3D printing technique is related to the shear stresses experienced by the cells in the viscous fluid during flow through the nozzle. Survival rate is in the range of 40 – 86% and generally decreases with increasing extrusion pressure or decreasing nozzle diameter, which increases the shear rate [41, 42]. There is a trade-off between maintaining high cell viability and resolution. For instance, a large diameter nozzle will reduce the shear rate and extrusion pressure, but the printed line width will increase, reducing the lateral spatial resolution. Increasing print resolution for bioprinting is a challenge for researchers and requires use of mechanically robust biological materials that can help maintain cell viability and function after printing.

4.5 Experimental Methods:

4.5.1 Materials:

The extracellular matrix; Matrigel® used in this study was purchased from Corning Life Sciences (Cat# 354248). A mixture of dulbeccos minimal essential media (DMEM) and 10% fetal bovine serum (FBS) was used as the media for storing the printed structures. Green fluorescent protein (NIH3T3-GFP) tagged 3T3 mouse fibroblast which forms the bottom layer of the 3D printed structure was purchased from Cell Biolabs, Inc. Red fluorescent protein (4T1-RFP) tagged mouse breast cells used as the second layer of the 3D printed structure was purchased from AntiCancer Inc.

4.5.2 Rheological characterization:

TA Instruments AR-G2 rheometer was used for performing rheological characterizations. A 20-mm diameter parallel plate test fixture was used. Matrigel® was thawed overnight on an ice bath and approximately 250 µl of the solution was dispensed on the rheometer plate that was pre-chilled to 2 °C. Each sample was dispensed on the precooled rheometer plate while in liquid state. The test geometry was lowered to the desired gap height (500 or 1000 µm), and excess hydrogel was discarded. Rapidly heating (>30 °C/min) the rheometer plate initiated gelation. The testing sequence was then applied to the sample. Each sample was used for only one test. The testing time to determine gelation time and modulus was on the order of 15 mins but as a precaution, a solvent trap (with water) was used to counter any evaporation.

The accuracy of small angle oscillatory shear measurements depends on the magnitude of the torque generated by the deformation and by the instrument's ability to resolve the phase angle

between the strain wave and the stress wave. Larger torques can be produced by using larger diameter parallel plates. The AR-G2 is rated to measure a lower limit of 0.003 mN/m of torque. For that reason, the reported values of G' in this article correspond to a minimum torque of at least 0.003 mN/m.

4.5.3 FDM-based Microextrusion:

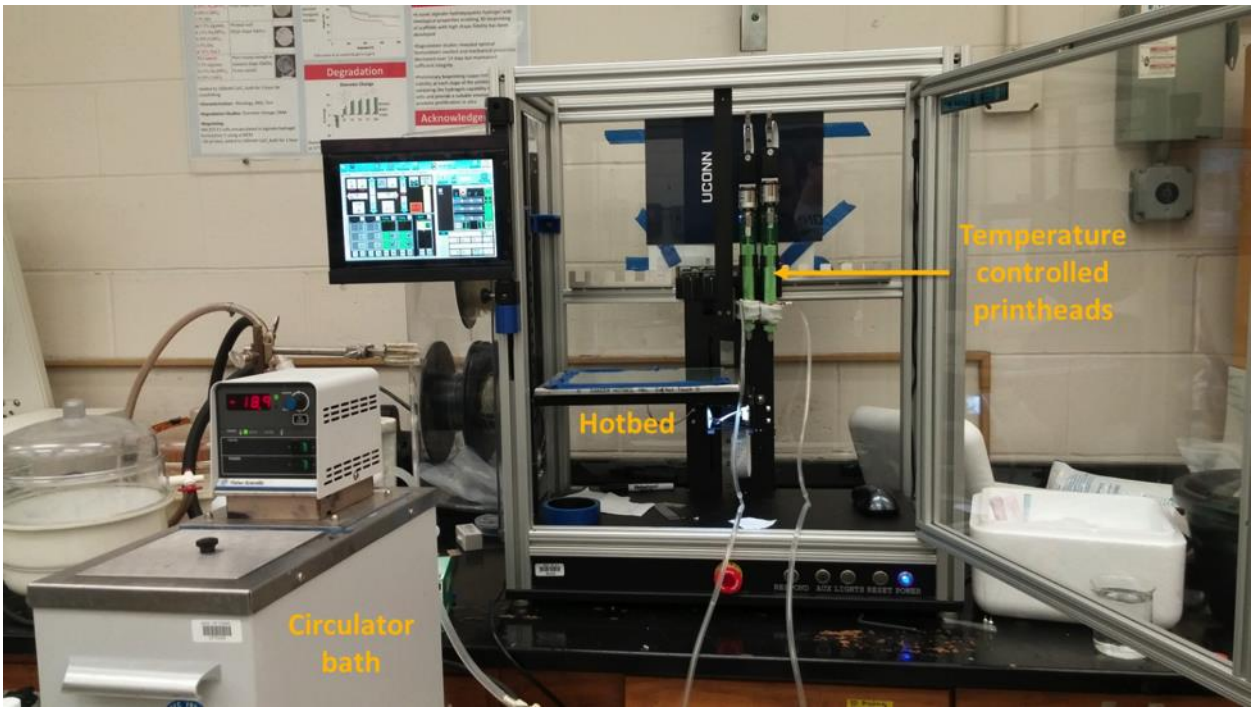

Figure 4.4: FDM based microextrusion print setup.

As discussed earlier, microextrusion technique is based on FDM. This means that the FDM type 3D printer can be utilized for printing Matrigel®, but requires a few modifications on the printer. Hyrel system 30 was used in this study and more details on capabilities and specifications of the printer can be found in chapter 3. First, the hot end extruder was swapped for a syringe-based microextrusion printhead sold by Hyrel LLC. This printhead has a piston mechanism as shown in

Figure 4.2, which pushes the material out of a 30 G blunt end metal needle (~150 µm in diameter, Hamilton Cat# 91030). Syringe and nozzle are made of anodized aluminum and stainless steel respectively, making them autoclavable. Secondly, Matrigel® requires precise control in temperature as it has a narrow window of operation (0 – 4 °C) under which it can be printed (details in results and discussions). This required building a cooling jacket around the syringe which was connected to a circulating bath via Tygon® tubing. Temperature control was made possible by circulating a cooling liquid through the jacket. Tygon® tubings used were non-insulated and this resulted in heat gain from the surrounding. For this reason, temperature of the circulating liquid was usually kept at -10 °C in order to have a temperature of 0 - 4 °C inside the syringe. This was verified by measuring the temperature of the material in the syringe before running any experiments. If needed, temperature of the circulating liquid was adjusted to bring the syringe at the desired temperature for printing Matrigel®. The modified print setup is shown in **Figure 4.4**.

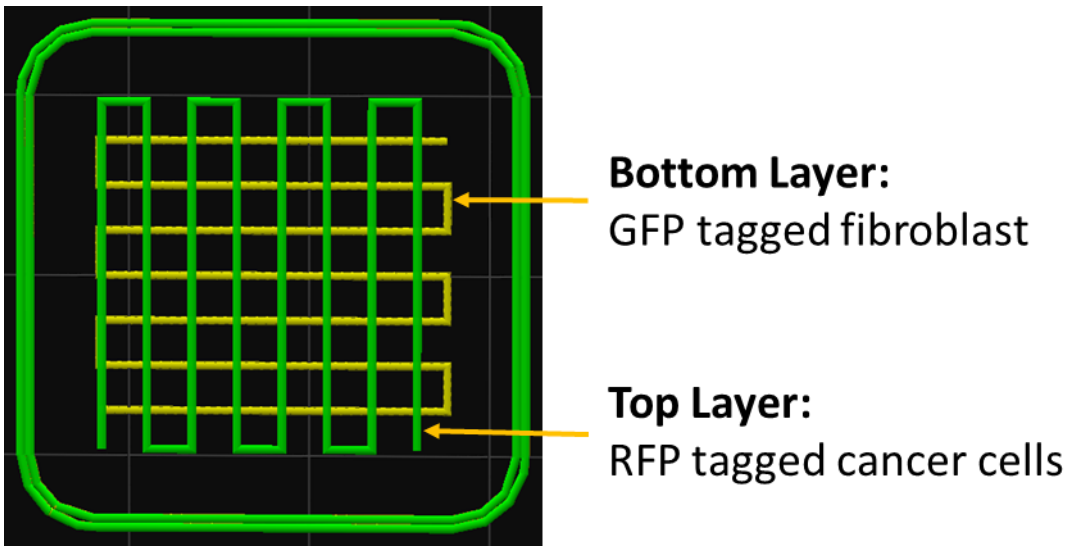

Figure 4.5: CAD rendering explaining the array construct created using microextrusion based 3D printing.

An array of interfaces between NIH3T3-GFP and 4T1-RFP cell types were fabricated using the modified 3D printer and the CAD design as shown in **Figure 4.5**. It is a two-layer structure with NIH3T3-GFP tagged fibroblast printed as the bottom layer and 4T1-RFP tagged cancer cells as the second layer, both cell types embedded in Matrigel® prior to printing. A major advantage of using microextrusion-based 3D printing technique is higher spatial accuracy and reproducibility in fabricating the construct. It also gives us the ability to choose from factors like size of the construct/array, defining the number and dimension of intersects by controlling and adjusting the flow rate, layer thickness, and linear translation speed of the printhead amongst other non-geometric process parameters.

For printing cell-laden Matrigel®, cell pellet was first dispersed in the ECM by dispensing and collecting it repeatedly through a pre-chilled pipette tip until no visual cell aggregates are observed. Similar to FDM printing, a CAD file is first sliced to stereolithography (.stl) file format where print parameters are selected and finally a gcode is used for printing the 3D structure. Build plate temperature is kept at 37 °C, a physiologically relevant temperature, which is specified as one of the print parameters.

4.5.4 Cell Line Culture

NIH3T3-GFP cells were cultured in DMEM (high glucose) supplemented with 10% FBS, 1% MEM Non-Essential Amino Acids (NEAA), 2 mM L-gluatmine and 1% Pen-Strep. 4T1-RFP cells were maintained in RPMI 1640 medium supplemented with 10% FBS, 2mM L-glutamine and 1% Pen-Strep. All cells were maintained at 37 °C in a humidified atmosphere containing 5% CO_2. For subculturing of both lines, media was removed and cells were briefly rinsed with PBS followed by 2mL of 0.25% trypsin-EDTA until cells have lifted. Upon cell lifting, 5mL of appropriate

growth medium was added to neutralize trypsanization reaction. Cell suspensions were then centrifuged for 3 min at 1000 rpm. Media was aspirated off and cell pellets were re-suspended in fresh growth media and appropriate aliquots of cell suspension was added to new plates. Subculturing ratios were 1:8 for NIH3T3-GFP and 1:6 for 4T1-RFP. Media was changed every 2 days. For 3D printing experiments, cells were counted and pellets were re-suspended in 1ml pure high concentration Matrigel® to give a final cell concentration of $1x10^6$ cells/ml. Cell solutions were placed on ice until printing experiments were performed.

4.6 Results & Discussions:

4.6.1 Rheological Characterization:

Hydrogels are extensively used and studied for many tissue-engineering applications. Their mechanical properties influence both cellular and tissue compatibility [44]. Rheology is an important tool that can help characterize the mechanical properties of a wide range of materials including hydrogels. In this study, rheology was used as a tool to discern the print parameters of temperature and print speed required for construction of the 3D array structure.

Each test was conducted at 37 °C as the maximum temperature, since in tissue engineering applications the gel will be forming in-vivo at or close to this temperature. Furthermore, each sample is loaded onto the rheometer plate as a liquid and the test geometry is set to the desired gap while still in liquid state. This ensures that the gelation of the ECM occurs within the parallel plate fixture. It is not recommended to let the ECM gel prior to dispensing on the rheometer plate and subsequently compressing the sample by lowering the test geometry to the desired gap. If allowed to gel prior to dispensing, the resulting data is then indicative of a deformed network structure and not the naturally formed network as the applied normal force during sample loading may affect the structure.

Strain sweep:

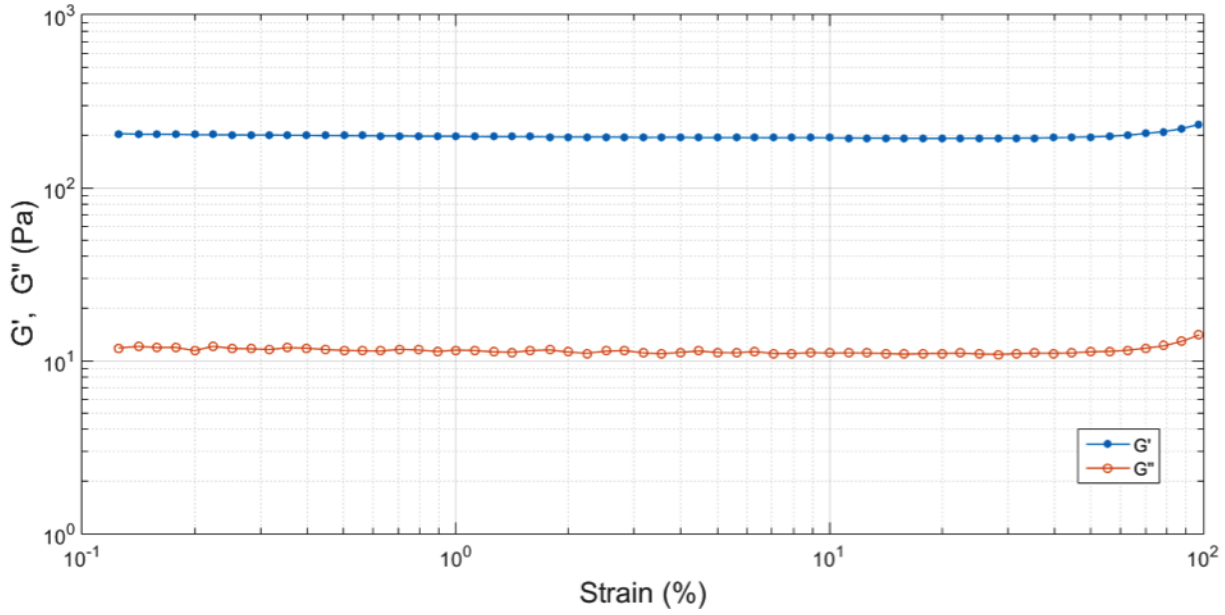

Figure 4.6: Strain sweep data at equilibrium (after 30 min) at a fixed frequency of 1 Hz and a constant temperature of 37 °C.

First, the linear viscoelastic region (LVE) of the fully formed gel was determined by performing a strain sweep. A new liquid sample was dispensed on the Peltier plate held at 2 °C and the sample was squeezed between a 20 mm parallel plate upper fixture and the Peltier, maintaining an arbitrarily chosen gap of 1 mm. The temperature was then raised to 37 °C and the sample was allowed to reach equilibrium for 30 min in the absence of rheological monitoring. A strain sweep from 0.1 – 100% strain was then carried out at an arbitrarily chosen fixed frequency of 1 Hz (6.28 rad/s) on the fully formed gel. The results are shown in **Figure 4.6**. Matrigel® showed a linear behavior up to 50% strain and a strain of 10% was chosen for subsequent rheological experiments.

Temperature sweep:

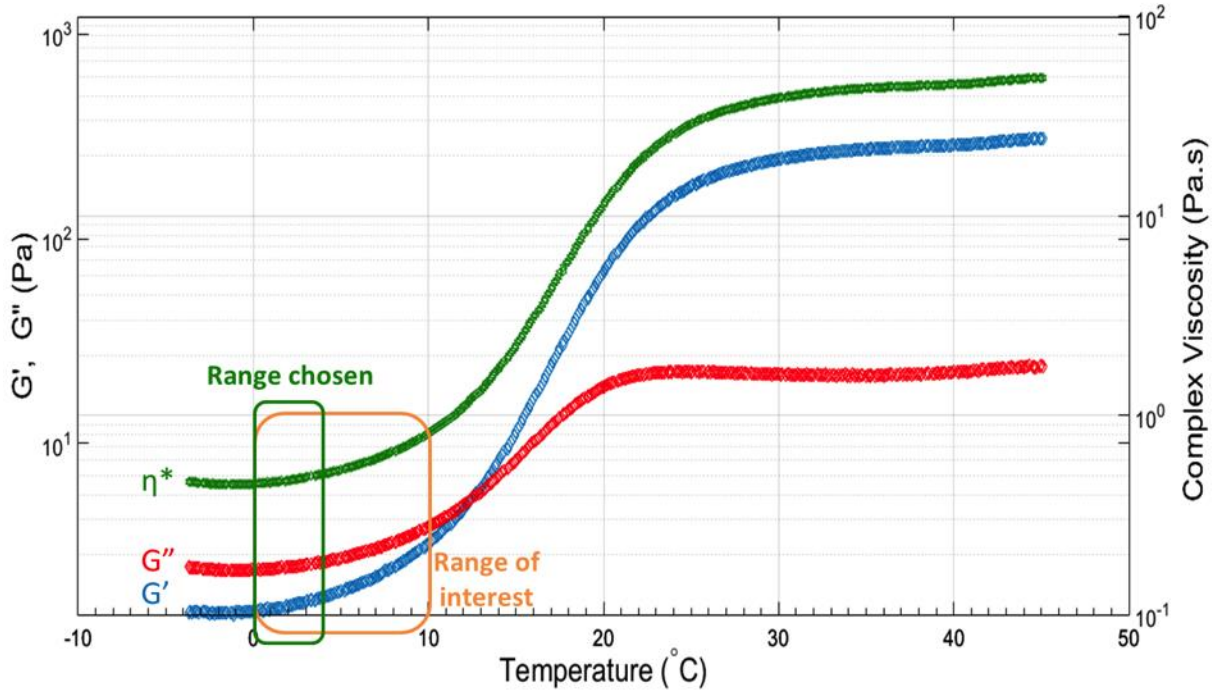

Figure 4.7: Temperature sweep data for Matrigel® at 10% strain, a fixed frequency of 1 Hz and a heating ramp rate of 1 °C/min.

After determining the LVE regime, a temperature sweep was carried out at a fixed frequency (1 Hz) and a constant strain amplitude (10%) to determine the temperature range in which Matrigel® can be printed via microextrusion. Again, a new liquid sample was dispensed on the Peltier plate held at 2 °C and the sample was squeezed between a 20 mm parallel plate geometry and the Peltier, maintaining a gap of 1 mm which was arbitrarily chosen. The run sequence was set and the temperature range from -4 – 45 °C was chosen and a heating ramp rate of 1 °C/min was arbitrarily selected. The results are shown in **Figure 4.7**. It can be observed that the cross-over of G' (solid behavior) and G" (liquid behavior), an indirect indication of gelation, happens at around 13 °C. The cross-over point being a function of frequency cannot be used as the gel point and

requires temperature sweep measurements at different frequencies to extract the loss tangent tanδ(ω) as a function of time where the intercept of tanδ(ω_i) will mark the critical gel point [45, 46]. However, for 3D printing, the ECM should preferably be in a liquid form while being extruded and gel once it is deposited onto the build plate. Therefore, a temperature of less than 13 °C can be chosen as the syringe temperature and eliminates the need for temperature sweeps at multiple frequencies to determine the critical gel point. Incorporation of a chilling jacket flushed with a circulating liquid made it possible for maintaining the syringe temperature below 4 °C. With such capabilities, a lower temperature range of 0 – 4 °C was chosen for microextrusion mainly because an increase in viscosity is associated with increasing temperature as seen from **Figure 4.7**. In general, a lower viscosity material is easier to flow through narrow orifice.

Time sweep:

Equilibrium profile:

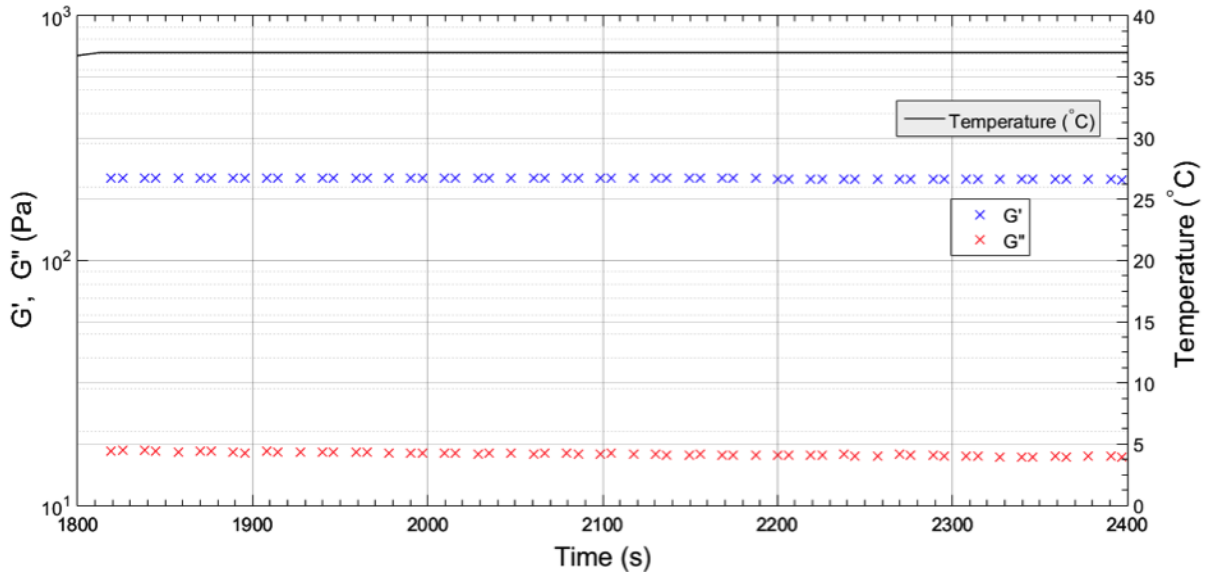

Figure 4.8: Time sweep data at equilibrium.

Time sweep experiments were carried out at % strain within the LVE limits, verified previously, to determine the equilibrium modulus and the time required to attain that. Matrigel® was first dispensed on the Peltier plate at 2 °C, gap was fixed at 1 mm and excess material discarded. Temperature was then allowed to rise to 37 °C and the sample allowed to gel without any rheological monitoring for 30 min. Matrigel® equilibrium time sweep was then performed at 10% strain amplitude and a fixed frequency of 1 Hz at 37 °C. The profile, as shown in **Figure 4.8**, thus obtained is termed as the equilibrium profile for further reference.

Microextrusion profile:

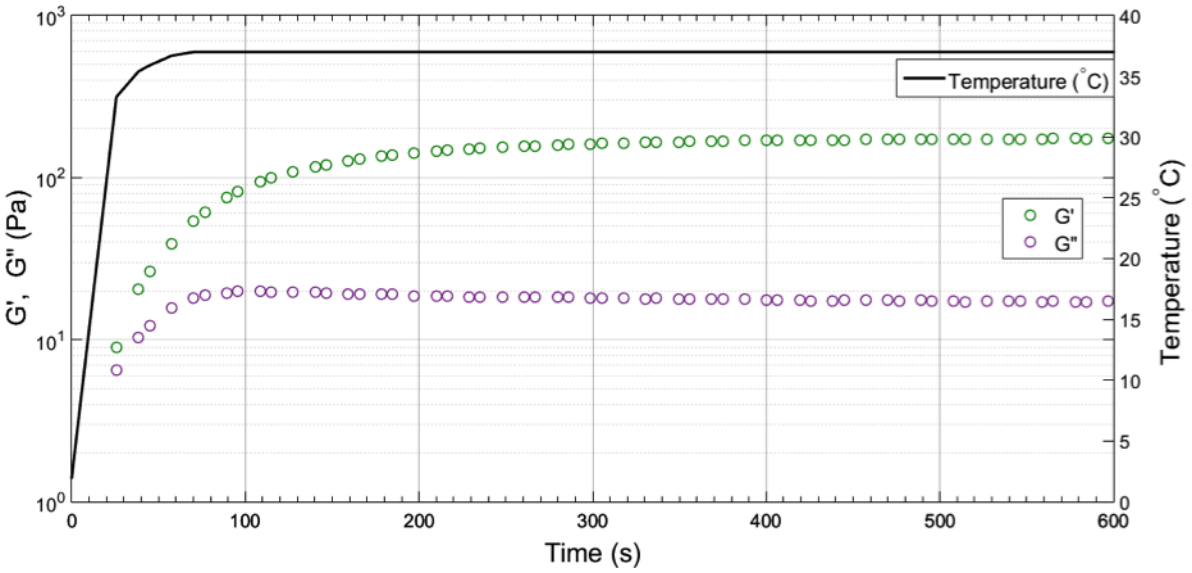

Figure 4.9: Time sweep data simulating microextrusion. A pre-shear of 50 s^{-1} was applied, followed by linear viscoelastic measurements at 10% strain and 1 Hz.

Another similar time sweep experiment was carried out within the LVE limits, this time simulating the microextrusion process. Matrigel® in the syringe is held between 0 – 4 °C and extruded through a 150 µm diameter metal needle where the material experiences shear forces while flowing

through the needle. Pre-shear at the rate of 50 s^{-1} was applied to simulate the shear experienced by the material while being extruded through the needle during 3D printing. It is extremely essential that the gel network is elastic and able to re-form and heal upon shearing in order to impart structural integrity to the printed array. The shear thinning and viscoelastic properties of Matrigel® prevents complete destruction of the network, providing a suitable environment capable of protecting cells through the extrusion process.

From **Figure 4.9**, it can be seen that in about 300 s the material recovers by approximately 90% in G' value. This helps in determining the minimum time that should be allowed for the material to gel before laying down another layer on top of it while 3D printing the array.

4.6.2 FDM based microextrusion:

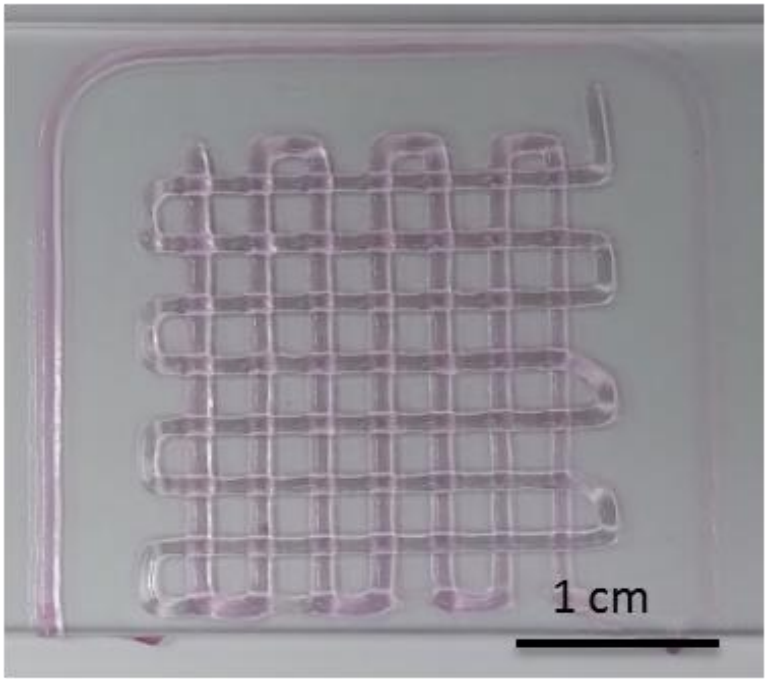

Figure 4.10: 3D printed array using NIH3T3-GFP tagged (bottom layer) and 4T1-RFP tagged (top layer) cells.

An array with two cell types have been 3D printed into a bilayer construct, each layer consisting of one individual cell type. CAD rendering is shown in **Figure 4.5**. NIH3T3-GFP tagged fibroblast and 4T1-RFP tagged cancer cells were suspended in Matrigel® and extruded through two different syringes with temperature control and laid down on the heated build plate. First, NIH3T3-GFP tagged cells were extruded forming a periphery around the array. This is to allow time for the material to yield and start flowing through the nozzle before it reaches the starting point of the structure being printed. Once the first layer was printed, the build stage was lowered and the second printhead was brought to action, again laying down a periphery around the array before printing the actual structure. **Figure 4.10** shows the 3D printed array on a glass slide.

4.6.3 Confocal Fluorescence Microscopy:

In this study, confocal fluorescence microscopy (Leica TCS SP2 microscope) was used to acquire images of the intersection between two printed layers from the 3D printed structures. A total of four intersections were imaged from two different 3D printed structures. Images were recorded at different focal planes by incrementally stepping through the samples forming a z-stack. A step-size of 5 µm was arbitrarily chosen. Z-stacks collected shows two distinct layers, the bottom layer being rich in NIH3T3-GFP tagged cells and the top layer being rich in 4T1-RFP tagged cells.

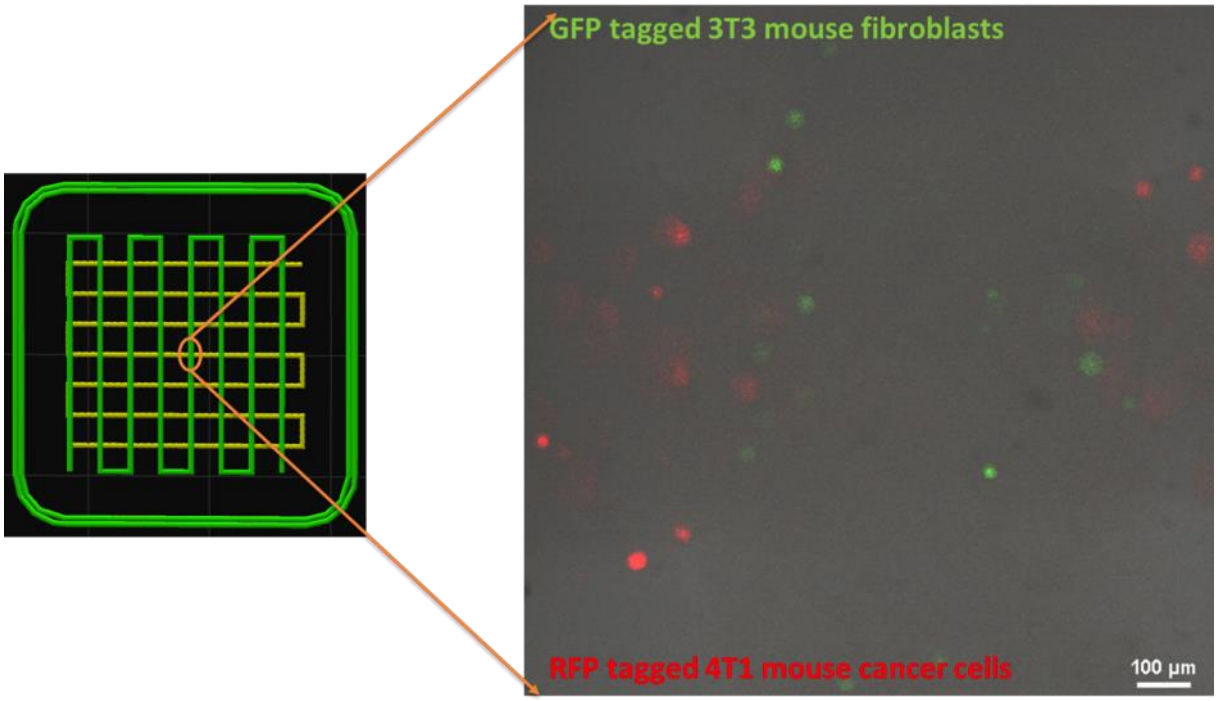

Figure 4.11: A single frame, from z-stack imaging using confocal fluorescence microscopy, showing NIH3T3-GFP and 4T1-RFP cells embedded in the ECM.

Confocal images (**Figure 4.11**) thus obtained were analyzed using ImageJ to count the total number of individual NIH3T3-GFP and 4T1-RFP tagged cells within a given intersect. The results are tabulated and shown in **table 4.1**. On an average 24 ± 3 individual NIH3T3-GFP cells and 25 ± 6 individual 4T1-RFP cells were located within a given intersect. The results indicate that FDM based microextrusion 3D printing technique can be successfully utilized for laying down viable cells for subsequent 3D cell culturing and similar studies. However, since the cell count for a given intersect is typically less than 30, precision and reproducibility of the process cannot be inferred with confidence.

Table 4.1: Cell count of individual NIH3T3-GFP and 4T1-RFP tagged cells within a given intersect.

Sample	**Cell Count**	
	4T1-RFP	**NIH3T3-GFP**
1	33	19
2	19	26
3	19	28
4	30	23
Average	25	24
Standard Deviation	6	3

4.7 CONCLUSIONS & FUTURE WORK

The aim of this study is to 3D print cell-laden Matrigel® structures as 3D cell cultures for studying cancer progression. Rheology was successfully used as a tool to identify the optimal print temperature for the Matrigel®. A rheology protocol is defined to gather important non-geometric process parameters for 3D printing. Strain sweep experiment helps gather information of the LVE region of the fully formed gel. A temperature sweep within the limits of LVE helps identify the temperature requirements for printing. A time sweep experiment simulating the microextrusion process can be used to get information on the gelation time of the matrix material. These characterized process parameters can be incorporated while designing and slicing the 3D construct for a successful print.

Rheological parameters identified for Matrigel® were utilized for successfully 3D printing an array of intersects using NIH3T3-GFP mouse fibroblast and 4T1-RFP mouse cancer cells. Z-stacks collected immediately after 3D printing using confocal fluorescence microscopy shows two distinct layers, one with NIH3T3-GFP and the other with 4T1-RFP tagged cells. Even though the individual cell count in each layer for different intersects is consistent, reproducibility cannot be deduced from these experiments. More experiment needs to be carried out with a higher initial cell concentration to infer reproducibility in creating arrays using microextrusion based 3D printing.

4.8 REFERENCES

[1] C. Desantis, R. Siegel, and A. Jemal, “Breast Cancer Facts & Figures 2015-2016,” *Surveill Heal Serv Res Progr*, 2015.

[2] C. J. Lovitt, T. B. Shelper, and V. M. Avery, “Advanced Cell Culture Techniques for Cancer Drug Discovery,” *Biology (Basel)*, vol. 3, no. 2, pp. 345–367, Jun. 2014.

[3] L. a Gurski, N. J. Petrelli, X. Jia, and M. C. Farach-carson, “3D Matrices for Anti-Cancer Drug Testing and Development,” *Oncol Issues*, vol. 25, no. February, pp. 20–25, 2010.

[4] C. S. Hughes, L. M. Postovit, and G. A. Lajoie, “Matrigel: a complex protein mixture required for optimal growth of cell culture.,” *Proteomics*, vol. 10, no. 9, pp. 1886–1890, 2010.

[5] G. Benton, J. George, H. K. Kleinman, and I. P. Arnaoutova, “Advancing science and technology via 3D culture on basement membrane matrix,” *J Cell Physiol*, vol. 221, no. 1, pp. 18–25, 2009.

[6] A. Sourla, C. Doillon, and M. Koutsilieris, “Three-dimensional type I collagen gel system containing MG-63 osteoblasts-like cells as a model for studying local bone reaction caused by metastatic cancer cells.,” *Anticancer Res*, vol. 16, no. 5A, pp. 2773–80.

[7] W. Tan, R. Krishnaraj, and T. A. Desai, “Evaluation of Nanostructured Composite Collagen–Chitosan Matrices for Tissue Engineering,” *Tissue Eng*, vol. 7, no. 2, pp. 203–210, Apr. 2001.

[8] S. Khetan and J. A. Burdick, “Patterning hydrogels in three dimensions towards controlling cellular interactions,” *Soft Matter*, vol. 7, no. 3, p. 830, 2011.

[9] P. Calvert, “Materials science. Printing cells.,” *Science*, vol. 318, no. 2007, pp. 208–209,

2007.

[10] B. Lorber, W.-K. Hsiao, I. M. Hutchings, and K. R. Martin, “Adult rat retinal ganglion cells and glia can be printed by piezoelectric inkjet printing.,” *Biofabrication*, vol. 6, no. 1, p. 15001, Mar. 2014.

[11] S. V Murphy and A. Atala, “3D bioprinting of tissues and organs.,” *Nat Biotechnol*, vol. 32, no. 8, pp. 773–785, 2014.

[12] R. E. Saunders, J. E. Gough, and B. Derby, “Delivery of human fibroblast cells by piezoelectric drop-on-demand inkjet printing,” *Biomaterials*, vol. 29, pp. 193–203, 2008.

[13] T. Xu, J. Jin, C. Gregory, J. J. Hickman, and T. Boland, “Inkjet printing of viable mammalian cells,” *Biomaterials*, vol. 26, pp. 93–99, 2005.

[14] R. Elmqvist, “United States Patent,” 2566443, 1951.

[15] R. G. Sweet, “High frequency recording with electrostatically deflected ink jets,” *Rev Sci Instrum*, vol. 36, no. 2, pp. 131–136, 1965.

[16] R. G. Sweet, “United States Patent 3596275,” US3596275 A, 1975.

[17] W. L. Buehner, J. D. Hill, T. H. Williams, and J. W. Woods, “Application of Ink Jet Technology to a Word Processing Output Printer,” *IBM J Res Dev*, vol. 21, no. 1, pp. 2–9, Jan. 1977.

[18] J. L. Vaught, F. L. Cloutier, D. K. Donald, J. D. Meyer, C. A. Tacklind, and H. H. Taub, “United States Patent 4490728,” 1984.

[19] G. D. Martin, S. D. Hoath, and I. M. Hutchings, “Inkjet printing - the physics of manipulating liquid jets and drops,” *J Phys Conf Ser*, vol. 105, p. 12001, 2008.

[20] B. Bognet, Y. Guo, and A. W. K. Ma, “Controlling system components with a sound card: A versatile inkjet fluid testing platform,” *Rev Sci Instrum*, vol. 87, no. 1, 2016.

[21] I. M. Hutchings and G. D. Martin, *Inkjet Technology for Digital Fabrication*. Chicester: Wiley, 2012.

[22] B. Derby, “Inkjet Printing of Functional and Structural Materials: Fluid Property Requirements, Feature Stability, and Resolution,” *Annu Rev Mater Res*, vol. 40, no. 1, pp. 395–414, Jun. 2010.

[23] X. Cui and T. Boland, “Human microvasculature fabrication using thermal inkjet printing technology,” *Biomaterials*, vol. 30, no. 31, pp. 6221–6227, 2009.

[24] M. M. Mohebi and J. R. G. Evans, “A drop-on-demand ink-jet printer for combinatorial libraries and functionally graded ceramics,” *J Comb Chem*, vol. 4, no. 4, pp. 267–274, 2002.

[25] E. A. Roth, T. Xu, M. Das, C. Gregory, J. J. Hickman, and T. Boland, “Inkjet printing for high-throughput cell patterning,” *Biomaterials*, vol. 25, no. 17, pp. 3707–3715, 2004.

[26] T. Xu, W. Zhao, J. M. Zhu, M. Z. Albanna, J. J. Yoo, and A. Atala, “Complex heterogeneous tissue constructs containing multiple cell types prepared by inkjet printing technology,” *Biomaterials*, vol. 34, no. 1, pp. 130–139, 2013.

[27] X. Cui, K. Breitenkamp, M. G. Finn, M. Lotz, and D. D. D ’lima, “Direct Human Cartilage Repair Using Three-Dimensional Bioprinting Technology,” *Tissue Eng Part A*, vol. 18, pp. 1304–1312, 2012.

[28] X. Cui, K. Breitenkamp, M. Lotz, and D. D’Lima, “Synergistic action of fibroblast growth factor-2 and transforming growth factor-beta1 enhances bioprinted human neocartilage

formation," *Biotechnol Bioeng*, vol. 109, no. 9, pp. 2357–2368, 2012.

[29] X. Cui, D. Dean, Z. M. Ruggeri, and T. Boland, "Cell damage evaluation of thermal inkjet printed chinese hamster ovary cells," *Biotechnol Bioeng*, vol. 106, no. 6, pp. 963–969, 2010.

[30] U. Demirci and G. Montesano, "Single cell epitaxy by acoustic picolitre droplets.," *Lab Chip*, vol. 7, no. 9, pp. 1139–45, 2007.

[31] S. Tasoglu and U. Demirci, "Bioprinting for stem cell research," *Trends Biotechnol*, vol. 31, no. 1, pp. 10–19, 2013.

[32] U. Demirci, "Acoustic picoliter droplets for emerging applications in semiconductor industry and biotechnology," *J Microelectromechanical Syst*, vol. 15, no. 4, pp. 957–966, 2006.

[33] R. Saunders, L. Bosworth, J. Gough, B. Derby, and N. Reis, "Selective cell delivery for 3D tissue culture and engineering," *Eur Cells Mater*, vol. 7, no. SUPPL.1, p. 84, 2004.

[34] M. Nakamura, A. Kobayashi, F. Takagi, A. Watanabe, Y. Hiruma, K. Ohuchi, Y. Iwasaki, M. Horie, I. Morita, and S. Takatani, "Biocompatible Inkjet Printing Technique for Designed Seeding of Individual Living Cells," *Tissue Eng*, vol. 11, no. 11–12, pp. 1658–1666, 2005.

[35] J. D. Kim, J. S. Choi, B. S. Kim, Y. Chan Choi, and Y. W. Cho, "Piezoelectric inkjet printing of polymers: Stem cell patterning on polymer substrates," *Polymer (Guildf)*, vol. 51, no. 10, pp. 2147–2154, 2010.

[36] S. V Murphy, A. Skardal, and A. Atala, "Evaluation of hydrogels for bio-printing applications.," *J Biomed Mater Res A*, vol. 101, no. 1, pp. 272–84, Jan. 2013.

[37] S. Khalil and W. Sun, “Biopolymer deposition for freeform fabrication of hydrogel tissue constructs,” *Mater Sci Eng C*, vol. 27, no. 3, pp. 469–478, 2007.

[38] W. E. Hennink and C. F. van Nostrum, “Novel crosslinking methods to design hydrogels,” *Adv Drug Deliv Rev*, vol. 64, no. SUPPL., pp. 223–236, 2012.

[39] Y. Guo, H. S. Patanwala, B. Bognet, and A. W. K. Ma, “Inkjet and inkjet-based 3D printing: connecting fluid properties and printing performance,” *Rapid Prototyp J*, vol. 23, no. 3, pp. 562–576, Apr. 2017.

[40] S. T. Bendtsen and M. Wei, “Synthesis and characterization of a novel injectable alginate–collagen–hydroxyapatite hydrogel for bone tissue regeneration,” *J Mater Chem B*, vol. 3, no. 15, pp. 3081–3090, 2015.

[41] F. Marga, K. Jakab, C. Khatiwala, B. Shephard, S. Dorfman, and G. Forgacs, “Organ Printing: A Novel Tissue Engineering Paradigm,” in *5th European Conference of the International Federation for Medical and Biological Engineering: 14--18 September 2011, Budapest, Hungary*, Á. Jobbágy, Ed. Berlin, Heidelberg: Springer Berlin Heidelberg, 2012, pp. 27–30.

[42] R. Chang, J. Nam, and W. Sun, “Effects of Dispensing Pressure and Nozzle Diameter on Cell Survival from Solid Freeform Fabrication–Based Direct Cell Writing,” *Tissue Eng Part A*, vol. 14, no. 1, pp. 41–48, 2008.

[43] C. M. Smith, A. L. Stone, R. L. Parkhill, R. L. Stewart, M. W. Simpkins, A. M. Kachurin, W. L. Warren, and S. K. Williams, “Three-dimensional bioassembly tool for generating viable tissue-engineered constructs.,” *Tissue Eng*, vol. 10, no. 9, pp. 1566–1576, 2004.

[44] J. M. Zuidema, C. J. Rivet, R. J. Gilbert, and F. A. Morrison, “A protocol for rheological

characterization of hydrogels for tissue engineering strategies," *J Biomed Mater Res - Part B Appl Biomater*, vol. 102, no. 5, pp. 1063–1073, 2014.

[45] H. H. Winter and F. Chambon, "Analysis of Linear Viscoelasticity of a Crosslinking Polymer at the Gel Point," *J Rheol (N Y N Y)*, vol. 30, no. 2, p. 367, 1986.

[46] F. Chambon and H. H. Winter, "Linear Viscoelasticity at the Gel Point of a Crosslinking PDMS with Imbalanced Stoichiometry," *J Rheol (N Y N Y)*, vol. 31, no. 8, pp. 683–697, Nov. 1987.